Magnetic resonance imaging in ^{166}Ho liver radioembolization

Gerrit van de Maat

Colophon

Magnetic resonance imaging in ^{166}Ho liver radioembolization

PhD thesis, Utrecht University, the Netherlands

ISBN: 978-90-393-5933-4

The research described in this dissertation was carried out at the Image Sciences Institute and the Department of Radiology and Nuclear Medicine, University Medical Center Utrecht, Utrecht, the Netherlands. The project was financially supported by the Dutch Technology Foundation (STW) under grant OTP06648 and by the Dutch Cancer Society (KWF Kankerbestrijding) under grant UU2009-4346

Printing of this thesis was financially supported by Philips Healthcare, Röntgenstichting Utrecht, and the Ina Veenstra-Rademaker stichting

Printed by: Gildeprint Drukkerijen, the Netherlands

Magnetic resonance imaging in ^{166}Ho liver radioembolization

Magnetische resonantie beeldvorming rondom
^{166}Ho radioembolisatie van de lever

(met een samenvatting in het Nederlands)

Proefschrift

ter verkrijging van de graad van doctor aan de Universiteit Utrecht
op gezag van de rector magnificus, prof. dr. G.J. van der Zwaan,
ingevolge het besluit van het college voor promoties
in het openbaar te verdedigen
op donderdag 4 april 2013 des middags te 2.30 uur

door

Gerrit Hendrik van de Maat

geboren op 16 april 1982 te Almelo

Promotoren:	Prof. dr. ir. M.A. Viergever
	Prof. dr. M.A.A.J. van den Bosch
Co-promotor:	Dr. C.J.G. Bakker

Contents

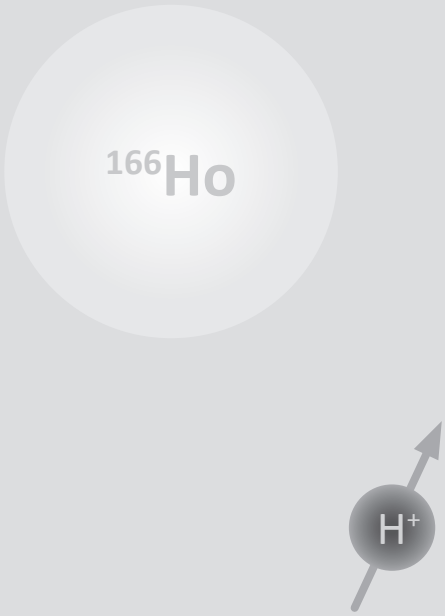
166Ho
H+

Chapter 1

Introduction

"In this thesis, the utility of MRI in radioembolization therapy with Ho-MS is explored, addressing several aspects regarding the influence of Ho-MS on MR imaging and how this influence can be exploited or should be taken into account."

Intra-arterial radioembolization (RE) is an increasingly applied, minimally invasive therapy for patients with unresectable primary or metastatic liver tumors (1-4). In RE, radioactive microspheres are administered to the liver through a catheter that is positioned in the hepatic artery. The infused microspheres are carried along with the blood stream and finally lodge in the microvasculature of the liver. Since liver tumors receive the bulk of their blood supply from the hepatic artery, whereas healthy liver tissue mainly is supplied by the portal vein (5, 6), the majority of the microspheres is expected to lodge in the peritumoral vasculature. This will lead to selective irradiation of tumorous tissue while sparing most of the healthy liver tissue (7).

Microspheres suitable for radioembolization contain a β-emitting radioisotope embedded in a carrier that possesses a high mechanical and chemical stability. Furthermore, the microspheres have uniform size and density and the used radioisotope has a half-life of a few days. Microspheres that have been developed for clinical use thus far contain yttrium-90 (^{90}Y), rhenium-186/rhenium-188 (^{186}Re/^{188}Re) or holmium-166 (^{166}Ho), embedded in poly L-lactic acid (PLLA), resin, albumin or glass. Of these microspheres, the ^{90}Y resin spheres (SIR-Spheres®, Sirtex Medical Limited, North Sydney, NSW, Australia) and ^{90}Y glass spheres (TheraSphere®, Nordion, Ottawa, Canada) are currently widely used in clinical practice (3, 8). ^{188}Re human serum albumin microspheres have been tested in a small cohort of patients (9) whereas the use of ^{166}Ho PLLA microspheres has recently been investigated in a Phase I clinical trial (10).

A crucial condition for safe and effective treatment with radioembolization is an optimal microsphere biodistribution, i.e., the majority of the microspheres ending up in or surrounding tumorous tissue. Furthermore, extrahepatic deposition of radioactive microspheres has to be averted to avoid potential damage to healthy organs leading to complications (11-15). In particular for this last purpose, extensive treatment planning is carried out including visceral angiography to visualize extrahepatic vessels branching off the hepatic artery, interventional preparation of these vessels by coil embolization (16) and administration of a test dose (17). This test dose is a small dose of technetium-99m-labeled macro aggregated albumin (^{99m}Tc-MAA), which is expected to behave similarly to the therapeutic dose and, therefore, to simulate the therapy. Imaging of the distribution of the test dose using gamma scintigraphy and single photon emission computed tomography (SPECT) provides an estimation of potential lung shunt fraction and extra-hepatic deposition of the therapeutic dose (11, 12, 18, 19).

Although extensive treatment planning will minimize the risk of complications owing to extrahepatic microsphere deposition, the occurrence of liver related complications, like radiation-induced liver disease and liver toxicity, will largely depend on the intrahepatic distribution of the delivered dose. Furthermore, treatment efficacy will depend on the total radiation dose that is delivered to the tumors. To evaluate safety and efficacy of RE,

accurate assessment of the microsphere biodistribution in the liver after treatment is therefore indispensable. In the current clinical situation, where typically ^{90}Y microspheres are used for radioembolization, measuring the microsphere distribution is a challenging task since ^{90}Y lacks good imaging properties. Bremsstrahlung SPECT imaging is possible but has an inherently low resolution and quantitative measurements are hampered by scattering (20-23). Positron emission tomography (PET), exploiting the low positron abundance of ^{90}Y, offers a better spatial resolution but has a low sensitivity (24, 25).
Especially with respect to in vivo imaging of the microsphere biodistribution for safety and efficacy assessment, ^{166}Ho PLLA microspheres (26, 27), further abbreviated in this work as Ho-MS, have been shown to be a promising alternative. Although the energy of the beta particles emitted by ^{166}Ho is lower than the energy of ^{90}Y beta particles (E_{max} = 1.85 MeV for ^{166}Ho vs E_{max} = 2.28 MeV for ^{90}Y), requiring a total activity that is threefold higher to achieve a similar radiation dose, and the decay time is shorter (26.8h for ^{166}Ho vs 64.1h for ^{90}Y) which may logistically be more challenging, Ho-MS can be visualized in vivo with a range of clinical imaging modalities. γ-Emission of activated microspheres (E_{γ} = 80.6 keV) allows quantitative SPECT imaging (28), the relatively high radiopacity of holmium provides detectable contrast in computed tomography (CT) and the paramagnetic nature of holmium can be exploited using magnetic resonance imaging (MRI) (29). SPECT has a high Ho-MS sensitivity but lacks spatial and temporal resolution. CT is capable of imaging at high spatiotemporal resolution and offers anatomical reference information, but has a low Ho-MS sensitivity. MRI combines a good Ho-MS sensitivity with good spatiotemporal resolution and soft tissue contrast. Furthermore, MRI can be used for catheter tracking (30), thus enabling fully MR-guided endovascular hepatic intervention required for the microsphere delivery (31). Finally, MRI enables functional imaging like diffusion and perfusion imaging which makes it an attractive modality for treatment response follow-up. The combination of the paramagnetic nature of the holmium microspheres and the imaging possibilities of MRI thus provides an ideal platform for fully image-guided radioembolization therapy.

In this thesis, the utility of MRI in radioembolization therapy with Ho-MS is explored, addressing several aspects regarding the influence of Ho-MS on MR imaging and how this influence can be exploited or should be taken into account. The work primarily focuses on quantitative MRI-based biodistribution measurements after radioembolization and how these measurements can be used to estimate the tissue absorbed radiation dose. Besides, part of this thesis deals with the influence the presence of the microspheres has on diagnostic imaging for tumor response assessment.
In **Chapter 2**, the feasibility of MRI-based quantitative biodistribution assessment after radioembolization is demonstrated using data obtained from the first patients treated

ever with ^{166}Ho radioembolization. It is shown that by measuring the holmium induced R_2^* signal decay, utilizing a multi-gradient echo acquisition prior to and after microsphere administration, the Ho-MS biodistribution can be visualized with great detail and the local amount of microspheres can be estimated for dosimetric purposes. **Chapter 3** describes a post-processing method, S_0-fitting, that enables the quantification of high local concentrations of Ho-MS in case the conventional quantification method as presented in chapter 2 fails because the MR signal decays too fast. S_0-fitting incorporates the estimated initial amplitude of the free induction decay (FID) curve, S_0, of well-characterized neighboring voxels into the fitting procedure of the voxel that cannot be characterized by the conventional fitting algorithm. In **Chapter 4**, the accuracy of MRI for absorbed radiation assessment after radioembolization is demonstrated. This is done by comparing MRI-based radiation-absorbed dose measurements, on an anthropomorphic phantom and on an ex vivo human liver, with SPECT-based measurements. Chapter 5 presents a new method for MRI-based Ho-MS quantification, S_0 estimation of the free induction decay combined with a single spin echo measurement (SOFIDSE). SOFIDSE estimates R_2^* and the initial amplitude of the MR signal S_0 from a multi gradient echo acquisition of the FID and subsequently estimates R_2 utilizing S_0 and a single spin echo readout. By a subtraction of R_2^* and R_2 the Ho-MS induced R_2' signal decay is determined, which is linearly related to the local concentration of microspheres. Since the estimated R_2' is only dependent on changes in signal decay induced by the microspheres, the method is insensitive to changes in R_2 following changes in tissue characteristics and in principle takes away the requirement for pretreatment image acquisition. In **Chapter 6**, the influence of temperature and proton diffusion on the accuracy of the quantification methods described in chapters 2 and 5 is investigated. By measuring the holmium microsphere relaxation rates R_2^* and R_2 for a range of temperatures and apparent diffusion coefficients (ADC), it is demonstrated that both temperature and ADC are factors that can affect microsphere quantification. **Chapter 7** is concerned with the influence of Ho-MS on image based treatment follow-up after radioembolization. The influence of Ho-MS on diffusion weighted imaging (DWI), a functional MR imaging method that holds promise for measuring tumor response at an early stage, is explored. It is shown that the presence of Ho-MS results in signal reduction on diffusion weighted images, thereby hampering accurate ADC characterization. In the final chapter, **Chapter 8**, a summary of the work described in this thesis is given, providing an overview of the current role MRI can play in ^{166}Ho radioembolization, and some future directions are outlined.

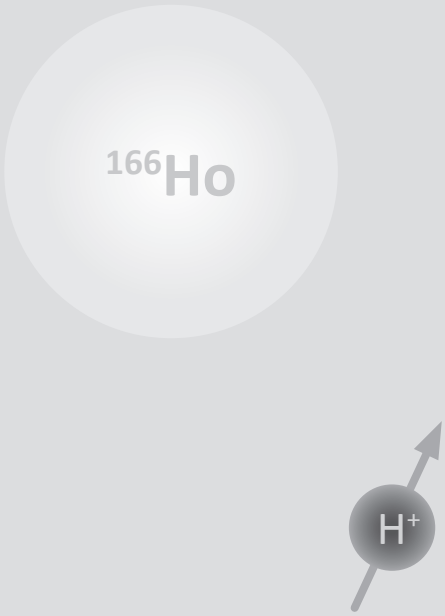
166Ho
H+

Chapter 2

Biodistribution assessment in patients

"The aim of the work described in this chapter was to investigate the capability of MRI to measure the intrahepatic microsphere distribution in order to quantify the absorbed radiation dose in patients treated with Ho-MS radioembolization."

Based on:
van de Maat GH, Seevinck PR, Elschot M, et al. MRI-based biodistribution assessment of holmium-166 (poly(L-lactic acid) microspheres after radioembolisation. Eur Radiol 2013;23:827-835

INTRODUCTION

Yttrium-90 (^{90}Y) radioembolization (RE) is increasingly used for the treatment of patients with unresectable primary or metastatic liver tumors (3, 8, 17, 32-34). The two commercially available products, SIR-Spheres® (Sirtex Medical Limited, North Sydney, NSW, Australia) and TheraSphere® (Nordion, Ottawa, Canada), use empirical methods for dose calculation, based on body surface area and total liver weight respectively. However, apart from the total dose delivered to the liver, the efficacy of RE will largely depend on the intrahepatic dose distribution or, more specifically, on the ratio between the tumor absorbed dose and healthy tissue absorbed dose. Quantitative assessment of the post-administration intrahepatic microsphere distribution is therefore indispensable for evaluation of RE toxicity and efficacy and can potentially be used for the prediction of patient response and patient-specific therapeutic dose optimization. Image-based approaches to assess the microsphere distribution after RE have gained interest but are mostly hampered by the limited imaging possibilities of the isotope ^{90}Y. Quantitative ^{90}Y-SPECT imaging has limited spatial resolution because it is based on ^{90}Y Bremsstrahlung (20-23), whereas ^{90}Y-PET has better spatial resolution but low sensitivity (24, 25). As a consequence, alternative methods of visualizing the microspheres have been investigated such as MR imaging of iron-labeled microspheres (35).

In the past decade, holmium-166 (^{166}Ho) poly(L-lactic acid)-loaded microspheres (Ho-MS) have been developed as a potential radioembolization particle (27, 36). Neutron activated holmium-166 is a β-emitting (E_β = 1.77 and 1.85 MeV; I_β = 48.7% and 50%, respectively; $T_{1/2}$ = 26.8 h) and γ-emitting (E_γ = 80.6 keV) lanthanide that, embedded in microspheres of poly(L-lactic acid), yields a particle suitable for internal radiation therapy that can be visualized with a range of clinical imaging techniques, including SPECT and MRI. This multimodal imaging has previously been demonstrated in preclinical animal studies (37-39). It was also shown that MRI combines high sensitivity with high spatial-temporal resolution and with superior soft tissue contrast (29) and thus can be used to cover a broad range of clinically interesting imaging parameters. More recently, it was shown for an ex vivo situation that MRI is able to provide a good measurement of the Ho-MS radiation-absorbed dose by convolution of quantitative MRI data with a ^{166}Ho dose point kernel (40).

The feasibility of image-guided RE using Ho-MS was tested in a first-time-in-man clinical phase I study. The aim of the work described in this chapter was to investigate the capability of MRI to measure the intrahepatic microsphere distribution in order to quantify the absorbed radiation dose in patients treated with Ho-MS radioembolization.

MATERIALS AND METHODS

Patients

To be eligible to enter the phase I study each patient needed to comply with the following inclusion criteria: written informed consent; age 18 years or older; presence of liver-dominant, unresectable, chemorefractory liver metastases of any primary tumor with at least one measurable lesion of ≥10 mm in the longest diameter on CT; an estimated life expectancy >3 months; World Health Organization (WHO) performance status 0–2; and a negative pregnancy test for women. Furthermore, patients with contraindications for MRI were excluded from treatment. Ethics approval for this study was obtained from the institutional review board; the study was performed in accordance with the Declaration of Helsinki and was registered with Clinicaltrials.gov, number NCT01031784.

Treatment

Holmium-165 poly(L-lactic acid) microspheres with a mean diameter of 30 µm (range 20–50 µm) and a holmium content of 18.7% (weight/weight) were prepared under Good Laboratory Practice (GLP) guidelines as previously described (27). The amount of microspheres (600 mg) was weighed, packed in high-density polyethylene vials (Posthumus Plastics, Beverwijk, the Netherlands) and sent to the nuclear reactor (Delft University of Technology, Delft, the Netherlands) for neutron activation (41). The calculation of the amount of radioactivity was based on liver weight, conforming to the clinically used approach for TheraSphere®. The amount of administered ^{166}Ho-radioactivity was calculated using the target liver absorbed dose in a dose-escalation fashion (20, 40, 60, or 80 Gy) as previously described (42). All patients received whole liver treatment. The activity to be administered was calculated assuming homogeneous distribution of the activity in the liver using the following formula: A_{Ho166} (MBq) = Liver Dose x 63 (MBq/J) x LW, where A_{Ho166} is the administered activity, LW is the liver weight in kg, and Liver Dose is the intended liver absorbed radiation dose in Gy. While the radioactivity was different for each patient, the amount of administered Ho-MS was kept constant at 600 mg. Before administration, the amount of radioactivity in the vials was measured using a dose calibrator (VDC-404, Veenstra Instrumenten B.V., Joure, the Netherlands) and the specific activity of the Ho-MS was determined. After administration, activity measurements were performed on the administration system to determine the amount of microspheres that was actually delivered to the subjects retrospectively.

Radioembolization procedure

Radioembolization was performed according to standard recommendations (18, 43). Relevant vessels, in particular branches of the hepatic artery supplying organs other than the liver, e.g., the gastroduodenal artery and right gastric artery, were coiled during a pretreatment angiographic procedure to prevent extrahepatic deposition of activity. A scout dose of ^{99m}Tc-MAA (150 MBq, 0.8 mg, TechneScan LyoMaa®, Mallinckrodt Medical B.V., Petten, the Netherlands) was injected into the hepatic artery followed by planar gamma camera imaging and SPECT to check for inadvertent extrahepatic deposition. The ^{99m}Tc-MAA lung shunt was measured by planar scintigraphic imaging, and shunt fractions were determined by region of interest (ROI) analyses (19). If the lung shunt fraction of ^{99m}Tc-MAA was <20% and no other extrahepatic deposition of ^{99m}Tc-MAA was detected, treatment with Ho-MS was performed within 2 weeks.

Data acquisition for dosimetry

For intrahepatic biodistribution assessment of the microspheres, abdominal SPECT and MRI were performed.

MRI

Magnetic resonance images were acquired 1–2 weeks before and 1 week after administration of the therapeutic dose of Ho-MS. Since MRI utilizes the paramagnetic nature of the microspheres rather than the radioactivity, the posttherapy imaging time point was of minor relevance and posttherapy images were acquired during the patients' first weekly visit at the outpatient clinic after treatment. Imaging was performed using a 1.5-T whole body system (Achieva, Philips Healthcare, Best, the Netherlands) equipped with a 16-element torso coil. For detection and quantification of Ho-MS, a multi-slice multi-gradient echo (MGE) sequence was used, acquiring 16 echoes during breath hold with an in-plane resolution of 2 x 2 mm^2 and a slice thickness of 6 mm. Imaging parameters included: Field of view (FOV): 288 x 384 mm^2; number of slices: 45; TR/TE1/ΔTE: 440 ms/1.33 ms/1.15 ms; flip angle: 50°. Sensitivity encoding (SENSE) with a factor of 2.5 was used for acceleration resulting in an imaging time of 3 x 19 s during breath hold. For anatomical information and segmentation purposes, T_2-weighted turbo spin echo (TSE) images were acquired with identical FOV and voxel size. Imaging parameters included: TR/TE: 830 ms/80 ms; SENSE factor: 2; imaging time: 2 x 19 s during breath hold. In addition, T_1-weighted turbo field echo (TFE) images were acquired using an in-plane resolution of 1.8 x 3.6 mm^2; slice thickness: 10 mm; TR/TE: 8.5 ms/4.18 ms; total imaging time: 2 x 14 s during breath hold.

To determine the sensitivity of MRI for Ho-MS, as expressed by the r_2^* relaxivity (relaxation rate per mg/ml Ho-MS), a calibration phantom setup containing known microsphere con-

centrations (0, 2.1, 4.1, 6.1 and 8 mg/ml Ho-MS in agarose gel) was imaged using the MGE sequence described above.

SPECT

Single photon emission computed tomography images were acquired 3–6 days after administration of Ho-MS. The imaging time point did depend on the total activity that was administered to the patient and was based on the maximum tolerated count rate of the SPECT system to acquire images without dead-time effects. The first nine patients underwent imaging using a FORTE™ dual-headed gamma camera (FORTE™, Philips Medical Systems, Milpitas, CA, USA) equipped with gadolinium-153 scanning line sources for transmission CT. The last 6 patients underwent imaging using a Siemens Symbia T16 SPECT/CT system (Siemens, Erlangen, Germany), which combines a dual-headed gamma camera with a 16-slice CT system. Medium energy collimators were used on both systems. Energy windows were set at 80.6 keV (15% window width) for the holmium-166 photo peak and at 118 keV (12% window width) for the correction of downscatter. One hundred twenty projections of 30 s were acquired in a 180° (FORTE) or 360° (Symbia T16) orbit around the liver. Quantitative image data were reconstructed to a 128^3 matrix size with an isotropic voxel size of 4.7 mm^3 (FORTE) or 4.8 mm^3 (Symbia T16), using an ordered subsets expectation maximization algorithm including a hybrid scatter correction method (28), resulting in an absolute quantitative 3D activity distribution in MBq/voxel.

Data analyses

Magnetic resonance images were processed using software code written in MATLAB (MathWorks, Natick, MA, USA). From the MGE MRI patient data, R_2^* values were estimated voxelwise using a monoexponential fitting algorithm weighting all signal amplitudes equally. To minimize the influence of noise, signal intensities lower than 3σ were excluded from the fitting procedure, with σ the standard deviation (SD) of the signal determined in a region with homogeneous signal intensity and free from Ho-MS. R_2^* values were determined for data obtained both before and after RE. For further analysis, the liver was manually segmented based on the tissue contrast of the corresponding T_2-weighted TSE images. The distribution of estimated liver R_2^* values was measured, and the mean R_2^* value together with the SD was calculated.

To determine the change in R_2^* (ΔR_2^*) after therapy, a baseline R_2^* value determined by the mean R_2^* of the liver before Ho-MS administration was subtracted from the post- therapy R_2^* maps. Voxelwise concentrations of Ho-MS were determined from the ΔR_2^* maps by the relationship [Ho-MS] = $\Delta R_2^* / r_2^*$, with r_2^* measured from the calibration phantom set-up. Using the voxel volume and the total volume included in the segmentation, the total amount of Ho-MS in the liver was determined.

For all patients, the MRI-based amount was compared with the total amount that was assumed to be delivered to the liver. This amount was determined by correcting the delivered amount of Ho-MS by the ^{99m}Tc-MAA lung shunt fraction and the amount of Ho-MS left in the administration system. Data from patients who had surgical clips implanted (as a consequence of former partial liver resection) were separated from the patients without clips, and means were also compared separately for these two groups. This separation was made because metallic surgical clips are known to distort gradient echo images (44-46) and hence were suspected to influence MRI-based quantification.
As a final step, the mean radiation absorbed dose was calculated on a whole liver level using MRI and SPECT dose maps that were constructed using the method previously described for an ex-vivo liver model (40). In short, MRI concentration values were converted into MBq/voxel using the voxel size and the specific activity of the microspheres (MBq/mg) at the moment of injection. The SPECT reconstructions provided an absolute quantitative activity in MBq/voxel. Both MRI and SPECT activity maps were convolved with a ^{166}Ho dose point kernel that was calculated using the Monte Carlo code MCNPX (vs. 2.5.0; LANL, Los Alamos, NM, USA) according to the method described in Medical Internal Radiation Dose (MIRD) Pamphlet 17 (47), assuming a tissue density for liver tissue of 1.06 g/cm^3 according to International Commission on Radiation Units and Measurements (ICRU) Report 44 (48). The voxel size of the dose point kernel was equal to the native resolution of the imaging technique (2 x 2 x 6 mm for MRI, 4.7 mm isotropic for SPECT). After manual co-registration of SPECT maps to MRI, and segmentation, mean liver absorbed dose values were calculated for both techniques.

Statistical analysis

Descriptive statistics of means, standard deviations and ranges were calculated for continuous variables. The paired Student's t-test was used for comparison of means (two-tailed 95% confidence interval). Bivariate Pearson's correlation (one-tailed 95% confidence interval) was used for correlation between Ho-MS calculations based on MRI and the actual amount for the whole liver and the correlation between MRI and SPECT dosimetry on a whole liver level. SPSS software (SPSS for Windows, version 13.0; SPSS Inc., Chicago, IL, USA) was used for all analyses.

RESULTS

Fifteen patients were included in this phase I dose-escalation study (Table 1). Nine men and six women, median age 55 years (range 38–87 years), were treated with escalating whole liver doses of 20–80 Gray. The median number of liver tumors was 5 (range 1–21), with a median fractional liver involvement of 14% (range 2–52%), originating from an ocular melanoma (7 patients), colorectal carcinoma (5 patients), cholangiocarcinoma (2 patients) or breast carcinoma (1 patient). Five patients had surgical clips implanted in the liver as a consequence of former partial liver resection (number of clips ranging from 1 to >20). MRI data were analyzed for 14 patients. One patient was excluded from MRI analysis because of incomplete data. The patients received a mean of 523 mg Ho-MS (range 438–640 mg). Corrected for shunting to the lungs (mean 7.4%; range 3.0–13.0%), the mean administered amount of Ho-MS to the liver was 484 mg (range 408–593 mg). Ho-MS caused enhanced MR signal decay after administration, translating into high R_2^* values (Figure 1). Strongly increased R_2^* values were observed locally, corresponding to tumor lesions with high signal intensity on T_2-weighted images.

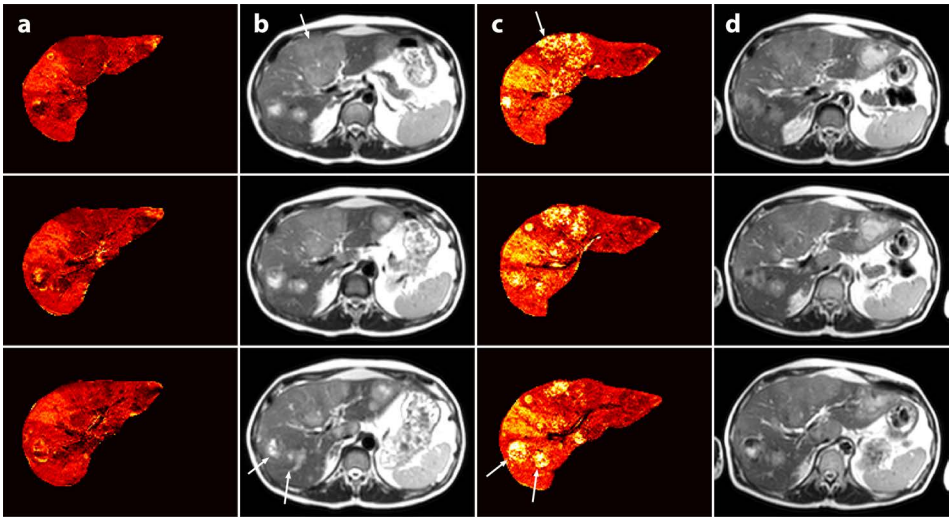

Figure 1 R_2^* maps and SE images (TR/TE: 830 ms/80 ms, flip angle: 90°) before (a+b) and after (c+d) RE. Variations in R_2^* values before RE (a) correspond to variations on SE images (b). After RE, increased R_2^* values were observed at locations with Ho-MS deposition (c), corresponding to tumour lesions with high intensities on SE images (arrows).

Detection of Ho-MS in the whole liver

Subject	Dose cohort (Gy)	nr. of surg. clips	Admin Ho-MS (mg)	R_2^* pre ± SD (s^{-1})	R_2^* post ± SD (s^{-1})	Concentration Ho-MS ± SD (mg/ml)	MRI based Ho-MS in mg (% of admin)		MRI-based dose (Gy)	SPECT- based dose (Gy)
1	20	-	490	excl.	excl.	excl.	excl.	excl.	excl.	9.5
2	20	-	408	28.4 ± 12.4	43.3 ± 21.8	0.14 ± 0.21	467	(115)	12.4	9.1
3	20	5-10	449	31.1 ± 18.6	42.4 ± 36.2	0.11 ± 0.35	287	(64)	6.6	12.5
4	20	-	465	31.8 ± 16.4	45.4 ± 21.2	0.13 ± 0.21	452	(97)	16.4	14.1
5	20	-	489	37.3 ± 24.1	61.4 ± 39.7	0.23 ± 0.39	415	(85)	13.4	11.0
6	20	-	461	30.6 ± 14.8	59.2 ± 23.6	0.28 ± 0.23	447	(97)	15.9	11.9
7	40	10-15	411	33.2 ± 20.3	52.2 ± 36.7	0.18 ± 0.36	291	(71)	19.8	22.2
8	40	-	472	33.9 ± 19.7	52.7 ± 36.2	0.19 ± 0.35	351	(74)	19.4	20.9
9	40	10-15	453	30.9 ± 21.7	50.2 ± 29.8	0.28 ± 0.23	495	(109)	29.5	27.7
10	60	-	501	27.9 ± 15.7	42.2 ± 21.4	0.14 ± 0.21	436	(87)	32.4	36.6
11	60	-	485	31.4 ± 19.6	53.8 ± 32.2	0.23 ± 0.30	457	(94)	41.3	36.9
12	60	>20	478	35.8 ± 34.2	45.3 ± 30.0	0.09 ± 0.29	236	(49)	19.6	37.3
13	80	-	593	29.2 ± 13.8	69.4 ± 56.4	0.39 ± 0.55	597	(101)	59.3	53.1
14	80	1	522	25.5 ± 21.0	41.6 ± 25.7	0.16 ± 0.25	442	(85)	42.0	41.3
15	80	-	591	33.7 ± 16.8	78.2 ± 54.8	0.43 ± 0.53	666	(113)	68.8	55.2

Table1 Acquired biodistribution data of all 15 patients included in the phase I dose-escalation study (20, 40, 60 and 80 Gy). One patient was excluded from MRI analyses because of incomplete data. Data of patients with surgical clips present in the liver are shaded grey. Administered amounts (admin Ho-MS) were determined based on activity measurements of the administration system and lung shunt fraction. R_2^*, concentration and absorbed dose values are mean values over the entire liver.

Histograms of the R_2^* values found in the liver showed an overall shift of R_2^* values toward higher values and a broadening of the R_2^* distribution after treatment (Figure 2). The mean R_2^* values, measured over the entire liver for all patients before treatment (mean 31.5 s^{-1}; range 27.9–37.3 s^{-1}) significantly increased after administration of Ho-MS (mean 52.7 s^{-1}; range 41.6 s^{-1} – 78.2 s^{-1}; $P < 0.001$; Table 1).

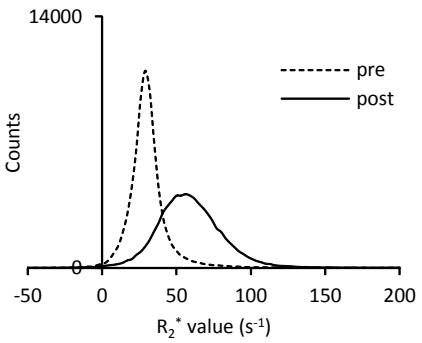

Figure 2 Typical histogram of R_2^* values measured in the whole liver of a patient before (---) and after (—) adminstration of Ho-MS. After administration the curves shifted toward higher values and a broader distribution of R_2^* values was observed.

From the phantom setup, an r_2^* relaxivity of 103 ± 4 $s^{-1}.mg^{-1}.ml$ was measured for the used Ho-MS at 1.5 T, which is in good agreement with the values in the literature (19, 20). This value was subsequently used to calculate Ho-MS concentration maps. The concentration maps were comparable to the R_2^* maps with relatively high concentrations found at tumor sites (Figure 3). From the concentration maps and the volume of the liver, the amount of Ho-MS was calculated. The mean total amount of Ho-MS that was detected in the liver based on MRI was 431 mg (range 236-666 mg). For all patients this was 89 ± 19% (mean ± SD) of the amount delivered to the liver (correlation coefficient $r = 0.7$; $P < 0.01$). By excluding the data of the patients with surgical clips implanted in the liver, the mean MRI-based detected fraction increased to 96 ± 13% (mean ± SD; correlation coefficient $r = 0.8$; $P < 0.01$; Table 1). MRI showed that the presence of surgical clips in the liver led to undetermined areas (black spots) surrounded by (virtual) high concentration values (Figure 4). This led to a poor correlation between Ho-MS amounts calculated on MRI and the actual delivered amount of Ho-MS (correlation coefficient $r = 0.3$; $P = 0.29$).

A good correlation was found between the whole liver mean absorbed radiation dose as assessed by MRI and SPECT (correlation coefficient $r = 0.93$; $P < 0.001$ including all patients, correlation coefficient $r = 0.98$; $P < 0.001$ excluding patients with surgical clips, correlation coefficient $r = 0.81$; $P = 0.10$ for only patients with clips).

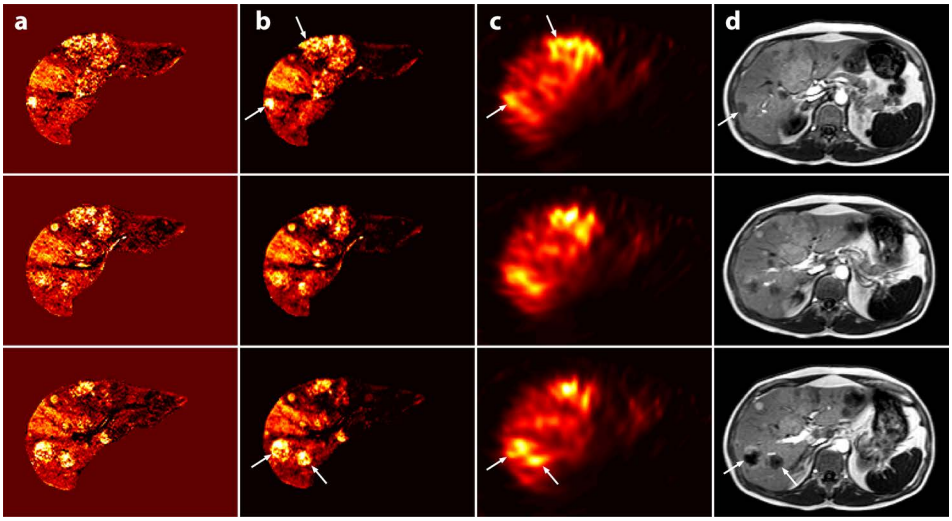

Figure 3 MRI-based concentration maps (a) after Ho-MS administration, MRI-based absorbed dose maps (b) together with their corresponding SPECT images (c) and T_1-weighted images (d) (TR/TE: 8.5 ms/4.18 ms, flip angle: 10°). The concentration maps were constructed from normalised R_2^* maps by using the r_2^* relaxivity of Ho-MS. MRI-based dose maps were constructed by applying a dose point kernel after conversion of concentrations Ho-MS into MBq/voxel. MRI-based concentration and absorbed dose correspond to the activity distribution on the SPECT images (c), and the tumour sites on T_1-weighted images (d) (arrows).

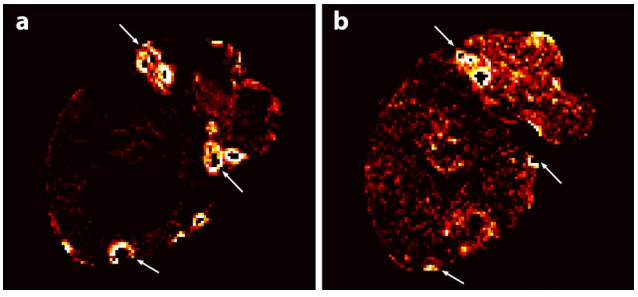

Figure 4 MRI-based Ho-MS concentration maps before (a) and after (b) radioembolization in a patient with multiple surgical clips after partial liver resection. At the location of the clips (arrows), quantification failed (black spots), while in the near vicinity extremely high concentration values were found (white rings).

Magnetic resonance imaging displayed the local microsphere distribution in much more detail because of the relatively high in-plane resolution, for example revealing an absence of Ho-MS in the central part of a furthermore highly targeted tumor in some cases. This situation was rather obscured in the corresponding SPECT images owing to the lower resolution and blurring effects (Figure 5).

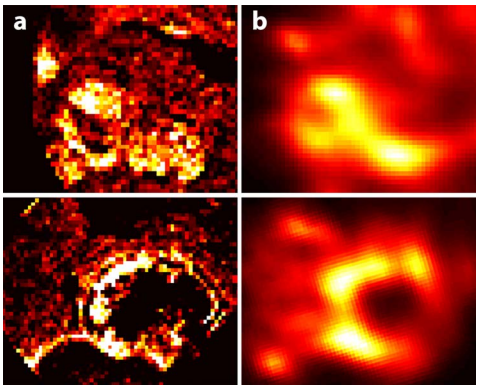

Figure 5 Ho-MS deposition around tumours. MRI-based concentration maps (a) show more detail (higher resolution) about the distribution of the microspheres than the SPECT-based activity maps. The Ho-MS are primarily distributed in the peripheral parts of the tumour (a). This is less pronounced on the SPECT images (b).

DISCUSSION

In this chapter we presented the first in vivo quantitative MRI data of ^{166}Ho-poly(L-lactic acid) microspheres for image-guided radioembolization using MRI.

Three-dimensional MRI-based assessment of the intrahepatic biodistribution of Ho-MS was feasible. Ho-MS concentration maps, which were constructed by using a time series of T_2^*-weighted images, clearly showed the ability of MRI to visualize the intrahepatic biodistribution of the microspheres. Furthermore, MRI provided both a quantitative measure of the Ho-MS distribution and anatomical information, enabling direct localization of the microsphere deposition within the tissue. MRI detected 89% of the actual delivered Ho-MS in the whole liver. The mean whole liver absorbed radiation dose calculated on MRI correlated very well with the absorbed radiation dose on SPECT. A more detailed intra-tumor biodistribution assessment was possible using MRI compared with SPECT because of the better spatial resolution of MRI. The quantitative nature of MRI-based biodistribution assessment of Ho-MS allows for personalized dosimetry in vivo and may ultimately lead to optimization of radioembolization with regard to safety and efficacy.

Compared with the actual administered amount of Ho-MS in the liver, determined based on the injected amount and taking into account the ^{99m}Tc-MAA-based lung shunt fraction, the MRI quantification method presented in this work showed on average an underestimation. As shown, this was in part due to the presence of surgical clips (Figure 4). These clips induced field distortions, resulting in large MR signal voids surrounded by large R_2^* values. Therefore, locally the amount of Ho-MS cannot be determined resulting in an underestimation of the microsphere amount in the vicinity of the clips. Although the presence of surgical clips does not necessarily lead to a contraindication for MRI-based dosim-

etry, biodistribution measurements in the vicinity of the clips should be interpreted with care. Another source of the discrepancy between the MRI-based amount and the amount delivered may be the use of ^{99m}Tc MAA as a predictor of the lung shunt fraction. Although used to correct for extra-hepatic deposition in order to estimate the Ho-MS liver amount, it is known that, because of a number of dissimilarities between ^{99m}Tc MAA and Ho-MS such as size, shape and density, ^{99m}Tc MAA is not the optimal microsphere analogy (8). Incorrect assessment of the lung shunt fraction may have led to an erroneous estimation of the amount of Ho-MS delivered to the liver. This explanation is supported by the good correlation that was found between the MRI-based mean liver absorbed dose and the absorbed dose based on the more conventional method of image-based dosimetry, SPECT.
Quantification errors may also arise from the need to correct for baseline R_2^* values in order to determine ΔR_2^*. ΔR_2^* values were calculated by subtracting the mean liver R_2^* value before administration from the posttreatment R_2^* maps. Because of the variance of R_2^* in the absence of microspheres as a result of tissue characteristics (Figure 1), over- or underestimations will be introduced at the voxel level. The bias introduced in ΔR_2^* will depend on the local voxel R_2^* value with respect to the mean R_2^* over the whole VOI. In addition to these variations over space, changes may occur in tissue T_2 in the time interval between pre- and posttherapy imaging. Such changes may occur, for example, because of short-term therapy-induced edema (49) which leads to increasing T_2 values, and thus decreasing R_2 values, owing to the higher water content as is generally reflected by hyperintense areas on T_2-weighted images (50). A decrease in tissue R_2 may therefore counteract the increase in R_2^* because of Ho-MS leading to an underestimation of Ho-MS concentration. To minimize these quantification errors, voxel-based subtraction of post- and pretherapy maps seems to be crucial. Manual or (semi-) automatic registration of these maps may partly solve the problem, but a more robust solution will be to integrate MR imaging as part of the RE procedure. Data needed to construct the concentration maps shown in this work were acquired within 1 minute, and data processing can be performed within several minutes. Considering this short time scale, it is feasible to perform personalized MRI-based dosimetry during the actual RE procedure. This would enable fast verification and give the opportunity, if necessary, to immediately adjust the RE procedure. Moreover, MRI would enable monitoring of the administration of the Ho-MS in real time. This has previously been demonstrated in a pig model (31).
The first MRI data of patients treated with ^{166}Ho-poly(L-lactic acid) microspheres show the feasibility of MRI-based dosimetry for radioembolization. Intrahepatic microsphere biodistribution can be visualized with great detail, and a good quantitative measurement of the absorbed radiation dose can be obtained within several minutes of the radioembolization procedure. Biodistribution assessment in the vicinity of surgical clips should be interpreted with care.

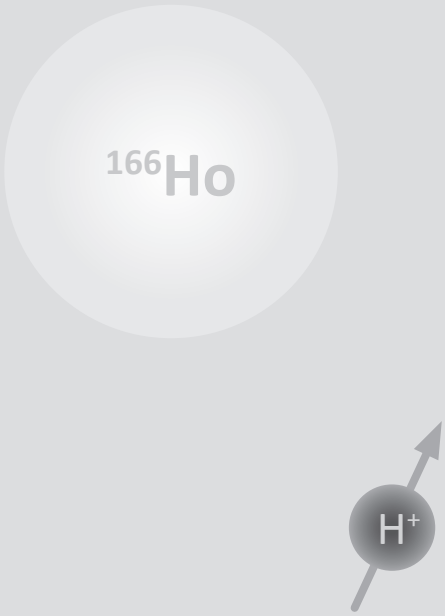
166Ho
H+

Chapter 3

S_0-fitting: estimating high local concentrations

"In this chapter, a post-processing strategy is presented, S_0-fitting, that provides a best estimate of R_2^* values irrespective of how fast the signal decays."

Based on:

van de Maat GH, Seevinck PR, Bos C, et al. Quantification of holmium-166 loaded microspheres: estimating high local concentrations using a conventional multiple gradient echo sequence with S_0-fitting. J Magn Res Imag 2012;35:1453-1461

INTRODUCTION

Internal radiation therapy using radioactive holmium-166 loaded microspheres (Ho-MS) is a novel and promising technique for treatment of liver metastases (26, 42, 51). In this embolization therapy, accurate assessment and quantification of the biodistribution of the microspheres is of major importance for treatment planning, dosimetry and follow-up (37). Due to the paramagnetic nature of holmium, the microspheres can be detected by magnetic resonance imaging (MRI) using the induced T_2^* signal decay (37, 38). Previously, MR T_2^* relaxometry has been shown to enable high-resolution imaging of the biodistribution of the microspheres in the liver (37, 38, 52). It has also been demonstrated that for quantitative T_2^* measurements of Ho-MS, the favorable imaging strategy is multiple gradient echo (MGE) sampling of the free induction decay (FID) since it minimizes the influence of diffusion as compared with sampling of the spin echo envelope (53). By a monoexponential fit to the subsequent echoes of an MGE data set, accurate R_2^* values have been obtained over a broad range of Ho-MS concentrations in vitro. Furthermore, using an MGE strategy has been shown to enable quantification of Ho-MS in patients within a clinically feasible scanning time (54).

In practice, the upper limit of the detectable R_2^* ($R_2^* = 1/T_2^*$) range and consequently of the detectable concentration of the Ho-MS is mainly determined by the minimal echo time (TE_{min}), the echo spacing (55, 56), and the parameters governing SNR that can be obtained. However, minimal echo times and intervals between successive gradient echoes in conventional MGE sampling schemes that can be obtained on clinical scanners are relatively long (~1 ms). This limits the accuracy by which rapidly decaying signals can be sampled (52, 55-58) and, as a consequence, complicates the quantification of high concentrations of Ho-MS since high R_2^* values cannot be characterized. To use MRI-based biodistribution measurements for, e.g., dosimetric calculations, these high concentrations are of major importance since they largely contribute to the local deposited dose. For this reason, it is essential to at least obtain a best estimate of the R_2^* value of voxels containing such high concentrations.

In this chapter, a post-processing strategy is presented, S_0-fitting, that provides a best estimate of R_2^* values irrespective of how fast the signal decays. S_0-fitting incorporates the estimated initial amplitude of the FID curve, S_0 (S at t = 0 ms), of neighboring voxels into the fitting algorithm of voxels for which the initial conventional fitting procedure failed. Incorporation of S_0 assumes that the S_0-value of neighboring voxels is representative for the S_0-value of the problematic voxels. This assumption is made based on 1) the structure of liver tissue, which is known to be fairly homogeneous and 2) the minor influence of the presence of Ho-MS on S_0. The second argument is theoretically valid since Ho-MS have

a negligible influence on T_1 (38) and the maximum expected concentrations of Ho-MS in vivo correspond to a voxel volume fraction of ~1%.
To validate the assumptions that are made, to evaluate the accuracy of the model, and to show the benefits of applying S_0-fitting, experiments were carried out on a phantom setup that contained a wide range of Ho-MS concentrations, and on an ex vivo rabbit liver to which Ho-MS were administered. S_0-fitting was applied to MGE data that was acquired and the results were compared with ultrashort echo time (UTE) (59-61) imaging, which was chosen as an image-based reference standard because of its ability to sample rapidly decaying signals (62, 63).

MATERIALS AND METHODS

To investigate the validity and accuracy of using a monoexponential signal decay model for quantification of Ho-MS, quantitative ultrashort echo time (qUTE) imaging was performed on the phantom setup. qUTE utilizes an acquisition scheme that is composed of several interleaved UTE acquisitions that was recently successfully applied to assess the distribution of Ho-MS in vitro (52). Using the qUTE data set, R_2^* values were determined for the entire range of concentrations Ho-MS and the r_2^* relaxivity of Ho-MS was derived from these values. This r_2^* value was used as the reference standard for further measurements. Second, the influence of the presence of Ho-MS on estimated S_0 values was investigated using conventional MGE data of the phantom setup. Third, R_2^* values and the r_2^* relaxivity of Ho-MS were estimated from conventional MGE data of the phantom setup with and without S_0-fitting. These values were compared quantitatively with R_2^* values and the r_2^* relaxivity of Ho-MS obtained with qUTE to evaluate the accuracy of the S_0-fitting algorithm. Finally, S_0-fitting was applied to an ex vivo rabbit liver containing Ho-MS and resulting R_2^* maps were compared qualitatively and quantitatively with R_2^* maps obtained with UTE imaging.

Phantom and specimen preparation

Ho-MS gel phantom
Ho-MS were prepared as described by Nijsen et al (27), resulting in Ho-MS with a density of 1.4 g/ml, a size distribution of 20-50 µm (mean diameter 30 µm) after sieving and a holmium content of 18.7% by weight. An agarose gel (2% w/w) series containing Ho-MS concentrations ranging from 0-15 mg/ml was created, providing a wide range of R_2^* val-

ues. $MnCl_2$ was added to the native gel to mimic the relaxation properties of liver tissue. Samples were sealed in tubes and placed parallel to the main magnetic field.

Ex vivo rabbit liver

An excised rabbit liver was extensively perfused through the hepatic artery using ($MnCl_2$-doped) saline to remove the blood volume. Subsequently, the liver was stored in saline. The hepatic artery was cannulated using a small injection tube. Through this tube Ho-MS were administered and the liver was perfused again. MRI was done prior to and after administration.

Data acquisition

MRI was performed on a 3T whole body system (Achieva, Philips Medical Systems, Best, the Netherlands). R_2^* estimation was done using two different MRI sequences: 1) conventional MGE (Cartesian) imaging, sampling the FID, and 2) qUTE imaging with MGE (radial) sampling of the FID, which consists of a series UTE-MGE acquisitions in an interleaved fashion in which the entire readout echo train is shifted systematically to ultra-densely sample the decaying MR signal, as depicted schematically in Figure 1.

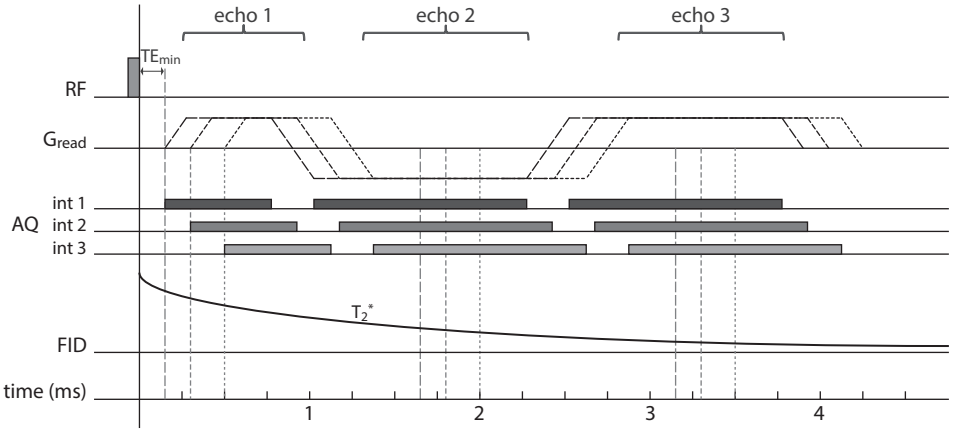

Figure 1 3D qUTE sampling scheme, incorporating three gradient echoes and three interleaved acquisitions with shifted echo trains. The UTE acquisition (echo 1) is a half echo, the later echoes are full echoes. The echo time of the first echo is defined as the interval between the end of the RF excitation pulse and the beginning of the acquisition window. In this example, echo times of the three echoes of the first interleaved acquisition were 0.15, 1.65, and 3.15 ms, resulting in an echo spacing of 1.50 ms. The complete second and third echo trains were shifted with respect to the first echo train over a time period of 0.15 ms and 0.35 ms, resulting in echo times of 0.3, 1.8, 3.3 ms, and 0.5, 2.0, 3.5 ms, respectively. In practice, six interleaves were used, resulting in a densely sampled FID signal.

Ho-MS gel phantom

To verify the monoexponentiality of the signal decay and to determine the R_2^* reference standard values of concentrations Ho-MS, qUTE imaging was performed using an anisotropic 3D radial sampling scheme with a field of view (FOV) = 160 x 160 x 150 mm^3; scan matrix = 128 x 128 x 15; reconstruction matrix = 160 x 160 x 15; bandwidth per pixel = 867 Hz and TR/ΔTE/flip = 13.5/1.5 ms/10°. Seven gradient echoes were acquired. Six interleaves were applied with a minimal TE of, respectively, 0.15, 0.2, 0.3, 0.5, 0.8 and 1.2 ms, allowing detailed assessment of the signal decay time course of fast decaying signals. The scan time of each interleave was 2m12s, leading to a total scan time of 13 minutes. For investigating the influence of the presence of Ho-MS on S_0 and to apply the S_0-fitting method, 2D Cartesian MGE imaging was performed using 15 echoes without additional interleaves. Scan parameters included TR/TE1/ΔTE = 200/1.42/1.2 ms; FOV = 160^2 mm^2; scan matrix = 128^2; reconstruction matrix = 160^2, flip angle = 45° and bandwidth per pixel = 1377 Hz.

Ex vivo rabbit liver

qUTE imaging was performed using a 3D acquisition scheme with FOV = 128^3 mm^3; scan matrix/reconstruction matrix = 128^3; bandwidth per pixel = 856Hz and TR/ΔTE/flip = 11/1.6 ms/8°, acquiring five echoes. Five interleaves were applied with a minimal TE of, respectively, 0.08, 0.15, 0.3, 0.6 and 1.10 ms resulting in a total scan time of 30 minutes. Furthermore, multi slice MGE sampling (Cartesian) was performed with a FOV = 128 x 128 mm^2, scan matrix/reconstruction matrix = 128^2, slice thickness = 2 mm, 26 slices, and bandwidth per pixel = 1002 Hz. Further imaging parameters included TR/TE_1/ΔTE/flip = 354/1.9/1.36 ms/40°, acquiring eight echoes without additional interleaves, resulting in a total scan time of 49 seconds.

Data analysis

Data was analyzed using Matlab 2009 (Mathworks, Natick, MA). Conventional R_2^* estimation was done according to the following procedure. A monoexponential least-squares fitting algorithm, weighing small and large signal amplitudes equally (64), was used to estimate R_2^* and S_0 for each image pixel. A truncation model was used incorporating a signal-to-noise ratio (SNR)-threshold criterion to exclude echo time points with low SNR (65) to prevent the influence of a Rician noise distribution in MR magnitude images at low SNR (66). An SNR-threshold of $S>3\sigma$ was used, with σ the standard deviation of the signal determined for all gradient echo images in a region with homogeneous signal intensity and absence of Ho-MS on visual inspection. In case less than two data points met the SNR-threshold, no R_2^* and S_0 value was estimated, a value of zero was assigned to the R_2^* map, and the voxel was subjected to S_0-fitting. After the conventional fitting procedure,

resulting R_2^* maps were inspected and voxels with a negative value were also subjected to S_0-fitting.

For S_0-fitting two processing steps were added. In the first step, for pixels for which the conventional fitting procedure failed and no R_2^* and S_0 value were determined, an S_0 value was estimated. For the phantom setup this was done using the mean S_0 value of the samples to which the initial fitting procedure was successfully applied. For the ex vivo rabbit liver, S_0 was estimated by averaging S_0 values of neighboring pixels using a region-growing method. Starting with a selection region of 3 x 3 pixels surrounding the undetermined pixel, pixels were selected that fulfilled the threshold criterion mentioned above. The selection region was extended until at least 4 pixels were included. From these included pixels an average S_0 was determined and assigned to the undetermined pixel. In the second step, the estimated value of S_0 was used to estimate an R_2^* value. For this procedure two cases were distinguished: In case no data point met the SNR-threshold, the R_2^* value that can maximally be estimated based on noise level and echo time was assigned to the particular pixel, according to $R_{2\,lim}^* = \ln(S_0/3\sigma)/TE_1$. Here the assumption is made that the MR signal decayed from S_0 to below the SNR threshold (3σ) in a time period $t = TE_1$. This $R_{2\,lim}^*$ also represents the minimum lower bound of the estimate so the actual R_2^* value of that voxel might be even higher. In all other cases, R_2^* was estimated by fitting the monoexponential function to the estimated S_0 and available original data points.

Ho-MS gel phantom

Monoexponentiality of aqueous systems containing Ho-MS was investigated using mean region of interest (ROI) (225 pixels) data of the Ho-MS dilution gel samples acquired with qUTE. Furthermore, R_2^* values of this dataset were determined pixelwise and from these values the r_2^* relaxivity of Ho-MS was investigated using ROI (225 pixels) values. Pixelwise R_2^* estimation was also done using MGE data with S_0-fitting and using MGE data without S_0-fitting. For the S_0-fitting method, the mean S_0 value of the samples that were successfully characterized by conventional fitting was used since the region-growing method would not work on the phantom setup because the samples were separated by air. Resultant R_2^* values were displayed in regression curves and compared with the reference standard (qUTE). Estimated S_0 values from MGE data were investigated to verify the assumption that the presence of Ho-MS does not influence S_0.

Ex vivo rabbit liver

R_2^* values were estimated voxel wise from conventional MGE data and qUTE data prior to and after administration of Ho-MS. For MGE data acquired after administration of Ho-MS, S_0-fitting was applied in addition using the region-growing method. To compare the results in a quantitative way, the R_2^* values were used to determine the detected Ho-MS

content per voxel for the three different cases: qUTE, MGE without S_0-fitting, and MGE with S_0-fitting. The Ho-MS content was determined according to:

$$HoMS\ content = \frac{R^*_{2,post} - R^*_{2,pre}}{r^*_2} \cdot V_{voxel} \qquad [1]$$

where $R_2^*{}_{post}$ is the R_2^* value after administration of Ho-MS, $R_2^*{}_{pre}$ is the R_2^* value prior to Ho-MS administration, V_{Voxel} is the voxel volume, and r_2^* is the relaxivity of the Ho-MS.

RESULTS

MR experiments: Ho-MS gel phantom

Monoexponentiality

Densely sampled qUTE data (mean ROI data) were used to characterize the Ho-MS induced signal decay in great detail over the entire MR signal range from S_0 toward noise level (Figure 2a). Monoexponential behavior was found as observed from the linear relation between the logarithm of the signal and the echo time over a wide range of Ho-MS concentrations (1-15 mg/ml) for signals above the SNR-threshold criterion. Conventional pixelwise R_2^* estimation could be achieved for all concentrations for the qUTE data set (Figure 2c). A linear relation between R_2^* and Ho-MS concentration was found (Figure 2b), representing an r_2^* relaxivity of 200 ± 10 $s^{-1}.mg^{-1}.ml$ for Ho-MS at 3T.

Conventional fitting of MGE data

R_2^* estimation by conventional fitting of MGE data could be achieved up to a Ho-MS concentration of 5 mg/ml (Figure 3a). This corresponds to a maximum detectable R_2^* value of about 1000 s^{-1}. A linear fit of mean ROI R_2^* values in this well-defined range of 0-1000 s^{-1} provided an Ho-MS r_2^* relaxivity of 208 ± 24 $s^{-1}.mg^{-1}.ml$ (Figure 4a), which is similar to the value determined from qUTE data (200 ± 10 $s^{-1}.mg^{-1}.ml$). Estimated values of S_0 in this range showed constant behavior (Figure 4b) with a mean S_0 value of 3433 (a.u.) and standard deviation of 79 (2.3%), which confirms the assumption that Ho-MS has negligible influence on S_0. Although the S_0 values were rather constant, their standard deviation increased for higher concentrations since fewer data points were available for estimation.

Influence of S_0-fitting on R_2^* estimation

Applying S_0-fitting on MGE data using the mean estimated S_0 of the other samples provided a best estimate for R_2^* up to a value of about 2300 s^{-1} compared with a maximum value of about 1000 s^{-1} that could be characterized using conventional fitting (Figures 3b, 4c). This value corresponds to a Ho-MS concentration of about 11.5 mg/ml assuming a relaxivity r_2^* = 200 $s^{-1}.mg^{-1}.ml$. This maximum R_2^* value is determined by the estimated S_0, the image noise, and the minimum echo time of the MGE dataset ($R_{2\,lim}^* = \ln(S_0/3\sigma)/TE_1$). A linear fit to the S_0-fitted R_2^* values (mean ROI values) in the range 0-10 mg/ml Ho-MS, provided a Ho-MS relaxivity of 206 ± 12 $s^{-1}.mg^{-1}.ml$. In comparison, qUTE data provided a relaxivity of 205 ± 16 $s^{-1}.mg^{-1}.ml$ over the same range (Figure 4d).

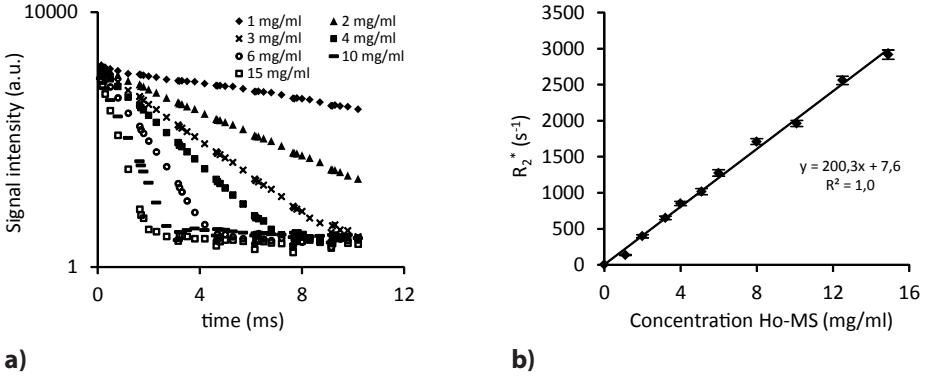

Figure 2 a) Log MR signal as a function of echo time for a range of Ho-MS utilizing qUTE imaing. For visualization, only data from a selection of samples is shown. For all concentrations, a linear relation is observed for the MR signal as a function of echo time for all signals above the SNR threshold. b) A linear relation between R_2^* and Ho-MS concentration is observed, resulting in an r_2^* relaxivity of 200 ± 10 $s^{-1}.mg^{-1}.ml$ for Ho-MS at 3 T.

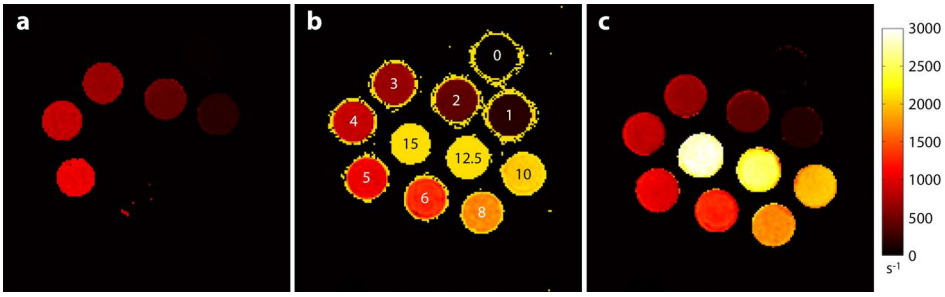

Figure 3 R_2^* maps of the Ho-MS gel phantom determined with conventional R_2^* estimation of MGE data (a), with S_0-fitting of MGE data (b), and conventional R_2^* estimation of qUTE data (c). As a result of S_0-fitting, $R_{2\,lim}^*$ was assigned to the entire background in (b). For visualization, maps are masked to exclude these background R_2^* values. However, some background values are still present causing yellow rings around the samples. A good agreement is shown between qUTE data (c) and S_0-fitted MGE data (b) for Ho-MS concentrations up to 10 mg/ml ($R_2^* \sim 2100\ s^{-1}$). For higher concentrations, S_0-fitting results deviate from qUTE results.

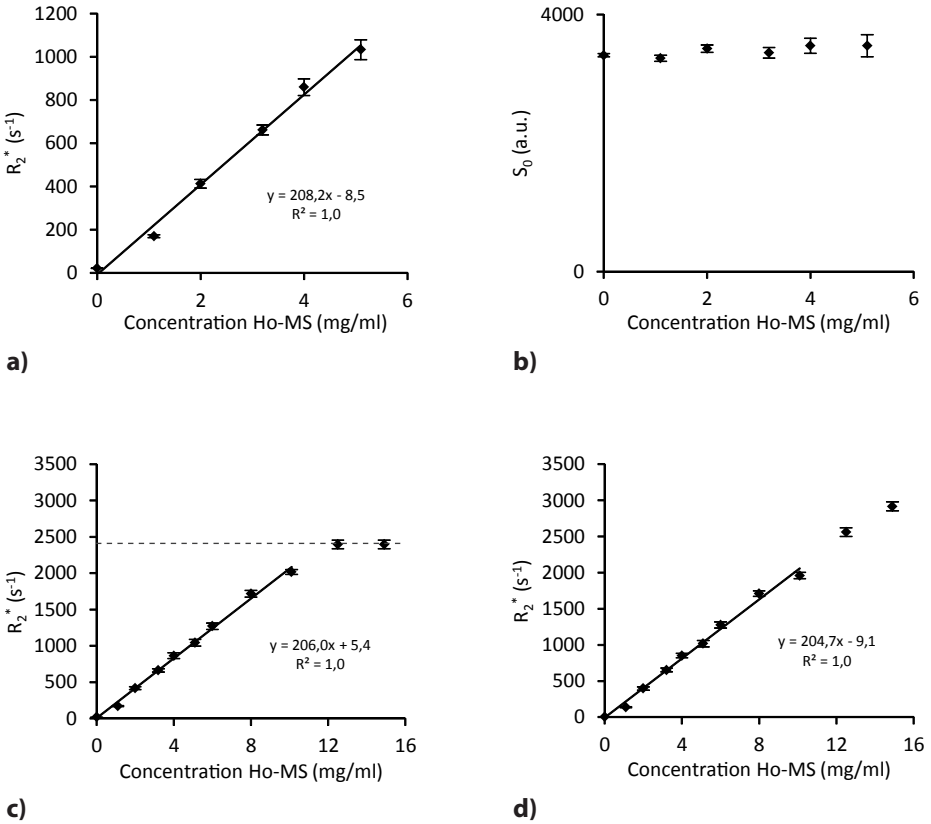

Figure 4 R_2^* regression curves obtained with conventional R_2^* estimation of MGE data (a), S_0-fitting of MGE data (c), and conventional R_2^* estimation of qUTE data (d). S_0 values, estimated by conventional R_2^* fitting, are shown in (b). R_2^* regression curves were linearly fitted to estimate the r_2^* relaxivity. Ho-MS concentrations of 12.5 and 14.9 mg/ml were excluded from the linear fit since their R_2^* values were higher according to qUTE measurements than the maximum value of 2300 s^{-1} that could be characterized by the S_0-fitting method.

MR experiments: Ex vivo rabbit liver

MGE and qUTE data acquired before and after administration of Ho-MS to the ex vivo rabbit liver are shown in Figure 5. Prior to Ho-MS administration, homogeneous signal intensity in the liver was shown by the first echo (1.9 ms) of the MGE image series (Figure 5a). After Ho-MS administration, large signal voids due to signal dephasing were observed (Figure 5b). As a result, signal decay could not be characterized for several voxels using conventional R_2^* estimation since fewer than two data points met the SNR threshold ($S>3\sigma$). These voxels are indicated in Figure 5c (white pixels). On the first UTE image (Figure 5d), signal dephasing was much less due to the very short echo time (0.15 ms). For

the qUTE dataset, all voxels met the threshold criterion and R_2^* values could be estimated by conventional R_2^* fitting.

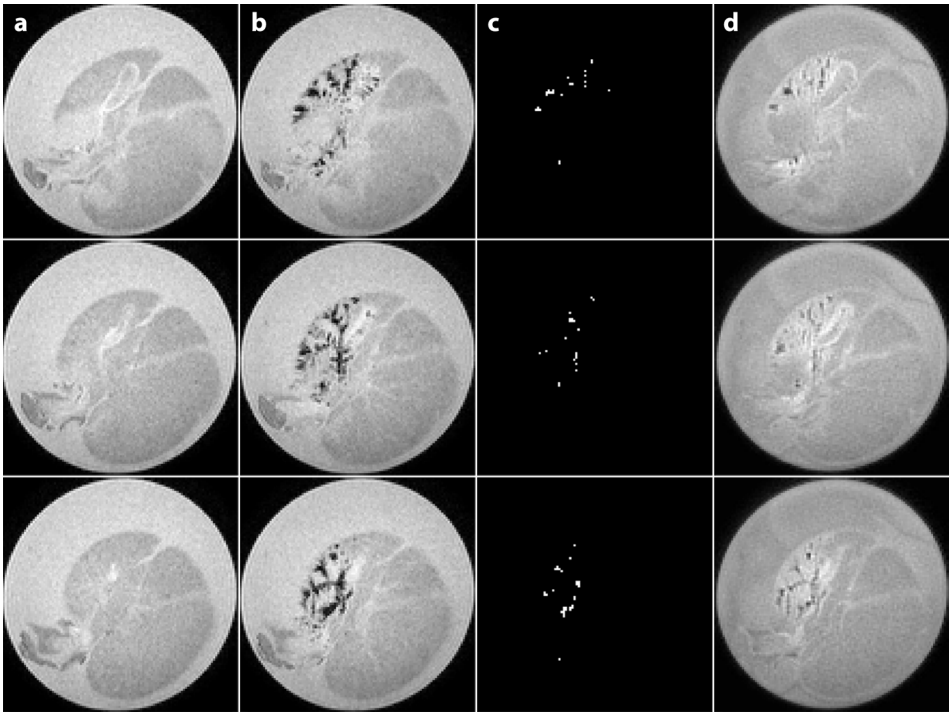

Figure 5 Three typical imaging slices of the ex vivo rabbit liver. First echo of the MGE series (TE = 1.9 ms) before (a) and after (b) administration of Ho-MS, pixels for which the conventional R_2^* fitting procedure failed (white pixels) (c) and first echo of the qUTE series (TE = 0.08 ms) after administration of Ho-MS (d). Fairly homogeneous signal intensity in the liver is observed in the gradient echo images in the absence of Ho-MS. After administration of Ho-MS, signal dephasing is clearly visible in the conventional gradient echo images (b), but less pronounced in the images of the qUTE dataset (d). R_2^* fitting was not possible for several voxels of the MGE series (c) in constrast to qUTE data, where all voxels complied with the SNR threshold criterion.

Influence of S_0 estimation on R_2^* maps

Conventionally fitted R_2^* maps of MGE data before and after administration of Ho-MS are shown in Figure 6a, b. The presence of Ho-MS clearly leads to higher R_2^* values. The black areas visible in Figure 6b indicate locations where R_2^* determination failed because of low SNR. These areas are mainly located near high concentrations of Ho-MS, as can be appreciated from the high R_2^* values in the neighborhood. By applying S_0-fitting, R_2^* values were estimated also for the problematic voxels, which is clearly visible in the resulting R_2^* maps (Figure 6c). The black areas that were visible in the original R_2^* maps at locations where the conventional fitting algorithm failed now have an estimated R_2^* value. Compared with

R_2^* maps determined by conventional R_2^* fitting of qUTE data (Figure 6d), a good correspondence is shown.

To determine the increase of the R_2^* value per voxel, R_2^* maps prior to administration of Ho-MS were subtracted from R_2^* maps after Ho-MS administration, both for conventionally fitted and S_0-fitted data. The same was done for the R_2^* maps determined from qUTE data. Next, the total amount of Ho-MS per slice was determined for the three cases using Equation [1] with r_2^* = 200 $s^{-1}.mg^{-1}.ml$ and V_{voxel} = 0.002 ml. The calculated amounts for the slices shown in Figure 6 were successively 1.24, 1.15 and 0.88 mg for conventional fitted MGE data, 1.38, 1.26 and 1.05 mg for S_0-fitted MGE data, and 1.40, 1.28 and 1.19 mg for qUTE data. The total amount of Ho-MS that was found in all the imaging slices was 7.21mg, 8.20mg, and 8.26 mg for, respectively, conventional fitted MGE data, S_0-fitted MGE data, and qUTE data. Taking qUTE results as the reference standard, applying conventional R_2^* fitting resulted in detection of 87.3% of the Ho-MS on average, where for S_0-fitting this percentage increased to 99.3%.

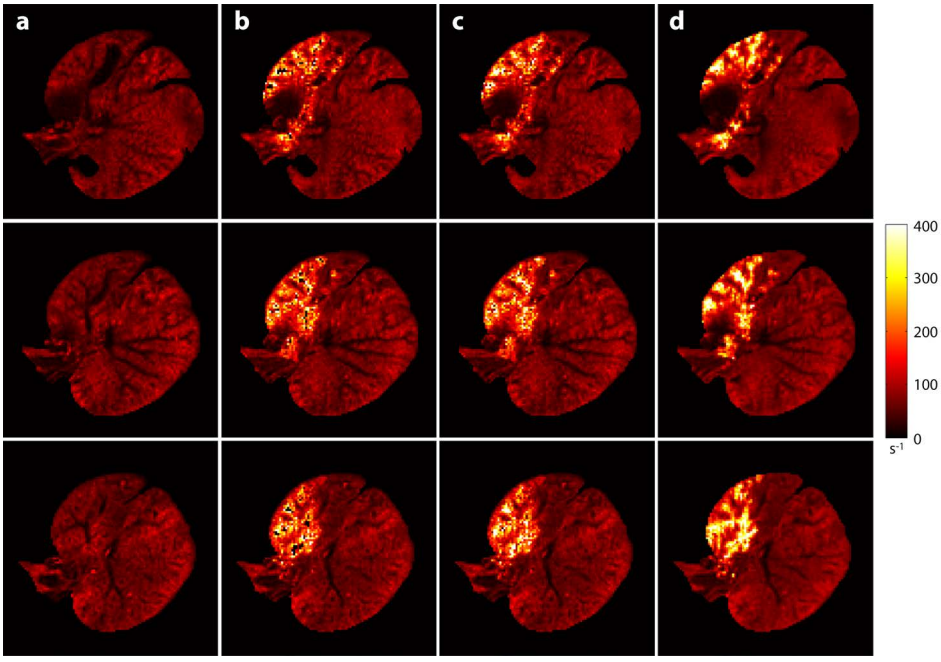

Figure 6 R_2^* maps of the three image slices displayed in Figure 5. Conventional fitted R_2^* maps of MGE data before (a) and after (b) administration of Ho-MS; (c) S_0-fitted R_2^* maps of MGE data; and (d) conventional fitted R_2^* maps of qUTE data. The presence of Ho-MS clearly leads to higher R_2^* values for MGE data as well as qUTE data. Black areas at locations where the conventional fitting algorithm failed, visible in (b) are filled with estimated R_2^* values after S_0-fitting (c). A good qualitative agreement is observed between S_0-fitted data and qUTE data, although the UTE images are more blurred because of the radial readout.

DISCUSSION

The potential of MRI to detect and quantify Ho-MS is of major importance to investigate the biodistribution of the microspheres after hepatic arterial radioembolization. For investigating therapeutic effects of radioembolization, accurate biodistribution measurements are necessary since they provide a base for dosimetric calculations. However, high concentrations of microspheres that can be present after embolization cause transverse signal decay to be so rapid that accurate signal characterization using conventional MGE sampling is a difficult task. In this chapter a post-processing method was presented intended to provide a best estimate of the R_2^* value of these rapidly decaying signals and hence of the local concentration Ho-MS. The method, S_0-fitting, was demonstrated and evaluated on a well-defined phantom setup and its benefits were shown by applying the method on an ex vivo rabbit liver containing Ho-MS.

S_0-fitting incorporates estimated S_0-values of well-characterized neighboring voxels into the monoexponential fitting algorithm that is used to estimate R_2^* values of voxels where the initial conventional fitting algorithm fails because of high concentrations Ho-MS. For quantification of Ho-MS in liver tissue, monoexponential signal decay was assumed. The legitimacy of this assumption was demonstrated in vitro over a wide range of Ho-MS concentrations using qUTE imaging; an interleaved radial MGE sampling strategy which is extremely useful for high R_2^* estimation due to its ultrashort echo times and sampling intervals (60, 61). From the UTE data, a linear relation was found between concentration Ho-MS and R_2^* over a concentration range of 0-15 mg/ml, resulting in a linear relaxivity r_2^* of 200 ± 10 $s^{-1}.mg^{-1}.ml$ at 3 T. R_2^* estimation using conventional MGE data without S_0-fitting demonstrated a similar relaxivity; however, R_2^* values could only be characterized over a Ho-MS concentration range of 0-5 mg/ml. Applying S_0-fitting increased this range by providing a best estimate of the R_2^* values up to 2300 s^{-1}. Resulting R_2^* values and r_2^* relaxivity showed very good correspondence with values obtained using qUTE, from which it can be concluded that S_0-fitting provides an accurate estimation of R_2^* over this range. Differences in r_2^* seem to be largely determined by the range of included Ho-MS and not by the imaging or processing method. R_2^* maps of an ex vivo rabbit liver containing Ho-MS, constructed using conventional MGE data with and without S_0-fitting, were compared qualitatively to qUTE R_2^* maps. R_2^* estimation using MGE data without S_0-fitting was unable to estimate R_2^* in areas with high Ho-MS concentrations. The S_0-fitting method, however, allowed R_2^* estimation in the entire tissue of interest and the estimated R_2^* maps were in good agreement with the R_2^* maps estimated using qUTE data. The detected amount of Ho-MS increased from 87.3% for conventional R_2^* fitting to 99.3% for S_0-fitting compared with conventional fitting of qUTE data. An overall improvement of the

quantification of Ho-MS was accomplished.

The exponential fitting algorithm applied throughout this study was based on a truncation model (65), incorporating a minimal threshold criterion to include data points to the fitting algorithm. This criterion was made very strict, S>3σ, to prevent any influence of the Rician noise distribution of the MR magnitude signal at low SNR. At least two data points needed to fulfill the threshold criterion to allow R_2^* estimation, otherwise R_2^* was set to zero. Less stringent criteria may seem to increase the detectable R_2^* range; however, it was shown in the literature that this may lead to an underestimation of R_2^* values and will decrease the overall reliability of the R_2^* estimation (66). To apply S_0-fitting, only a single measured data point had to fulfill the threshold criterion, which was then used together with the estimated S_0 value from surrounding pixels to perform exponential fitting and R_2^* estimation. In case the signal decay was so rapid that even the first data point was below the SNR threshold, the value of $R_{2\,lim}^*$ was assigned to the voxel. This calculated upper detection limit depended on the estimated value of S_0, the value of the threshold criterion (3σ) and the echo time of the first acquired sample point, TE_1, as defined earlier. For the multislice MGE sequence used throughout this study, $R_{2\,lim}^*$ was ~2300 s^{-1} (Figure 4c), which corresponds to a Ho-MS concentration of ~11.5 mg/ml.

Some limitations of the S_0-fitting method have to be considered. Since S_0-fitting is based on the assumption that S_0 values of neighboring voxels are representative for the S_0 value of the voxels for which the method is used, MRI data to which the method is applied should meet this condition. Considering the structure of liver tissue, the negligible effect of Ho-MS on T_1, and the low volume fractions of Ho-MS in a voxel, this condition will be met locally when the method is applied for the quantification of Ho-MS in the liver. Even in the case of concentrations of 15 mg/ml, the Ho-MS volume fraction will only be 1.1%, and thus will have a minor influence on the proton density. This was also confirmed by the fairly homogeneous signal intensity prior to administration of Ho-MS (Figure 5a), and the absence of the influence of Ho-MS on S_0 as demonstrated in Figure 4b. Potential effects of macroscopic variances in S_0 due to B_0 and B_1 inhomogeneities that might have been present were minimized by using only S_0 values of voxels in the near vicinity of the undetermined voxels in the ex vivo liver case. For the phantom setup, local estimation was not possible since samples were separated from each other and the mean S_0 value of the samples that were well characterized by conventional fitting was used for S_0-fitting. However, in each case were S_0-fitting needs to be applied, it has to be carefully considered if the S_0 condition is met.

Two methods, proposed in literature to increase the detectable R_2^* range, possess drawbacks. First, 3D UTE-based quantification methods are time-consuming and need non-selective excitation pulses, whereas 2D UTE methods need a very specific excitation scheme to reduce their sensitivity to eddy currents (67). Second, characterization of R_2^*

signal decay by sampling of the SE using either MGE (38, 57) or shifted SE (68) may be sensitive to diffusion due to the longer echo times typical for SE, leading to underestimation of the amount of Ho-MS that is present, as was shown recently (53). Finally, imaging times dramatically increase when applying shifted SE-based techniques due to the longer repetition times and application of multiple interleaved acquisitions, as was observed for qUTE as well (59).

In conclusion, a post-processing method providing a best estimate of high R_2^* values and hence of high local concentrations of Ho-MS is presented. The method uses information from well-defined neighboring voxels to determine the R_2^* value of a voxel that could not be characterized by conventional fitting. The method does not require dedicated MR pulse sequences as long as it is a MGE sampling scheme and was shown to be beneficial for quantification of high local concentrations of holmium-loaded microspheres.

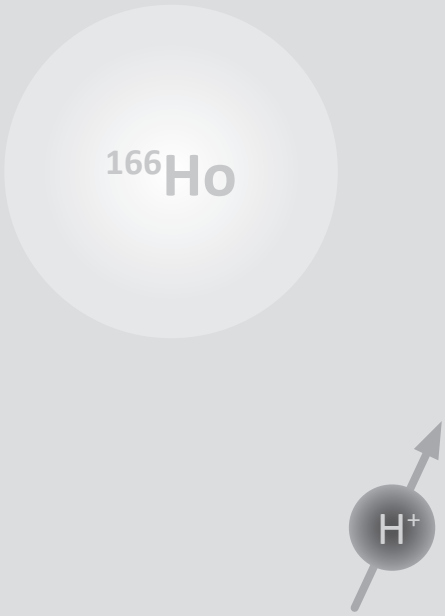
166Ho
H+

Chapter 4

Radiation-absorbed dose estimation

"The purpose of this study was to investigate whether MRI can be used to accurately assess the three-dimensional Ho-MS activity distribution to enable radiation-absorbed dose estimation for treatment planning optimization and follow-up of transcatheter liver RE."

Based on:

Seevinck PR, van de Maat GH, de Wit TC, et al. Magnetic resonance imaging-based radiation-absorbed dose estimation of (166)Ho microspheres in liver radioembolization. Int J Radiat Oncol Biol Phys 2012;83:e437-444

INTRODUCTION

During the past decade, over 30,000 patients suffering from unresectable primary or metastatic liver tumors were treated by hepatic arterial radioembolization (RE) with high-energy β-radiation-emitting microspheres (3, 69). Apart from the amount of radioactivity that is administered, the efficacy of this type of internal radiation therapy is postulated to depend on the intrahepatic dose distribution (3, 70, 71). By administering the microspheres intra-arterially, the predominance of the arterial supply to liver tumors is exploited, generally resulting in a high tumor-to-normal tissue ratio (72). However, the large variation in vascularity of tumor and liver observed between patients necessitates extensive treatment planning to assure a favorable dose distribution in each individual patient (73). The currently used radioactive microspheres for RE contain the β-emitting radionuclide ^{90}Y, which does not facilitate quantitative biodistribution assessment, despite developments involving Bremsstrahlung imaging (74) and more recently positron emission tomography (24). Therefore, in clinical practice, ^{99m}Tc macro aggregated albumin (MAA) is used as a surrogate, aiming to estimate the lung shunt fraction, to detect extrahepatic deposition, and to assess intrahepatic dose distributions using planar scintigraphy and single photon emission computed tomography (SPECT). The differences in size distribution (10-90 μm), number of particles, shape, density, and consequently hemodynamic properties of ^{99m}Tc-MAA particles, along with the sizeable amount (up to 10%) that is well below 30 μm are hypothesized to cause the discrepancies observed between the biodistribution of ^{99m}Tc-MAA particles and the ^{90}Y microspheres (74).

^{166}Ho-loaded poly(L-lactic acid) microspheres (Ho-MS) constitute an alternative RE device, the use of which has recently been the subject of a Phase I clinical trial (10). Ho-MS possess attractive radiation characteristics (E_β = 1.77 MeV [48.7%] and 1.85 MeV [50.5%]; E_γ = 81 keV [6.7%]; $t_{1/2}$ = 26.8h) for both therapy and quantitative SPECT imaging (28, 29, 73, 75). Interestingly, holmium is highly paramagnetic, which is independent of radioactivity, making neutron-activated and non-activated Ho-MS an ideal MR contrast agent (29, 37). These properties yield a single microparticle suitable for RE with the potential of in vivo quantitative biodistribution assessment. Additionally, MRI-guided catheterization and administration of Ho-MS has been shown to allow real-time in vivo monitoring of microsphere delivery to the tumor site (31, 37). More recently, the development of a fast quantitative MR imaging technique enabling accurate quantification of the distribution of Ho-MS at the level of a voxel was reported (53).

The purpose of this study was to investigate whether MRI can be used to accurately assess the three-dimensional Ho-MS activity distribution to enable radiation-absorbed dose estimation for treatment planning optimization and follow-up of transcatheter liver RE. To

this end, MRI experiments were conducted on an anthropomorphic gel phantom containing known amounts of Ho-MS and on an ex vivo human liver with tumors to which Ho-MS were administered post-excision. After transformation of MRI-based Ho-MS biodistributions into 3D ^{166}Ho activity distributions, radiation-absorbed dose distributions were estimated by convolution with a 3D ^{166}Ho dose point kernel. The results were validated by CT, SPECT, autoradiography, and dose calibrator measurements.

MATERIALS AND METHODS

Phantom preparation

Ten cone-hemisphere-shaped (~2 x 2.5 x 2.5 cm, ~7 ml) tumor-simulating agarose gel samples were prepared in a mould. The agarose gel (2%) was doped with 28 mg/ml $MnCl_2 \cdot 4H_2O$ to mimic the T_1 relaxation properties of liver tissue (gel density = 0.99 g/cm^3). Small amounts of radioactive Ho-MS were administered to the liquid gel in the mould. Ho-MS (17% by mass holmium; diameter = 30 ± 5 μm (mean ± SD) were prepared under good manufacturing practice as previously described (27). The specific activity (S_A) of Ho-MS, after activation by thermal neutron bombardment for 2 h (41, 73), was determined to be 5.83 MBq/mg using a dose calibrator (VDC-404, Veenstra Instrumenten B.V., Joure, the Netherlands), which was calibrated by the Dutch measurement institute (NMI, Delft, the Netherlands) according to the NEN-EN-ISO/IEC 17055:2005 criteria. Using the same dose calibrator, the activity in each "tumor" was determined. A total activity of 152 MBq in 26 mg of Ho-MS was distributed over eight "tumors" with the following amounts: 1.16, 1.16, 2.28, 2.86, 3.52, 3.95, 5.04, and 6.16 mg. As a control, two "tumors" without microspheres were made. The used amounts provided a realistic concentration range, in the knowledge that in clinical practice amounts of 60 mg (scout dose) to 600 mg (treatment dose) are infused into an average liver volume of 1.5 l (75), and in the expectation that tumor-to-normal tissue ratios vary between 2 and 8 (72, 75). All the "tumors" were subsequently placed in an ellipse-shaped Perspex phantom (short axis = 19 cm; long axis = 30 cm; height = 7 cm; volume ~3 L), that was filled with agarose gel.

Ex vivo liver preparation

To investigate the feasibility of MRI-based radiation absorbed dose estimation in a more realistic situation, an ex vivo tumor bearing human liver (2.4 kg) was prepared. A total amount of 606.5 mg Ho-MS (17% by mass) with an activity of 418 MBq (S_A = 0.689 MBq/mg) was prepared to be infused in the hepatic artery of the liver after excision. Before

infusion, the liver was submersed in purified water doped with 28 mg/ml $MnCl_2 \cdot 4H_2O$ to mimic the T_1 relaxation properties of liver tissue. The total administered amount of radioactivity was determined retrospectively by subtracting the activity left in the vial, syringe, tubes, and cloths, as determined using the dose calibrator.

MR imaging

The MR imaging experiments were performed on a clinical 3T MR system (Achieva, Philips Healthcare, the Netherlands). A quantitative MR imaging technique was applied, based on multiple gradient echo sampling of the free induction decay (53). For the phantom experiments, imaging parameters were as follows: field of view = 384 x 312 mm^2; flip angle = 45°; TR/TE1/ΔTE = 400/1.11/0.68 ms with 16 echoes; isotropic voxel size 3 mm^3; 22 slices; slice gap = 0 mm, and total acquisition time = 22.8 s. For the ex vivo liver experiment, similar parameter settings were used, however, with in-phase/out-of-phase gradient echo times (TE1/ΔTE = 1.15/1.15 ms) to prevent the influence of water-fat resonance frequency shifts, and with a slice thickness of 7 mm to increase coverage, resulting in a voxel size of 3 x 3 x 7 mm^3.

CT imaging

The x-ray CT experiments were performed on a 64-slice clinical CT scanner (Brilliance, Philips Healthcare, the Netherlands) for qualitative comparison of the estimated MRI-based biodistribution and absorbed dose maps of the ex vivo liver (29). The imaging parameters were as follows: field of view = 257 x 257 mm^2; matrix = 512 x 512; pixel spacing = 0.50 mm; collimation = 64 x 0.625 mm; pitch = 0.5; slice thickness = 1 mm; slice spacing = 0.5 mm; x-ray tube voltage and current 140 kVp and 337 mA, respectively. A soft tissue reconstruction filter was used.

SPECT imaging

Before SPECT, the liver was embedded in a carboxylmethyl cellulose solution (2.5%) containing four $^{166}HoCl_3$ markers as references, and was kept at -20°C for 24 hours. For both phantom and ex vivo liver, SPECT was acquired using a dual-headed gamma camera equipped with medium-energy general purpose collimators (Vertex MCD, Philips Healthcare, the Netherlands). Scanning line sources containing 5.5 GBq ^{153}Gd were used for attenuation correction (energy window: 100 keV ± 10%). The ^{166}Ho photo peak window was set to 81 keV ± 7.5%. A window centered at 118 keV ± 6% was used to obtain an estimate for the down-scatter in both the emission and transmission windows. The 360° SPECT study consisted of 120 projections of 30 s/angle. The imaging parameters were as follows: acquired matrix size = 128 x 128; reconstructed matrix size = 128 x 128 x 128; isotropic voxel size = 4.72 mm^3. A quantitative iterative reconstruction protocol as previously de-

scribed by De Wit et al (28) was applied. To obtain optimal image resolution, 40 iterations were used. No postreconstruction filter was applied.

Autoradiography

The frozen carboxylmethyl cellulose-embedded liver was cut into 6-mm-thick slices. The slices were placed on a storage phosphor screen (8 min exposure time/slice) and scanned using a Storm imaging system (GE Healthcare Life Sciences, Diegem, Belgium; 200 µm pixel size).

Data analysis

MR images

The effective transverse relaxation rate (R_2^*) was determined voxelwise using a least-squares fitting algorithm, assuming monoexponential signal decay. The Ho-MS concentration distributions ([Ho-MS]) were determined based on the R_2^* maps and the linear r_2^* relaxivity of Ho-MS, which represents the change in R_2^* (ΔR_2^*) as a function of the Ho-MS concentration ([Ho-MS] = $\Delta R_2^*/r_2^*$) as previously described (53) and summarized in Figure 1. For Ho-MS (17% by mass) at 3T, the relaxivity r_2^* was determined to be 180 $s^{-1}.mg^{-1}.ml$ (53). The concentration maps of the ex vivo liver were upsampled to a slice thickness of 3 mm using a linear interpolation scheme, leaving the total amount of Ho-MS unaffected. This resulted in 3-mm cubic voxel sizes for all data. Multiplication of the concentration maps by the voxel volume provided the total amount of Ho-MS present in each voxel. Then, multiplication by the specific activity of the administered microspheres at the moment of infusion provided maps of the activity per voxel.

SPECT images

The SPECT reconstructions provided an absolute quantitative 3D activity distribution (in MBq) per voxel after multiplication with a previously determined calibration factor specific for ^{166}Ho (28). The SPECT reconstructions were upsampled using a linear interpolation scheme to an isotropic voxelsize of 3 mm^3. To obtain the amount of Ho-MS in milligrams per voxel, the 3D activity distribution was divided by the specific activity.

Radiation-absorbed dose calculations

A ^{166}Ho dose point kernel (DPK) was calculated using the Monte Carlo N-Particle transport code (MCNP5; vs. 1.20; LANL, Los Alamos, NM) according to the method described in Medical Internal Radiation Dose (MIRD) Pamphlet 17 (47), assuming a tissue density for liver tissue of 1.06 g/cm^3, according to International Commission on Radiation Units and Measurements Report 44 (48). Default particle physics settings for MCNP were used

(energy cutoff 1 keV; photoelectric effect and coherent photon scattering turned on; Bremsstrahlung and x-ray production by electrons). The particle transport of the low-energy conversion and Auger electrons was not calculated because the range of these particles in liver tissue is well below the 3-mm voxel size; the total electron energy (27keV/decay) was considered to be locally deposited in each source voxel. The 3D point-symmetric DPK was generated on a 29 x 29 x 29 matrix, with the source located in the center, providing the absorbed energy in 3-mm cubic voxels per decay for the emission spectrum of ^{166}Ho as a function of the source-to-target voxel center-to-center distance. Radiation-absorbed dose distributions were estimated by convolving the MRI- and SPECT-based activity distributions with the ^{166}Ho dose kernel, after converting absorbed energies to dose per activity by taking into account the ^{166}Ho decay constant and voxel mass and assuming complete trapping of activity.

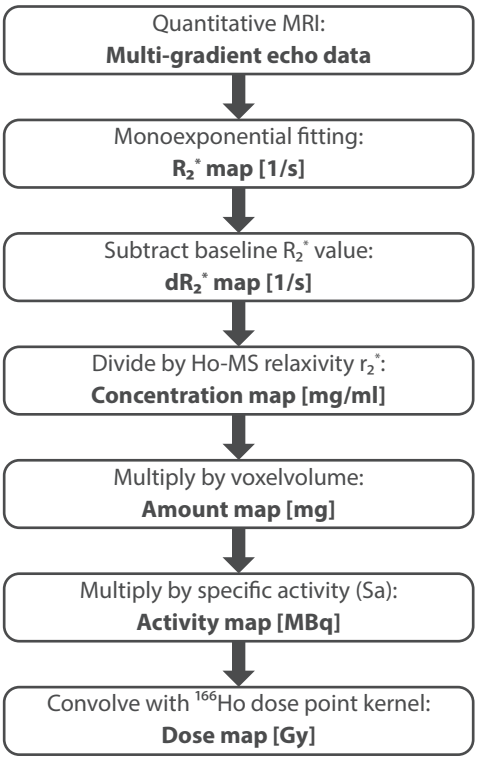

Figure 1 Flowchart indicating the sequence of steps taken to derive three-dimensional voxel-based ^{166}Ho radiation-absorbed dose distributions from MRI data.

Volume of interest analysis

The total amount of Ho-MS in the gel phantom was determined for each "tumor" separately by a volume of interest (VOI) analysis on MRI-based maps and SPECT-based maps. Cylinder-shaped VOIs were manually drawn around each "tumor", taking into account a 5-mm margin to ensure that the entire "tumor" was included. Summation of the included amount of Ho-MS in milligrams per voxel provided the total amount of Ho-MS in milligrams for each "tumor" for both imaging modalities, which also reflected the total activity per "tumor" when dividing by S_A.

The ex vivo liver was manually segmented utilizing T_2^*-weighted MR images to enable an MRI data VOI analysis of the whole liver. For analysis of the SPECT data, a VOI was defined by segmenting the liver on three orthogonal projections of the 3D activity maps. The estimated total amount and activity of Ho-MS were compared with the values obtained with the dose calibrator. Projections images were made for qualitative comparison. For quantitative analysis using a cumulative dose-volume histogram, the administered activity was extrapolated to that for a uniform average liver dose of 40 Gy. For a 2.4 kg liver, 6.0 GBq of ^{166}Ho activity is required to deliver 40 Gy (10), which was simulated by multiplying the net activity administered to the liver (368 MBq) by a factor of 16.3. Finally, a single slice analysis was performed by comparing MRI-based absorbed dose maps with CT, and by comparing SPECT-based absorbed dose maps with autoradiography.

RESULTS

In vitro experiments

The absorbed energy in liver tissue per decay for the emission spectrum of ^{166}Ho as a function of the distance between source and the center of a 3-mm cubic target voxel is shown in Figure 2. This energy deposition function was generated by MCNP and from MIRD pamphlet 17 and subsequently used to construct the ^{166}Ho DPK.

MRI-based and SPECT-based radiation-absorbed dose maps of the phantom setup, generated utilizing the ^{166}Ho DPK, showed good agreement both visually and quantitatively (Figure 3). The MRI-based dose maps clearly reflected the actual cone-hemisphere shape of the tumor-simulating gel samples containing Ho-MS; however, the SPECT-based dose maps depicted smoothed and sphere-shaped dose distributions. These differences are related to the inherently low resolution of SPECT and the subsequent upsampling (4.72 mm to 3 mm) necessary to match the cubic voxelsize of the DPK, leading to increased partial volume effects and spatial blurring at the edges of the "tumor".

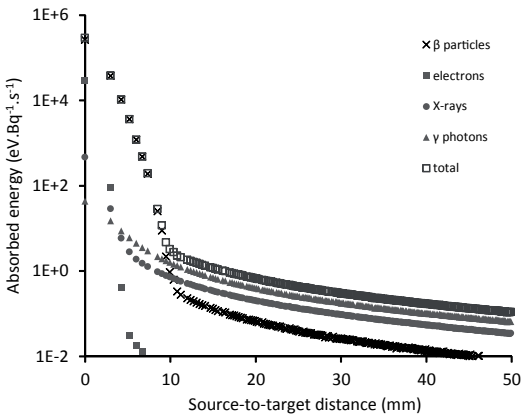

Figure 2 The absorbed energy in 3-mm cubic voxels in liver tissue per decay for the emission spectrum of ^{166}Ho as a function of the distance between source and target voxel centers.

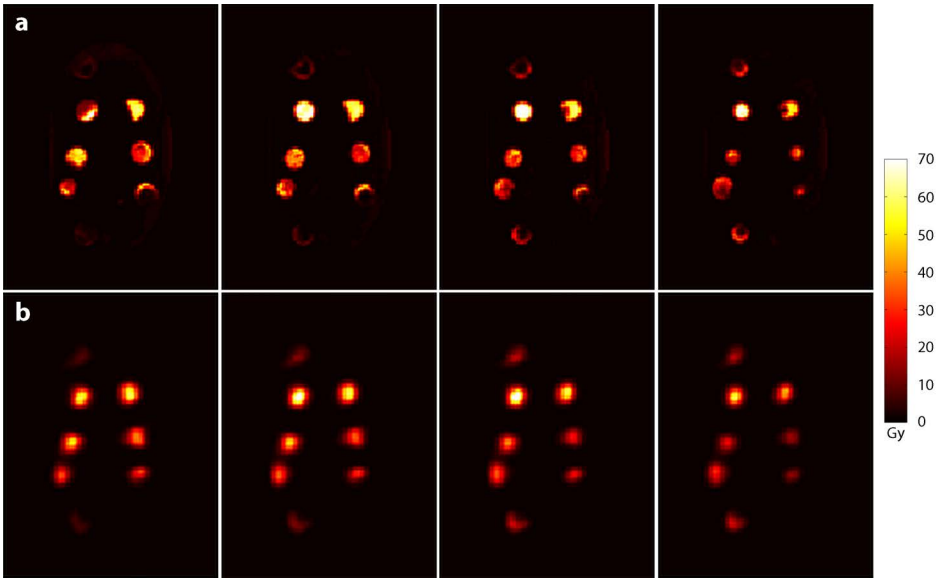

Figure 3 Estimated magnetic resonance imaging (MRI)-based (a) and single photon emission computed tomography (SPECT)-based (b) radiation-absorbed dose distributions, depicting the tumor-simulating gel samples in four consecutive slices (isotropic voxel size = 3 mm) of the agarose gel phantom.

In the center of the "tumors", where partial volume effects have less influence, both modalities presented similar absorbed dose values, with maximum values of 65 Gy. In some areas outside the "tumors", at locations where no activity was present based on prior knowledge, nonzero values were found on the MRI-based absorbed dose maps. These offsets in absorbed dose directly related to macroscopic magnetic field inhomogeneities

induced by sharp edges in the Perspex phantom, which locally increased the R_2^* value and thereby falsely indicated the presence of Ho-MS.

The VOI analysis of the tumor-simulating gel samples showed good agreement between the total amounts per "tumor" of Ho-MS as determined by MRI and by both SPECT and the dose calibrator (Figure 4). Linear regression analysis, relating SPECT- and MRI-based total amount of Ho-MS per "tumor" to the values obtained with the dose calibrator, revealed a linear relation of 1.05 (R^2 = 0.99) for MRI data and 1.00 (R^2 = 0.99) for SPECT data. The relation between MRI data and SPECT was found to be 1.05 (R^2 = 0.99).

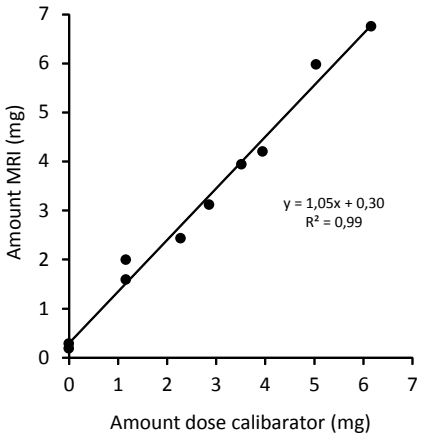

a)

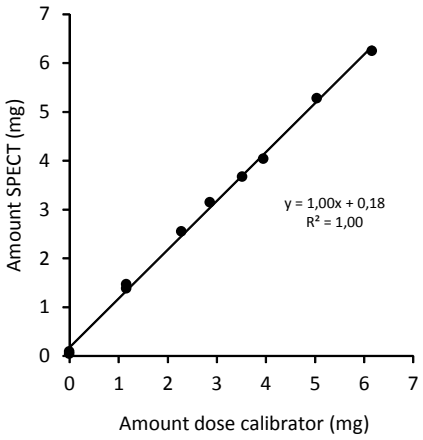

b)

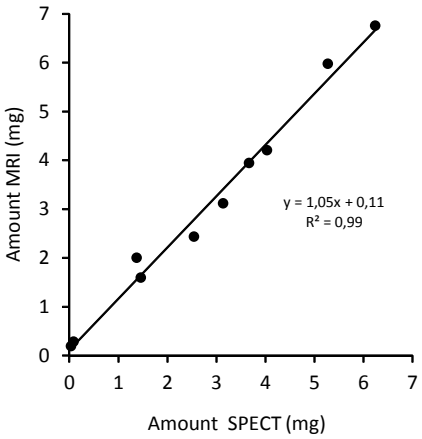

c)

Figure 4 Total estimated amounts of ^{166}Ho-MS in the "tumors" as determined with MRI (a) and with SPECT (b), plotted against the known amounts of ^{166}Ho-MS as determined with a dose calibrator. The correlation between MRI and SPECT is also demonstrated (c).

Ex vivo liver

Analysis of the MRI data provided a total amount of 521 mg of Ho-MS in the ex vivo liver, containing a total activity of 359 MBq. This agrees well (2.4%) with the values found by the dose calibrator (534 mg containing 368 MBq). SPECT overestimated the dose calibrator measurements by 7.9% (576 mg containing 397 MBq). Cumulative dose volume histograms obtained from MRI and SPECT-based absorbed dose estimations in the liver showed a high degree of resemblance (Figure 5).

This resemblance was visually supported by projection images of the SPECT- and MRI-based dose maps, which depicted similar dose distributions macroscopically (Figure 6a, b). The CT projection (Figure 6c) showed excellent visual agreement with the biodistribution of Ho-MS as depicted in the MRI projection, both having been obtained from the same experimental setup which prevented translation, rotation, and deformation.

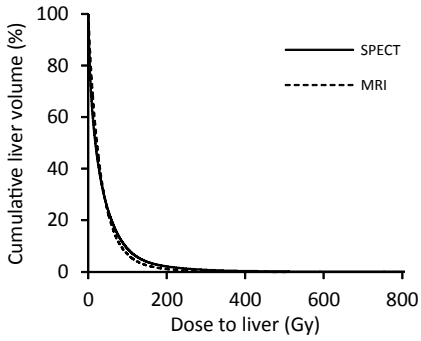

Figure 5 MRI-based and SPECT based cumulative dose-volume histograms measured in the whole liver. To simulate an average dose typical for clinical use, the net activity administered to the liver was multiplied by a factor of 16.3.

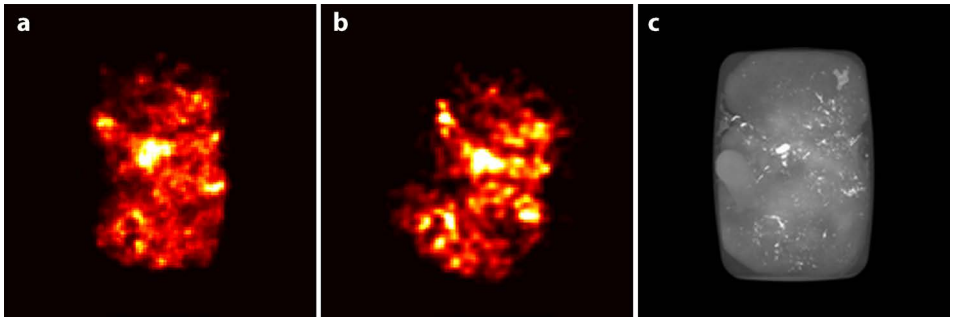

Figure 6 MRI-based and SPECT-based dose distributions in the ex vivo liver. Projection images of the three-dimensional dose distribution estimated from MRI (a) and SPECT data (b) show excellent agreement. The CT projection (c) shows excellent agreement with the biodistribution of Ho-MS depicted in the MRI projection.

Figure 7a-c shows a T_2^*-weighted MR image of the liver, the corresponding MRI-based absorbed dose distribution, and a CT image of the same slice, in which Ho-MS is depicted hyperintense. Excellent visual agreement was observed between the hypo-intensities in the T_2^*-weighted image, the high values in the absorbed dose map, and the hyper-intensities in the CT image. Although MRI- and SPECT-based dose maps (Figure 7b, 7e) showed similar absorbed dose distributions, clear differences could be observed as well. Apart from differences related to acquisition voxel size, differences in orientation were observed which can be attributed to the fact that prior to SPECT, the liver was transferred into a setup with radioactive markers used as landmarks to enable comparison of SPECT with autoradiography imaging. These autoradiographs showed a high degree of visual resemblance with the SPECT-based absorbed dose distributions (Figure 7f). However the SPECT reconstructions and dose maps showed lower resolution and smoothed distributions as compared to the autoradiographs.

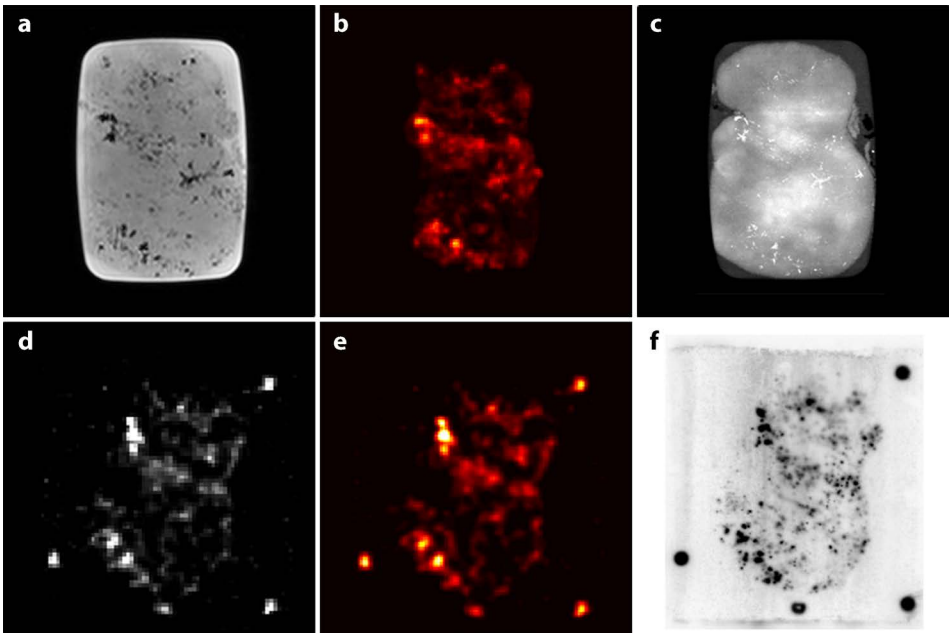

Figure 7 Single slice qualitative comparison of the biodistribution, activity distribution, and estimated radiation-absorbed dose distribution obtained with magnetic resonance imaging (MRI), computed tomography (CT), single photon emission CT (SPECT), and autoradiography. The T_2^* weighted image (a) and accompanying MRI-based dose map (b) show distributions similar to the CT image (c). The single slice MRI and SPECT-based dose maps (b and e) macroscopically and quantitatively agree well, taking into account object rotation. The SPECT image (d) (4.7 mm slice thickness) and the accompanying SPECT dose map (3 mm slice thickness) show a high degree of visual resemblance to the autoradiograph (f) (6 mm slice thickness). Four markers are shown as a reference.

DISCUSSION

This study demonstrates that quantitative MRI enables accurate estimation of the Ho-MS activity distribution in vitro and in ex vivo human tumor-bearing liver in an acquisition duration equal to a single breath hold. Furthermore, it was shown that by convolution of the 3D MRI-based activity distribution with a ^{166}Ho dose point kernel, it is possible to estimate the radiation-absorbed dose distribution. These results, in combination with the fact that MRI provides high resolution and excellent soft tissue contrast, has relatively short acquisition times, and allows real-time monitoring during microsphere delivery to the tumor site (31, 37), suggest that MRI is an attractive modality to perform treatment planning and follow-up of transcatheter radioembolization of hepatic malignancies with Ho-MS. Interestingly, the sensitivity of MRI for Ho-MS is independent of radioactivity, enabling intra-procedural biodistribution assessment and dose prediction using "cold" Ho-MS and the acquisition of follow-up scans after treatment long after ^{166}Ho has decayed.

The accuracy of MRI-based absorbed dose estimations of Ho-MS is directly related to the accuracy of the Ho-MS biodistribution assessment. In this regard, two limitations should be addressed. First, the MRI-based approach provides a single concentration value for each volume element, assuming an average activity in the entire voxel. This will not be the case in clinical practice, given that RE is an intravascular procedure that provides a highly inhomogeneous particle distribution at the level of the microvasculature. When a dose point kernel is applied for absorbed dose estimation in such a case, a homogeneous tissue composition and uniform radionuclide distribution within voxels is implicitly but falsely assumed, which may be expected to affect the accuracy of the DPK convolution method. These well-known characteristics of voxel dosimetry have already been addressed by Bolch et al. (47). Second, the accuracy of the MRI-based biodistribution assessment is limited by local variations of baseline R_2^* values in the liver, inasmuch as these variations complicate accurate determination of the increase of the R_2^* value (ΔR_2^*) attributed to the presence of Ho-MS. It is important to be aware of this limitation; however, it should also be realized that its maximum influence can easily be predicted and therefore taken into account in the treatment optimization (e.g., an erroneous increase of R_2^* by 10 s^{-1} translates into a local concentration increase of 0.05 mg/ml (= $\Delta R_2^*/r_2^*$)).

When higher accuracy and consistency are needed, for example for pretreatment intrahepatic dose prediction, both the baseline R_2^* map and the post-administration R_2^* map could be acquired in the same scan session. This would ensure intrinsic image registration and enable voxel wise subtraction of spatially varying baseline R_2^* values, leading to potentially very accurate ΔR_2^* maps and activity maps since tissue variability can be overcome. In practice, this will require MRI-guided catheterization and administration of

Ho-MS. The feasibility of such an MRI-guided radioembolization procedure has previously been demonstrated in pigs (31); however, the current absence of MR-compatible and visible guidewires and catheters approved for clinical use is an important limiting factor. Recent developments in this field are promising and may be expected to enable fully MRI-guided catheter directed RE (76). Such an MRI-guided approach will be particularly useful for patient-specific localized treatment, as provided in radiation segmentectomy (in which RE is selectively performed in only one or two predefined hepatic segments) which may be expected to increase safety and efficacy of radioembolization (70).

In conclusion, quantitative MRI was demonstrated to provide accurate 3D Ho-MS activity distributions at the voxel level, facilitating localized intrahepatic radiation-absorbed dose estimation by convolution with a ^{166}Ho dose point kernel to enable radioembolization treatment planning optimization and evaluation.

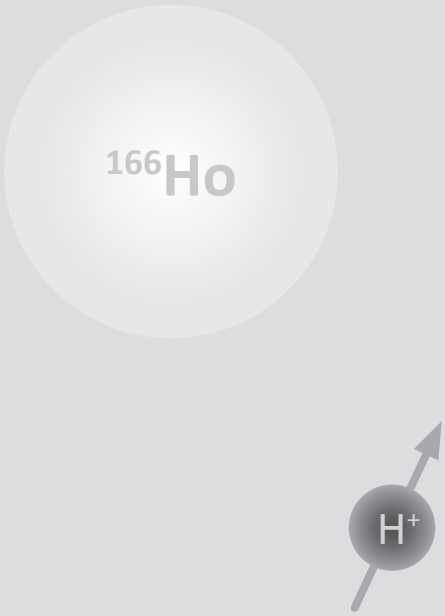
166Ho
H+

Chapter 5

SOFIDSE: Quantification in a single acquisition

"In this work we propose a method, S_0 estimation of the free induction decay combined with a single spin echo measurement, further abbreviated as SOFIDSE, that can be used to simultaneously measure R_2^*, R_2 and R_2' in diffusive systems containing paramagnetic Ho-MS within a relatively short acquisition time."

INTRODUCTION

MRI-based biodistribution measurement of paramagnetic holmium-166 Poly(L-lactic acid) microspheres (Ho-MS) (27, 36-38) is, like detection of other clinically applicable (super)-paramagnetic particles (35, 77), primarily based on R_2^* dephasing effects the microspheres induce. In general, the R_2^* relaxation rate increases for increasing particle concentration, enabling changes in R_2^* to be related to the local particle amount. Convenient methods to measure R_2^* relaxation rates sample either the free induction decay (FID) or the spin echo (SE) by utilizing a multi-gradient-echo (MGE) sequence.

The preferred method to quantify the local amount of Ho-MS is sampling the FID as this has been shown to provide a more accurate quantitative measure as compared with sampling the SE due to non-monoexponential signal behavior as a consequence of diffusion effects (53). R_2^* values are estimated by a monoexponential fit to the FID data and linearly related to the local microsphere concentration by their relaxivity r_2^*. The major drawback of this approach is that both the Ho-MS induced signal decay and the intrinsic R_2 signal decay of the tissue in which the microspheres reside contribute to the observed R_2^* values. The presence of this tissue R_2 component requires acquisition of a baseline R_2^* value prior to administration of the microspheres to subtract from the post-administration value in order to obtain the holmium induced ΔR_2^*. Using such a strategy makes the quantification method sensitive to two types of errors. First, subtraction of post and pretreatment R_2^* values has to be performed voxel wise to prevent influence of spatial variations in R_2^* due to tissue specific R_2 values and global field variations and thus necessitates co-registration of the post and pretreatment R_2^* images. Such a co-registration puts requirements on patient position, and demands changes in size and shape of the tissue between the two imaging sessions to be minimal. Second, using pretreatment R_2^* values, dominated by the tissue R_2 value in the absence of field inhomogeneities, as a baseline for ΔR_2^* measurements makes the method sensitive to changes in tissue R_2 values occurring in the interval between the pre and post image acquisition. Such R_2 changes are expected to occur because of development of necrotic, edematous or hemorrhagic changes as a consequence of the therapy (49).

Considering the influence of tissue R_2 values, inclusion of R_2 measurements may be expected to improve quantification of Ho-MS. The classical approach to measure R_2 values is by collecting a series of Carr-Purcell-Meiboom-Gill (CPMG) echoes (78, 79) and determine the R_2 value by a monoexponential fit to the measured spin echo signal intensities. However, CPMG echo signal behavior of diffusive systems containing paramagnetic objects deviates from monoexponential behavior due to diffusion effects (80, 81), which have been demonstrated to also occur in Ho-MS containing systems (82), complicating quanti-

fication of R_2. Acquisition of single Hahn echoes (83) with shifted echo times would suffer less from this effect but increases acquisition time, limiting clinical utility. Another disadvantage of these methods is that the R_2 values are acquired separately from acquired R_2^* values, necessitating image co-registration. For these reasons, other methods have been proposed, dedicated to simultaneously measure R_2^*, R_2' and R_2; for example, gradient-echo sampling of FID and echo (GESFIDE) (84) which samples the downslope of the FID and the upslope of the single spin echo, or gradient echo sampling of the spin echo (GESSE) (85), which samples the upslope and the downslope of the spin echo. However these methods also suffer from non-monoexponential signal behavior of the spin echo envelope (53).

In this work we propose a method, S_0 estimation of the free induction decay combined with a single spin echo measurement, further abbreviated as SOFIDSE, that can be used to simultaneously measure R_2^*, R_2 and R_2' in diffusive systems containing paramagnetic Ho-MS within a relatively short acquisition time. The method combines a multi gradient echo (MGE) read-out of the FID with a single spin echo (SE) read-out. By monoexponentially fitting the FID data, R_2^* and the signal amplitude at time point 0, S_0, are estimated. Subsequently, the estimated S_0 together with the signal amplitude of the spin echo is used to estimate R_2 using a monoexponential fit. By subtracting R_2 from R_2^*, the microsphere induced R_2' is obtained. We will show that SOFIDSE can be used to accurately estimate R_2 values and that Ho-MS induced R_2' values obtained by SOFIDSE are independent of the R_2 value of the tissue in which the microspheres reside and thus provides a valuable tool for Ho-MS quantification in tissue that is subjected to R_2 changes as a consequence of therapy.

THEORY

In general, in the absence of proton diffusion, the MR signal decay can be described in terms of a monoexponential function, where the envelope of the FID is characterized by

$$S(t) = S(0) \cdot e^{-R_2^* \cdot t} \quad \text{with} \quad R_2^* = R_2 + R_2' \qquad [1]$$

and the signal amplitude of the spin echo by

$$S(t) = S(0) \cdot e^{-R_2 \cdot t} \qquad [2]$$

where R_2 represents the tissue dependent thermodynamic decay component and R_2' the (reversible) component induced by system or object related external field inhomogeneities (86).

In case there is diffusion of protons, the MR signal behavior in the presence of field inhomogeneities changes, and Equations [1] and [2] may be no longer valid. To what extent the signal behavior changes primarily depends on the water diffusion coefficient, the strength of the main magnetic field, and the size, volume fraction and susceptibility of the field perturbing objects. In the limiting case where the average distance water molecules diffuse is relatively small compared to the size of the perturbing objects, the system is in the so-called static dephasing regime (SDR), R_2' dephasing effects can be refocused by a 180° pulse and Equations [1] and [2] hold (87). In the other limiting case, where water molecules can at least diffuse an inter-object spacing in a time period comparable to the reciprocal of the mean change in proton Larmor frequency due to the local field, the motion of the water averages out the influence of the static field gradients, which is known as motional narrowing (88). This motional narrowing results in an effectively lower, mainly irreversible, R_2^*. In the intermediate regime between these two limiting cases, signal behavior is complex but has been investigated by means of Monte Carlo based simulations and experiments (89). Moreover, analytical models have been developed that can be applied if the system under investigation satisfies certain criteria, for example the model of Kiselev and Posse that describes the MR signal in microvascular networks (90, 91) and the strong- and weak field behavior models of Jensen and Chandra (92, 93). In particular Monte Carlo results demonstrate that in general, starting from negligible diffusion, R_2^* starts at a maximum plateau and decreases towards a minimum due to motional narrowing whereas R_2, given by the spin echo signal, starts at a minimum in SDR, reaches a peak value in the intermediate regime and decreases again toward the motional narrowing regime. Over the entire range R_2^* is larger than R_2 but the ratio between the two depends on the system (89).

For aqueous systems containing paramagnetic Ho-MS it has been shown that not only the FID decays faster as a function of microsphere concentration but that also the spin echo amplitude is affected as a consequence of diffusion effects (38). Although the FID complies with the criteria of SDR, leading to signal behavior that can be completely described in terms of static dephasing, when involving a spin echo readout for quantification of Ho-MS the total signal behavior cannot completely be described in terms of static dephasing anymore (53). Since quantification of Ho-MS by utilizing SOFIDSE is based on a subtraction of the diffusion independent FID relaxation rate and the diffusion dependent spin echo decay rate we have to define a relaxivity parameter that relates SOFIDSE signal decay to the concentration Ho-MS. This parameter, which we call $r_{2\,SOFIDSE}'$, is derived as follows.

We define the FID relaxation rate of a Ho-MS containing system as:

$$R_2^* = R_{2,tissue} + R_{2,holm}^{'} \quad [3]$$

following the definition of SDR (87) where $R_{2\,holm}^{'}$ depends on the volume fraction and susceptibility of the microspheres, and on the main magnetic field B_0. For the spin echo decay, measured at a single spin echo time TE, we adopt the monoexponential approach from Equation [2] but include a relaxation rate term, $R_{2,holm\,irrev}^{'}$, that represents the microsphere induced irreversible loss of signal due to proton diffusion

$$R_2 = R_{2,tissue} + R_{2,holm\ irrev}^{'} \quad [4]$$

Although such a monoexponential approach does not accord with the nonlinear signal description that has been analytically derived for the spin echo decay of heterogeneous systems subjected to diffusion (92), in this work we will experimentally show that for a clinically interesting range of Ho-MS concentrations this approach suffices. Based on the two relaxation rates of Equations [3] and [4], the SOFIDSE relaxation rate $R_{2\,SOFIDSE}^{'}$ is given by subtraction

$$\begin{aligned} R_{2,SOFIDSE}^{'} &= (R_{2,tissue} + R_{2,holm}^{'}) - (R_{2,tissue} + R_{2,holm\ irrev}^{'}) \\ R_{2,SOFIDSE}^{'} &= (R_{2,holm}^{'} - R_{2,holm\ irrev}^{'}) \end{aligned} \quad [5]$$

Resulting in a relaxivity of

$$r_{2,SOFIDSE}^{'} = \frac{\Delta R_{2,SOFIDSE}^{'}}{\Delta[HoMS]} \quad [6]$$

From Equation [5] it is observed that the here defined SOFIDSE relaxation rate and thus relaxivity include only Ho-MS induced reversible dephasing effects and do not depend on tissue characteristics.

MATERIALS AND METHODS

SOFIDSE was applied on an agarose phantom containing a range of Ho-MS concentrations and results were compared with results obtained from a combination of FID and shifted spin echo measurements to validate the method. Furthermore, to demonstrate the independence of SOFIDSE quantification on tissue R_2, measurements were carried out on a phantom containing agarose gels with varying agarose concentrations and thus different R_2 values. Finally, similar experiments were carried out on a healthy volunteer to investigate the in vivo applicability of the method.

Preparation

Phantom

Three agarose gel series were prepared in 25 ml plastic tubes (length ~ 65 mm, inner diameter = 22 mm).

The first series of 6 gel samples was prepared with 2% agarose (weight/weight) in $MnCl_2.4H_2O$ doped water (30 mg per liter distilled water). During preparation of the gel, non-radioactive Ho-MS, prepared as described by Nijsen et al. (27), were added in concentrations of 0.96, 2.24, 3.03, 4.16 and 4.99 mg/ml. One sample was left blank (0mg/ml). The microspheres had a density of 1.4 g/ml and a holmium content of 18.9% (weight/weight) whereas the microsphere diameter ranged between 20 and 50 µm with a mean diameter of 30 µm.

The second series consisted of 6 gel samples with different agarose content: 1.00, 1.26, 1.51, 1.73, 2.01 and 2.26 % agarose (weight/weight) in $MnCl_2.4H_2O$ doped water (27 mg per liter distilled water). No Ho-MS were added.

The third series of 6 gel samples was identical to the second series with respect to the agarose content but now Ho-MS were added with an intended concentration of 1 mg/ml. The actual Ho-MS concentrations were 1.01, 1.08, 1.08, 1.04, 1.08 and 0.99 mg/ml.

Healthy volunteer

A 27-year-old male healthy volunteer was included in this study who provided written informed consent. The study setup was in accordance with the guidelines of the institutional review board.

Data acquisition

MRI data was acquired on a 1.5 T whole body system (Achieva, Philips Healthcare, Best, the Netherlands), using an 8-channel head receive coil for the phantom experiments and a 16-channel torso receive coil for imaging of the healthy volunteer. SOFIDSE data was acquired, sampling both the FID and the spin echo envelope by means of gradient echo images, using a custom-built research patch (Philips Research Laboratories, Hamburg, Germany), as described in Figure 2 of reference (94), but using only one spin echo.

Phantom

For the first gel series, containing various concentrations of Ho-MS, SOFIDSE data was acquired using a 2D sequence, sampling the FID by 11 gradient echoes (TE_1 = 3.1 ms/ΔTE = 0.8ms) followed by sampling the spin echo envelope by 11 gradient echoes with ΔTE = 0.8ms, centered around the spin echo peak. Data was acquired using 5 different spin echo times: 20, 30, 40, 50 and 60 ms to provide shifted spin echo (SSE) data. Other parameters included: repetition time (TR) = 2000 ms; slice thickness = 10 mm; field of view (FOV) = 128 x 128 mm^2; matrix = 64^2; and read-out bandwidth = 1783 Hz/pixel.

For the second gel series, containing various concentrations of agarose but no Ho-MS, SSE data was acquired using a 2D single spin echo sequence that was repeated for 5 different echo times: 10, 20, 30 40 and 50 ms. TR, slice thickness, FOV and matrix were identical to the parameters used for SOFIDSE of the first gel series, except from a slightly different read-out bandwidth (2047 Hz/pixel). In addition, diffusion weighted imaging was performed for ADC measurements in order to verify that varying the agarose concentrations only influenced the R_2 relaxation time of the samples and not the diffusion coefficient. Five diffusion weighted images were acquired with b-values of 0, 100, 200, 300 and 400 s/mm^2 and an effective echo time of 48 ms. Other imaging parameters were identical to those of the previous experiment.

For the last gel series, containing varying concentrations of agarose and on average 1 mg/ml Ho-MS, a single SOFIDSE acquisition was performed. FID and spin echo were both sampled by 11 gradient echoes with an echo spacing of 0.8 ms. The echo time of the first gradient echo of the FID was 3.1 ms whereas the spin echo was centered around 30 ms.

Healthy volunteer

Multi slice SOFIDSE data was acquired using 13 gradient echoes for sampling the FID (TE_1 = 2.3ms, ΔTE = 0.8) and 13 gradient echoes for sampling the spin echo envelope (spin echo time = 30 ms, ΔTE = 0.8). Imaging parameters included: FOV = 384 x 344 mm^2; acquisition matrix = 192 x 151; reconstruction matrix = 192 x 192; slice thickness = 6 mm; nr of slices = 45; TR = 360 ms; flip angle = 90°; read-out bandwidth = 1783 Hz/pixel. Sensitivity encoding (SENSE) with a factor of 2.7 was used for acceleration resulting in a scan time of

5 x 20 s during breath hold.
Dual echo (DE) spin echo data was acquired using a multi slice dual echo sequence with TE_1 = 20 ms and TE_2 = 50 ms. FOV, matrix, and flip angle were identical to the SOFIDSE acquisition. A repetition time of 300 ms was used and the read-out bandwidth was 1733 Hz/pixel. Here also SENSE was used (factor 2.7) and two signal averages were acquired resulting in a scan time of 9 x 20 s during breath hold.

Data analysis

Phantom
From all the acquired images, signal intensities for each gel sample were measured utilizing regions of interest (ROI, ±48 pixels).
Data of the first gel series, containing a range of Ho-MS concentrations, was processed as follows. First, a monoexponential fit ($S(TE) = S_0 \cdot \exp[-R_2^* \cdot TE]$) was applied to the gradient echo signal intensities S(TE) (mean ROI values) of the FID part of the SOFIDSE data from which R_2^* and S_0 values were obtained for each concentration. A threshold was applied excluding signal intensities from the fitting procedure with a signal to noise ratio (SNR) lower than 3, where the noise was determined by the standard deviation of the ROI signal intensity of the 0 mg/ml sample. Subsequently, the estimated S_0 values were combined with the signal intensities of the central spin echo sample of the SOFIDSE data for TE = 30 ms and R_2 (SOFIDSE) values were determined for each Ho-MS concentration by R_2 (SOFIDSE) = $\ln((S_0)/S(TE))/TE$. Next, the spin echo intensities, for the range of used spin echo times (20, 30, 40, 50, 60 ms) were monoexponentially fitted by $S(TE) = S_0 \cdot \exp[-R_2(SSE) \cdot TE]$ to obtain S_0 and R_2 (SSE) values for each Ho-MS concentration from the SSE data. Finally, $R'_{2\,SOFIDSE}$ values were calculated for each concentration Ho-MS using $R'_{2\,SOFIDSE} = R_2^* - R_2$ with R_2 either R_2 (SOFIDSE) values or R_2 (SSE) values. Correlations coefficients for both R_2 values and both $R'_{2\,SOFIDSE}$ values were calculated and the Ho-MS relaxivities r_2^*, r_2 and $r'_{2\,SOFIDSE}$ were determined from a linear fit of relaxation rates vs. microspheres concentration.
For the second gel series, containing various concentrations of agarose but no Ho-MS, signal intensities of the SSE data were monoexponentially fitted to obtain the R_2 value for each agarose concentration. Signal intensities of the diffusion weighted images were also monoexponentially fitted using $S(b) = S(0) \cdot \exp[-ADC \cdot b]$ from which ADC values were obtained for each agarose concentration.
For the third gel series, containing agarose concentrations identical to the second series but in addition a Ho-MS concentration of 1 mg/ml, $R'_{2\,SOFIDSE}$ values were determined using SOFIDSE data following the same procedure as was used for the first gel series.

Healthy volunteer

From the gradient echo images of the FID part of the SOFIDSE data, S_0 values and R_2^* values were estimated for each voxel by using a monoexponential fit. The resulting S_0 images were subsequently used in combination with the central spin echo image of the SOFIDSE data to determine voxelwise R_2 (SOFIDSE) values. $R'_{2\ SOIFDSE}$ values were obtained by subtracting R_2^* and R_2 values. Voxel wise R_2 values were also obtained from a monoexponential fit to the spin echo signal intensities of the dual echo data (R_2 (DE)). The liver was manually segmented using the tissue contrast of the spin echo image of the SOFIDSE data. The distribution of estimated R_2 values found in the liver was measured for both SOFIDSE and DE, and mean R_2 values were calculated together with their standard deviation. In addition, the mean R_2^* value of the liver, measured from the SOFIDSE data, was calculated and subtracted from the R_2^* maps in order to obtain 'virtual' ΔR_2^* maps that correspond to the conventional quantification method. Assuming homogeneous liver tissue, these ΔR_2^* maps will represent the variation in R_2^* induced by field inhomogeneities and therefore must be comparable to $R'_{2\ SOFIDSE}$ values. The distribution of these ΔR_2^* values was compared to the distribution of $R'_{2\ SOFIDSE}$ values and means together with their standard deviation were calculated.

RESULTS

Phantom

Signal intensities measured from the gel series containing a range of Ho-MS showed mono-exponential signal decay for all concentrations for both the FID of the SOFIDSE data (Figure 1a) and the SSE data (Figure 1b). A monoexponential fit (R^2 = 1 for all concentrations and both datasets) provided S_0 values for both the SOFIDSE and SSE data (Figure 1c). Estimated S_0 values were slightly higher for SOFIDSE as compared with SSE, including the 0 mg/ml sample. The mean SNR ± SD of the estimated S_0 values of the entire range of Ho-MS was 429 ± 9 for SOFIDSE and 393 ± 13 for SSE, resulting in an S_0 overestimation of 9% on average. Variations in S_0 over the range of microspheres concentrations were observed showing similar deviations for SOFIDSE and SSE but no correlation with the concentration Ho-MS. Signal intensities of the upslope and downslope of the spin echo envelope obtained from the SOFIDSE data, revealed obvious deviation from monoexponential signal behavior (Figure 2), especially for higher Ho-MS concentrations.

R_2 values that were obtained by either monoexponential fitting of the SSE data or determined by SOFIDSE data (SE = 30 ms) both showed a linear dependency on concentration

(Figure 3a). For SOFIDSE slightly higher values were found as compared to SSE values, as a result of the higher SOFIDSE S_0 values, leading to an overestimation of 5% on average for SOFIDSE. No significant relation of this overestimation with concentration Ho-MS was found. From a linear fit to the R_2 values, a Ho-MS r_2 relaxivity of 8.6 ± 1.0 s^{-1} and 8.7 ± 1.3 s^{-1} (95% confidence bounds) was found for respectively SOFIDSE and SSE at 1.5 Tesla. From a statistical analysis, a correlation coefficient of 1 (P = 1.5 ·10^{-6}) was found for the two methods (Figure 3b).

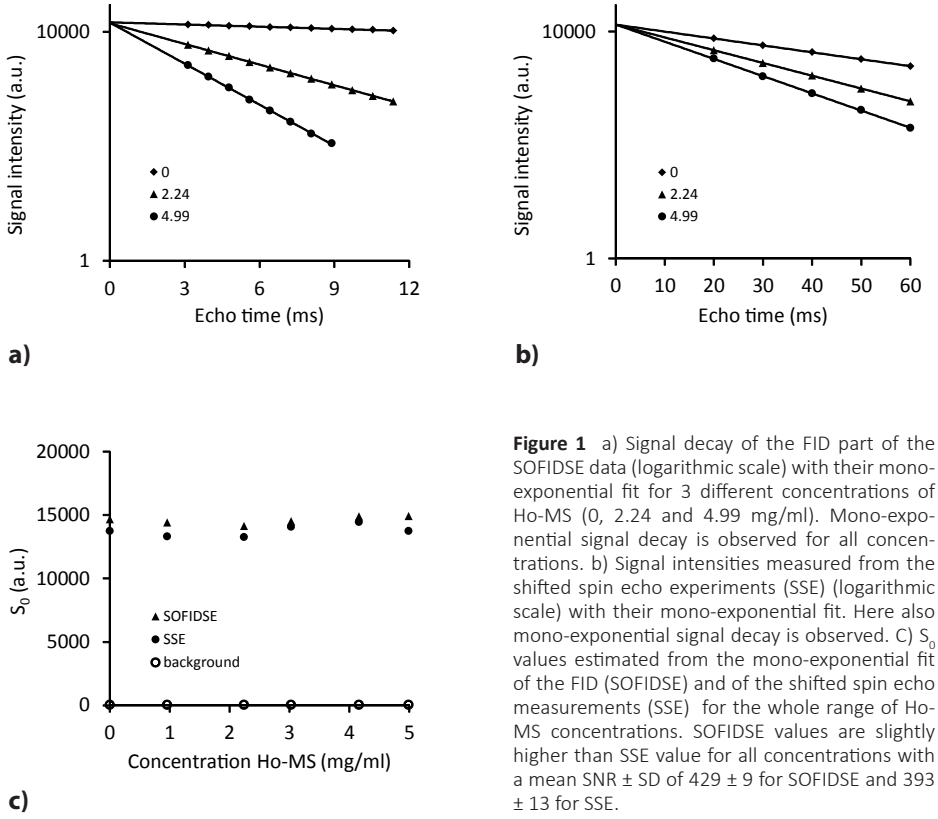

Figure 1 a) Signal decay of the FID part of the SOFIDSE data (logarithmic scale) with their mono-exponential fit for 3 different concentrations of Ho-MS (0, 2.24 and 4.99 mg/ml). Mono-exponential signal decay is observed for all concentrations. b) Signal intensities measured from the shifted spin echo experiments (SSE) (logarithmic scale) with their mono-exponential fit. Here also mono-exponential signal decay is observed. C) S_0 values estimated from the mono-exponential fit of the FID (SOFIDSE) and of the shifted spin echo measurements (SSE) for the whole range of Ho-MS concentrations. SOFIDSE values are slightly higher than SSE value for all concentrations with a mean SNR ± SD of 429 ± 9 for SOFIDSE and 393 ± 13 for SSE.

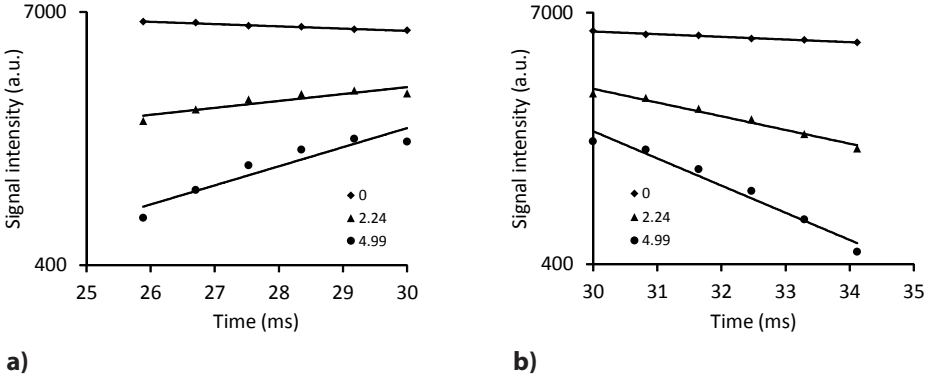

Figure 2 Upslope (a) and downslope (b) of the spin echo envelope of the SOFIDSE data around the spin echo time of 30 ms on a logarithmic scale. It is clearly shown that signal of both the upslope and downslope of the SE envelope deviates from mono-exponential behavior, complicating quantification.

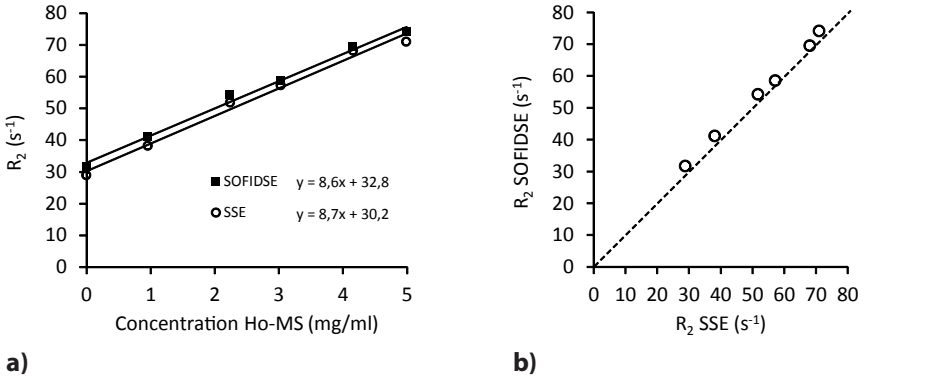

Figure 3 a) R_2 values, determined from a mono-exponential fit to the estimated S_0 in combination with a single spin echo measurement (SOFIDSE) and from a mono-exponential fit to the shifted spin echo (SSE) measurement as a function of concentration Ho-MS. b) R_2 values determined by SOFIDSE vs R_2 values determined by SSE. A good correlation is observed between the two methods although a small overestimation is found for the SOFIDSE method when compared to unity (dashed line).

In Figure 4, the $R_{2\ SOFIDSE}^{'}$ values determined by subsequently subtracting the R_2 values obtained from SSE and SOFIDSE from the R_2^* values determined from the FID of the SOFIDSE data, are plotted as a function of concentration Ho-MS. A linear relationship was found for both methods between $R_{2\ SOFIDSE}^{'}$ values and concentration microspheres resulting in an $r_{2\ SOFIDSE}^{'}$ relaxivity of 99 ± 5 $s^{-1}.mg^{-1}.ml$ (95% confidence interval) for the Ho-MS at 1.5 Tesla for both methods. A correlation coefficient of 1 ($P = 9 \cdot 10^{-11}$) was found for the $R_{2\ SOFIDSE}^{'}$ values of the two methods (Figure 4b). Figure 4a also shows the R_2^* values that were determined from the FID and normalized by subtraction of the R_2^* value of the 0 mg/ml

sample. By a linear fit to these values an r_2^* relaxivity of 108 ± 7 $s^{-1}.mg^{-1}.ml$ was found.

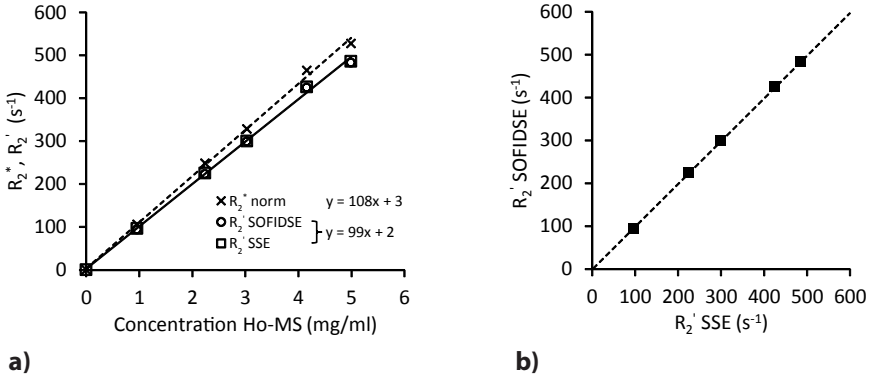

Figure 4 a) R_2^* values as determined from gradient echo sampling of the FID normalized by the R_2^* value of the 0 mg/ml sample (R_2^* norm) and R_2' values determined by subtraction of SOFIDSE R_2 values from SOFIDSE R_2^* values (R_2' SOFIDSE) and by subtraction of SSE R_2 values from SOFIDSE R_2^* values (R_2' SSE). b) R_2' SOFIDSE values versus R_2' SSE values display a high correlation (correlation coefficient = 1, p-value = $3x10^{-12}$).

R_2 values determined from the monoexponential fit of the SSE data of the second gel series, containing various concentrations of agarose but no Ho-MS are plotted in Figure 5a. Increasing R_2 values were found for increasing agarose concentration, where the R_2 ranged from 17 s^{-1} to 29 s^{-1}, corresponding to T_2 values of 58 ms to 35 ms, for the agarose concentration range of 1% to 2.26% (weight/weight). ADC values of the same gel series, determined from the diffusion weighted images, showed no dependency on agarose concentration (Figure 5b) demonstrating that only the intrinsic R_2 values of the samples differed.

$R_{2\ SOFIDSE}'$ values of the third gel series, containing various concentrations of agarose and thus various R_2 values, and approximately 1 mg/ml Ho-MS, showed fluctuations that corresponded to the known fluctuations in concentration Ho-MS (Figure 6a). $R_{2\ SOFIDSE}'$ values, corrected for these fluctuations showed no dependency on sample R_2, whereas R_2^* values showed an increase for increasing sample R_2 (Figure 6b).

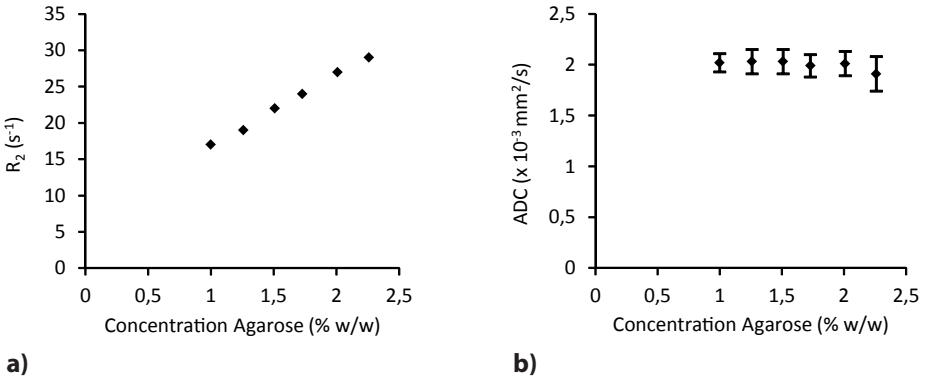

Figure 5 a) R_2 values as a function of agarose content measured from the gel series containing no Ho-MS. An increase of R_2 is observed for increasing agarose content. b) ADC values as a function of agarose content measured from the same gel series. No changes in ADC value are observed for changes in agarose content.

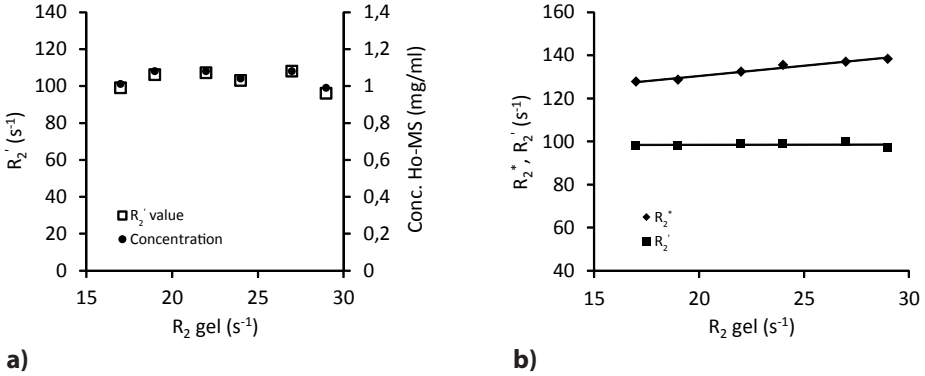

Figure 6 a) R_2' values (●) and corresponding Ho-MS concentrations (□) as a function of baseline R_2 value, measured from the gel series with varying agarose content and on average 1 mg/ml Ho-MS. No influence of the baseline R_2 value on R_2' is visible. Fluctuations that are observed clearly correspond to fluctuations in Ho-MS concentrations. b) R_2^* and R_2' values normalized for Ho-MS concentration as a function of baseline R_2. R_2^* depends on the R_2 value of the gel, whereas for R_2', no such dependency is found.

Healthy volunteer

R_2 maps of the liver of the healthy volunteer (containing no Ho-MS) determined from the SOFIDSE data showed good agreement with R_2 maps determined from the dual echo data (Figure 7). Differences were observed particularly at the locations of large blood vessels. These differences were also clearly observed in the spin echo images that were used to determine R_2 (Figure 7, bottom row). The first spin echo image of the dual echo sequence showed several hyper and hypo intense areas, where in the central spin echo image of the SOFIDSE data this effect was much less pronounced. However, in areas where no large

vessels were present, R_2 values, measured in a region of interest (Figure 7, white circle) were similar for both methods: 31 ± 6 s^{-1} and 30 ± 12 s^{-1} for respectively SOFIDSE and dual echo spin echo. $R'_{2\ SOFIDSE}$ maps (Figure 8a) and the R_2^* maps that were determined from only the FID part of the SOFIDSE data and normalized by their mean value (Figure 8b) showed good visual resemblance and no obvious differences. A quantitative assessment, comparing the distributions of R_2, $R'_{2\ SOFIDSE}$ and R_2^* that were found in the entire liver, showed that R_2 values obtained by SOFIDSE were very similar to R_2 values obtained by the dual echo acquisition (Figure 9a). On average, a mean R_2 value of 30 s^{-1} with a standard deviation of 10 s^{-1} was found for SOFIDSE whereas for the dual echo acquisition these values were 28 s^{-1} and 17 s^{-1}, respectively. When comparing $R'_{2\ SOFIDSE}$ values to normalized R_2^* values obtained from the FID, where the normalized R_2^* values mimicked ΔR_2^* values, a very good agreement was found between the two, both for mean $R'_{2\ SOFIDSE}$ and mean ΔR_2^* values (2 s^{-1} and 0 s^{-1} respectively) as well as for their standard deviations (19 s^{-1} and 20 s^{-1} respectively) (Figure 9b). A slight deviation from 0 was found for the SOFIDSE R'_2 values.

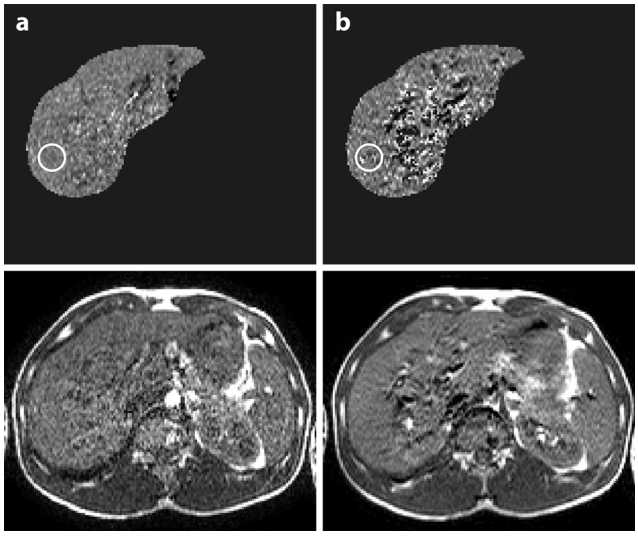

Figure 7 Top row: R_2 maps on a scale of 10 to 76 s^{-1} determined from SOFIDSE data (a) en dual echo data (b). Similar values are found for both methods although dual echo data shows differences at locations of large vessels. These differences are also visible in the corresponding spin echo images (bottom row) where hypo and hyper-intense areas are observed in the first spin echo image (20 ms) of the dual echo data (b). These hypo- and hyper-intense areas are much less visible in the central spin echo image (20 ms) of the SOFIDSE data (a). From an ROI analysis (white circle) similar R_2 values were found for normal liver tissue for both methods (R_2 = 31 ± 6 s^{-1} for SOFIDSE and R_2 = 30 ± 12 s^{-1} for dual echo spin echo).

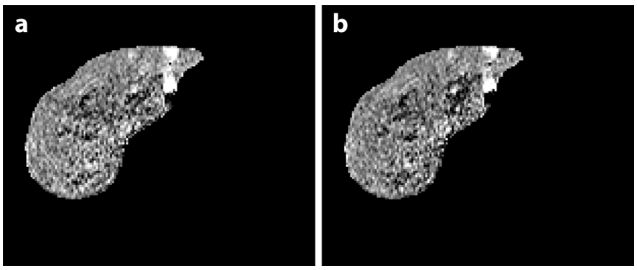

Figure 8 One slice of the R_2' maps determined by SOFIDSE (a) and the same slice, determined from the FID of the SOFIDSE data and normalized by the mean R_2^* value of the entire liver (b). The normalized map on the right mimics a ΔR_2^* map resulting from the conventional quantification method. No obvious differences are observed between the two maps.

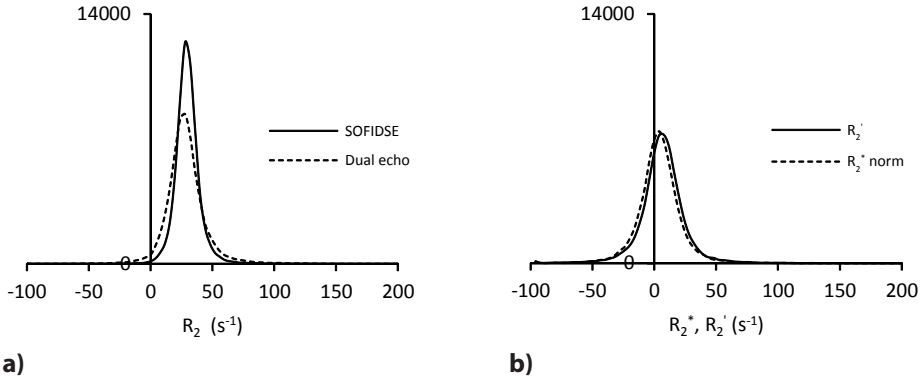

Figure 9 a) Distributions of R_2 values found in the entire liver for the SOFIDSE method (solid line) and the dual echo method (dashed line). b) R_2' values, determined by SOFIDSE, and normalized R_2^* values, determined by subtraction of the mean R_2^* value of the liver from the voxel R_2^* values, that were found in the entire liver of the subject.

DISCUSSION

In this chapter we presented a method to simultaneously estimate R_2^*, R_2 and R_2' values for quantification of Ho-MS, paramagnetic microspheres that can be employed for radioembolization.

The method assumes that both the free induction decay and the spin echo decay can be described by a monoexponential function with identical initial value S_0. In that case, S_0 determined from the FID can subsequently be used in combination with a single spin echo to estimate the spin echo decay rate. Phantom experiments clearly showed that the FID as well as the spin echo decay of Ho-MS containing systems are monoexponential, irrespective of the microsphere concentration. The S_0 values that were obtained by

SOFIDSE showed a small overestimation (9%) independent of the concentration Ho-MS, as compared with the reference values obtained by SSE. This overestimation may be the result of differences in excitation and refocusing slice profiles and non-perfect refocusing pulses, reducing the absolute signal at the spin echo time which leads to lower estimated S_0 values. As a consequence of this S_0 overestimation, SOFIDSE showed a concentration independent overestimation of 5% on average as compared with SSE R_2 values, which is acceptable for quantification purposes.

The monoexponential behavior of both FID and SE for the entire range of Ho-MS concentrations that was investigated, demonstrated that the signal decay of Ho-MS containing systems can be characterized by an addition of monoexponential components as given by Equations [3] and [4]. Therefore, the Ho-MS induced signal decay in SOFIDSE measurements, $R_{2\ SOFIDSE}^{'}$, can be determined by a subtraction of R_2^* and R_2 as given by Equation [5] and this $R_{2\ SOFIDSE}^{'}$ value is, unlike R_2^*, independent on the R_2 value of the tissue as was clearly demonstrated by the measurements performed on the phantom with varying intrinsic R_2 values (Figure 7). The introduction of this $R_{2\ SOFIDSE}^{'}$ value that only characterizes the reversible dephasing effect of the microspheres leads to the introduction of the Ho-MS relaxivity parameter $r_{2\ SOFIDSE}^{'}$, which linearly relates the local $R_{2\ SOFIDSE}^{'}$ to the concentration microspheres (Equation [6]). This $r_{2\ SOFIDSE}^{'}$ value was empirically found to be 99 ± 5 $s^{-1}.mg^{-1}.ml$ at 1.5 T for the used microspheres with a holmium content of 18.9% whereas the r_2^* relaxivity was found to be 108 ± 7 $s^{-1}.mg^{-1}.ml$.

Clinical value

Data acquired from the healthy volunteer showed that in vivo, R_2 values obtained by SOFIDSE closely corresponded with R_2 values obtained by a dual spin echo technique, demonstrating the clinical applicability of the method. For Ho-MS quantification in clinical practice, SOFIDSE adds value for several reasons. First of all, it allows for R_2 measurements using a short acquisition time since only a single spin echo is required. Second, within the same time needed to measure R_2, also R_2^* is measured which was shown to enable Ho-MS quantification purely based on $R_2^{'}$ dephasing effects. By combining FID and SE in a single acquisition, SOFIDSE basically eliminates the need for acquisition of baseline MRI data prior to administration of the microspheres, preventing errors due to misalignment of pre- and posttherapy images and errors invoked by tissue changes. This will especially create possibilities for quantitative imaging during the radioembolization procedure, since image processing and user intervention are minimal and $R_{2\ SOFIDSE}^{'}$ maps can be calculated fast on site. A third benefit of the method is that the R_2^* or $R_{2\ SOFIDSE}^{'}$ maps are intrinsically co-registered to the anatomical spin echo image, facilitating segmentation of the maps based on the contrast of the spin echo image.

In this work, we neglected the influence of macroscopic field inhomogeneities that might be present in the tissue due to for example air-tissue interfaces near the lungs and stomach. Such macroscopic fields will lead to increased $R_{2\,SOFIDSE}^{'}$ values that will be misinterpreted as concentrations of Ho-MS. The actual influence of these macroscopic effects is expected to be small. For instance, the in vivo $R_{2\,SOFIDSE}^{'}$ data of the healthy volunteer examined in this work showed an offset of 2 s^{-1} for the mean $R_2^{'}$ value of the liver, which would hypothetically correspond to a mean concentration offset of 0.02 mg/ml using a $r_2^{'}$ of 99 $s^{-1}.mg^{-1}.ml$. Furthermore, correcting for these macroscopic effects may be relatively easy by utilizing post processing techniques (95).

In the study reported here, we showed the applicability of SOFIDSE for quantification of Ho-MS, however its use is not restricted to Ho-MS only. If the system under investigation complies with the condition described in this work, i.e., if it can be assumed that S_0 is identical for both FID and SE decay, than SOFIDSE can be used to estimate R_2^* and R_2. Whether the use of SOFIDSE is beneficial, compared to methods earlier proposed in literature (84, 85), will depend on the clinical context. In our case, where temporal changes in tissue R_2, non-monoexponentiality of the spin echo envelope, and the need for short imaging times in liver imaging limit the use of existing acquisition methods, the advantages of SOFIDSE are fully exploited.

In conclusion, S_0 estimation of the free induction decay combined with a single spin echo measurement can be used to simultaneously measure R_2^*, R_2 and $R_2^{'}$ for R_2 insensitive quantification of Ho-MS within a single acquisition.

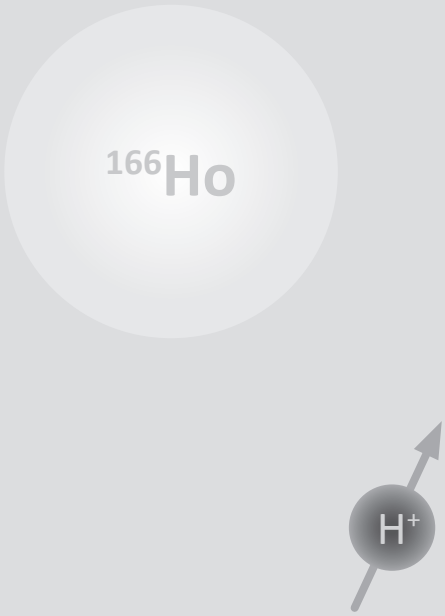
166Ho
H+

Chapter 6

Influence of diffusion on relaxivity parameters

"The purpose of this work was to investigate the dependency of the holmium relaxivity parameter r_2, as obtained by utilizing SOFIDSE, on the ADC of the tissue in which the microspheres are present in order to estimate the influence of diffusion on $r'_{2\ SOFIDSE}$."

INTRODUCTION

MRI-based biodistribution assessment of holmium-166 loaded microspheres after radioembolization is based on MR relaxometry, by relating the holmium enhanced transversal signal decay to local concentrations of microspheres (96). By sampling the free induction decay (FID) of the MR signal, utilizing a multi-gradient echo sequence, the transverse relaxation rate R_2^* is measured both prior to and after radioembolization, from which the microsphere induced ΔR_2^* is obtained. This ΔR_2^* is subsequently related to the local microsphere concentration by the microspheres' relaxivity r_2^* (53, 96), which represents the relaxation rate per unit concentration. Although this strategy has been shown to provide a good biodistribution measure for absorbed radiation dose estimation (40, 96), the main limitation is that it relies on two separate image acquisitions. This necessitates accurate image registration to avoid errors introduced by spatial variations in R_2^* due to tissue characteristics. Furthermore, it makes the method sensitive to temporal changes in tissue R_2 values which may occur in the interval between the pre- and posttherapy image acquisitions because of development of necrotic, edematous or hemorrhagic changes as a consequence of the therapy. For that reason, recently, a method was proposed in which both the FID relaxation rate R_2^* and the spin echo relaxation rate R_2 are derived from a single acquisition by using S_0 estimation of the FID in combination with a single spin echo (SOFIDSE) (see Chapter 5). By subtracting R_2 from R_2^*, the microsphere-induced reversible signal decay characterized by $R'_{2\,SOFIDSE}$ is obtained that is linearly related to the microsphere concentration by the relaxivity $r'_{2\,SOFIDSE}$. This $r'_{2\,SOFIDSE}$ was empirically determined to be 99 $s^{-1}.mg^{-1}.ml$ at 1.5T for microspheres with a holmium load of 18.9%. The main advantage of this method is that, upon assuming that macroscopic background gradients are negligible or may be corrected for (95), only a post-radioembolization image acquisition is required and that the method is insensitive to changes in tissue R_2. However, owing to the inclusion of a spin echo measurement, the estimated $R'_{2\,SOFIDSE}$ values may become sensitive to the degree of proton diffusion that is present in the tissue. Although R_2^* is known to be unaffected by diffusion and can be described in terms of static dephasing (85), the spin echo amplitude of holmium microsphere containing systems has been found to depend on the local degree of diffusion (53). As a consequence, the effective R_2 of holmium microsphere containing systems may depend on the diffusion coefficient which means that the relaxivity r_2 is not a fixed constant. As a result, $r'_{2\,SOFIDSE}$, determined by subtraction of r_2 from r_2^*, will depend on the diffusion coefficient. In vivo, the degree of diffusion, represented by the apparent diffusion coefficient (ADC) in diffusion weighted MR imaging, depends on various tissue characteristics and has been shown to differ between normal liver tissue and tumorous tissue (97). These differences in ADC, combined with using a

fixed $r'_{2\,SOFIDSE}$ value for in vivo holmium quantification, may yield errors in the determined concentrations of microspheres.

The purpose of this work was to investigate the dependency of the holmium relaxivity parameter r_2, as obtained by utilizing SOFIDSE, on the ADC of the tissue in which the microspheres are present, in order to estimate the influence of diffusion on $r'_{2\,SOFIDSE}$. This was done by relaxation measurements on a phantom setup for a clinically relevant range of microsphere concentrations and ADC values. Because Ho-MS containing systems have been shown to comply with the criteria defined for the theoretical model of strong field behavior (53, 92), which describes the NMR signal of systems in which diffusion can play a role, especially in spin echo sequences, this model was used as a basis for data processing and interpretation of the obtained experimental results.

MATERIALS AND METHODS

Model for numerical simulation

Numerical simulations were performed based on the strong field behavior model of Jensen and Chandra (92). In this model the additional signal decay due to compact objects (microspheres) is described by

$$S(T) \approx \exp\left[-f\left(k_1 - ik_2\right)T/\tau_0\right] \qquad [1]$$

for the free induction decay, which can be reduced to

$$S(T) \approx \exp\left[-fk_1T/\tau_0\right] \qquad [2]$$

when only the signal magnitude is considered. For the single spin echo decay, the additional signal decay is described by

$$S(T) \approx \exp\left[-fk_3\left(T^3/12\tau_0^2\tau_1\right)^{3/8}\right] \qquad [3]$$

It should be emphasized that Equation [3] is only valid at the spin echo time (92) and does not represent an expression for the entire spin echo envelope. The included parameters are defined as follows. The volume fraction of the objects f is given by

$$f = \frac{c}{\rho} \qquad [4]$$

with c the concentration of microspheres and ρ the microsphere material density. *k1* and *k3* are geometrical factors given by

$$k_1 = \frac{2\pi}{9\sqrt{3}} \qquad [5]$$

$$k_3 = 2.2184 \left\langle \left(\frac{V_n}{V_0} \right)^{3/4} \right\rangle_{obj} \qquad [6]$$

with V_0 the average volume of the objects and V_n the volume of the nth object; the angle brackets indicate an average over all objects. The time scales τ_0 and τ_1 are defined by

$$\tau_0 = \frac{1}{|\Delta\chi|\gamma B_0} \qquad [7]$$

$$\tau_1 = \frac{V_0^{2/3}}{D} \qquad [8]$$

with $\Delta\chi$ the difference between the volume susceptibility of the objects and the medium (dimensionless in SI units), γ the gyromagnetic ratio, B_0 the main magnetic field and D the diffusion coefficient of the tissue in which the objects reside. Substitution of these parameters into Equations [2] and [3] gives

$$S(T) \approx \exp\left[-\left(\frac{2\pi\Delta\chi\gamma B_0}{9\sqrt{3}\rho} \right) cT \right] \qquad [9]$$

for the FID, where the term between the brackets represents the objects' r_2^* relaxivity

$$r_2^* = \frac{2\pi\Delta\chi\gamma B_0}{9\sqrt{3}\rho} \qquad [10]$$

and

$$S(T) \approx \exp\left[-\left(\frac{2.2184\left(\Delta\chi\gamma B_0\right)^{6/8} D^{3/8}}{12^{3/8} V_0^{1/4}} \right) \frac{1}{\rho} cT^{9/8} \right] \qquad [11]$$

for the spin echo decay at echo time *T* where V_r/V_0 from Equation [6] was assumed to be 1. Equations [9] and [11] show that the FID is independent of diffusion and is described by a pure monoexponent but that the spin echo decay deviates from monoexponential behavior and depends on the diffusion coefficient. Equation [11] can be rewritten to

$$S(TE) \approx \exp\left[-\left(\frac{2.2184\left(\Delta\chi\gamma B_0\right)^{6/8} D^{3/8} TE^{1/8}}{12^{3/8} V_0^{1/4}} \frac{1}{\rho} \right) cT \right] \qquad [12]$$

where the term between brackets now represents the relaxivity r_2 for a monoexponential signal decay

$$r_2 = \frac{2.2184\left(\Delta\chi\gamma B_0\right)^{6/8} D^{3/8} TE^{1/8}}{12^{3/8} V_0^{1/4} \rho} \qquad [13]$$

The factor $TE^{1/8}$ in this decay parameter renders the relaxivity echo time dependent, which means that r_2 cannot be considered a constant that describes the decay over the entire time range but only applies to echo time TE. However, by writing the signal decay in this way, simulation results can be compared with r_2 relaxivity results obtained from experimental SOFIDSE data.

Phantom preparation

An agarose gel series was prepared in 25 ml plastic tubes using 2% agarose (weight/weight) in $MnCl_2.4H_2O$ doped water (30 mg/L). During preparation, non-radioactive holmium microspheres, prepared as described by Nijsen et al. (36), were added to the gel in concentrations of 0.94, 2.15, 3.07, 4.08 and 4.98 mg/ml. One sample was left blank (0mg/ml). The microspheres had a density of 1.4 g/ml and a holmium content of 18.9% (weight/weight) and the microsphere diameter ranged between 20 and 50 µm with a mean diameter of 30 µm. In order to vary the diffusion coefficient of the agar gels, the temperature of the phantom was varied. This was done in two separate steps to obtain a full range of clinically relevant ADC values. In the first step, the phantom was kept in melting water (0°C) for five hours and subsequently transferred to the MRI site after which data were acquired until the phantom reached room temperature (~20°C). In the second step, the phantom was placed in a water bath at 50°C for five hours, transferred to the MRI site and images were acquired until the phantom reached room temperature.

MRI data acquisition

MRI data was acquired on a 1.5 T whole body system (Achieva, Philips Healthcare, Best, the Netherlands) using an 8-channel head receive coil.

ADC data was acquired using a 2D diffusion weighted sequence with b-values of 0, 100, 200 and 300 s/mm^2 and an effective echo time of 46 ms. Diffusion sensitizing gradients were applied in three orthogonal directions to achieve isotropic diffusion weighting. Other imaging parameters included: repetition time (TR) = 1500 ms; slice thickness = 12 mm; field of view (FOV) = 128 x 128 mm^2; matrix = 64^2; and readout bandwidth = 2042 Hz/pixel; resulting in a total acquisition time of 16m5s.

R_2^* and R_2 data were acquired using the SOFIDSE method (Chapter 5) utilizing a custom-built research patch (Philips Research Laboratories, Hamburg, Germany) (94). A 2D sequence was used, sampling the FID by 11 gradient echoes (TE_1 = 3.1 ms/ΔTE = 0.8ms) followed by sampling one spin echo envelope by 11 gradient echoes with ΔTE = 0.8ms, centered around the spin echo peak at TE = 30 ms. Other parameters included: TR = 2000 ms; slice thickness = 10 mm; FOV = 128 x 128 mm^2; matrix = 64^2; and readout bandwidth = 1783 Hz/pixel; with a total acquisition time of 4m30s.

Relaxivity and ADC measurements were performed alternatingly, starting with ADC measurements both for the heating up and cooling down experiment.

MRI data processing

ADC values of the 0 mg/ml sample at each time point were estimated from the diffusion weighted data using a monoexponential fit: $S(b) = S(0) \cdot \exp[-ADC \cdot b]$, where b defines the degree of diffusion weighting, which depends on the strength, duration and spacing of the applied gradients, and S(b) is the corresponding signal intensity. ADC values corresponding to the time points at which the R_2^* and R_2 relaxation measurements were performed were estimated by the mean ADC value of the ADC measurements prior to and after the relaxation measurement. Temperature values were estimated from the ADC values taking 0°C as the reference temperature for the first ADC value of the heating up experiment and 50°C as the reference temperature for the first ADC value of the cooling down experiment and assuming a linear relation between ADC and temperature for agar gels (98).

Relaxivity data were processed as follows. First, a monoexponential fit ($S(TE) = S_0 \cdot \exp[-R_2^* \cdot TE]$) was applied to the gradient echo signal intensities of the FID part of the SOFIDSE data, from which R_2^* and S_0 values were obtained for each concentration. A threshold was applied excluding signal intensities from the fitting procedure with a signal-to-noise ratio (SNR) lower than 3, where the noise was estimated by the standard deviation of the background signal. Subsequently, the estimated S_0 values were combined with the signal intensities of the central spin echo sample of the SOFIDSE data and R_2 values were deter-

mined for each Ho-MS concentration by $R_2 = \ln (S_0/S(TE))/TE$.
For each concentration of microspheres, the Ho-MS induced ΔR_2^* and ΔR_2 were determined by, respectively, subtracting the R_2^* and R_2 value of the gel sample containing no Ho-MS in order to eliminate the influence of macroscopic background gradients. Subsequently, r_2^* relaxivity values were obtained by a linear fit to the ΔR_2^* values. Since the susceptibility of holmium is known to be dependent on temperature (99), the microsphere susceptibility for each temperature was determined using Equation [10], assuming no influence of diffusion. Similarly to the procedure for r_2^*, r_2 relaxivity values were obtained from a linear fit to the ΔR values.

Numerical calculations

Simulated r_2 relaxivity values where obtained from Equation [12] using the following parameters: $B_0 = 1.5T$; $\gamma = 2.68 \cdot 10^8$ rad/s/T; $TE = 30 \cdot 10^{-3}$ s; D values (in 10^{-3} mm^2/s) corresponding to the time points of the relaxation measurements were taken as found from the mean ADC value of the ADC measurements prior to and after the relaxation measurement. V_0 was taken as

$$V_0 = \frac{4}{3}\pi r^3 \qquad [14]$$

with r the mean radius of the microspheres. To investigate the influence of the chosen microsphere radius, r_2 values were calculated for three different radii: 15, 20 and 25 µm. For these three cases, the susceptibility values as obtained from the experimental r_2^* values, corresponding to the input ADC values, were used as input for $\Delta\chi$. For the radius of 15 µm, equal to the mean radius of the microspheres used for the experiments, r_2 values were also calculated using a fixed $\Delta\chi$ value. These r_2 values were compared with values obtained by using a varying $\Delta\chi$, in order to investigate the contribution of the temperature dependency of $\Delta\chi$ on r_2. This fixed $\Delta\chi$ value was chosen as the susceptibility measured at room temperature. To determine the range of $r'_{2\,SOFIDSE}$ values that are relevant for in vivo biodistribution measurements, $r'_{2\,SOFIDSE}$ values were estimated from a subtraction of r_2 from r_2^*, where for r_2^* a fixed value was used that was experimentally found for the temperature corresponding to body temperature (~37°C) and for r_2 the values that were found over the entire ADC and temperature range.

RESULTS

The ADC value measured from the agarose sample containing no holmium microspheres increased from 1.18 x 10^{-3} mm^2/s to 1.96 x 10^{-3} mm^2/s during heating up from ~0°C up to room temperature (Figure 1a). During cooling down from ~50°C to room temperature, the ADC decreased from 3.86 x 10^{-3} mm^2/s to 2.20 x 10^{-3} mm^2/s (Figure 1b). ΔR_2^* values as well as ΔR_2 values changed during heating up and cooling down for all concentrations Ho-MS. ΔR_2^* decreased during heating up and increased during cooling down, whereas ΔR_2 increased during heating up and decreased during cooling down (Figure 2). Over the entire range of temperatures, ΔR_2^* decreased for increasing temperature and ΔR_2 increased for increasing temperature and corresponding ADC value (Figure 3). For the concentrations of 0.94, 2.15, 3.07, 4.08 and 4.98 mg/ml Ho-MS, the total change in ΔR_2^* was, respectively, 13, 30, 38, 42 and 57 s^{-1} for baseline values of 100, 243, 333, 408 and 528 s^{-1} at room temperature. The change in ΔR_2 for these concentrations was 1.8, 5.5, 7.7, 10.5 and 12.2 s^{-1} for, respectively, baseline values of 8.7, 20.5, 27.0, 31.5 and 41.4 s^{-1}. The relaxivity r_2^*, obtained for each time point from a linear fit to the ΔR_2^* values, decreased from 108.3 $s^{-1}.mg^{-1}.ml$ to 98.3 $s^{-1}.mg^{-1}.ml$ for an estimated temperature range of 1.1°C to 46.3°C and corresponding ADC range of 1.24 x 10^{-3} mm^2/s to 3.68 x 10^{-3} mm^2/s (Figure 4). The corresponding volume susceptibility $\Delta\chi$, obtained from the r_2^* values using Equation [10], decreased from 946 ppm to 858 ppm over this temperature range. The relaxivity r_2, obtained from a linear fit to the concentration-dependent R_2 values for each time point, increased from 6.7 $s^{-1}.mg^{-1}.ml$ to 9.3 $s^{-1}.mg^{-1}.ml$ over the given temperature range and the corresponding ADC range (Figure 5a). Spin echo relaxivity values that were obtained from numerical simulations, for a microsphere radius or 15µm and temperature-dependent susceptibility $\Delta\chi$ (obtained from r_2^*), showed similar increasing behavior but higher r_2 values (range 8.2 - 11.4 $s^{-1}.mg^{-1}.ml$). Results for a microsphere radius of 20 µm showed good numerical agreement with the experimental values (range 6.6 - 9.3 $s^{-1}.mg^{-1}.ml$). Using a radius of 25µm resulted in significantly lower r_2 values (range 5.6 – 7.8 $s^{-1}.mg^{-1}.ml$). Figure 5b shows numerical results obtained using a microsphere radius of 15 µm and, respectively, a temperature dependent $\Delta\chi$ and a $\Delta\chi$ with a fixed value of 894 ppm (value at room temperature). A minor dependency of r_2 on varying $\Delta\chi$ was observed. From a subtraction of r_2^* and r_2 values the $r'_{2\ SOFIDSE}$ relaxivity as a function of ADC was found (Figure 6). Here, for r_2^* a fixed value of 99 $s^{-1}.mg^{-1}.ml$ was used (r_2^* at ~37°C, Figure 4) to obtain $r'_{2\ SOFIDSE}$ values relevant for in vivo Ho-MS quantification. A decrease of 2.6 $s^{-1}.mg^{-1}.ml$ starting from a value of 92.3 $s^{-1}.mg^{-1}.ml$ was found over the ADC range of 1.24 x 10^{-3} mm^2/s to 3.86 x 10^{-3} mm^2/s, which is a total change of 2.8%.

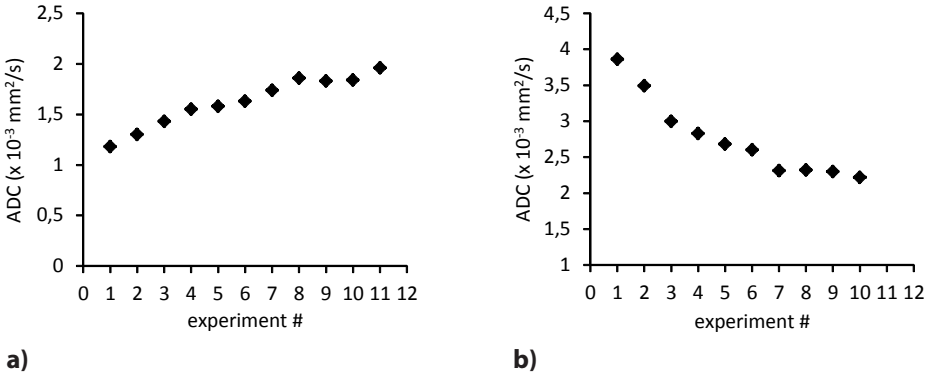

Figure 1 ADC values measured from the gel sample containing no Ho-MS during heating up from ~0°C to room temperature (a) and during cooling down from ~50° to room temperature (b).

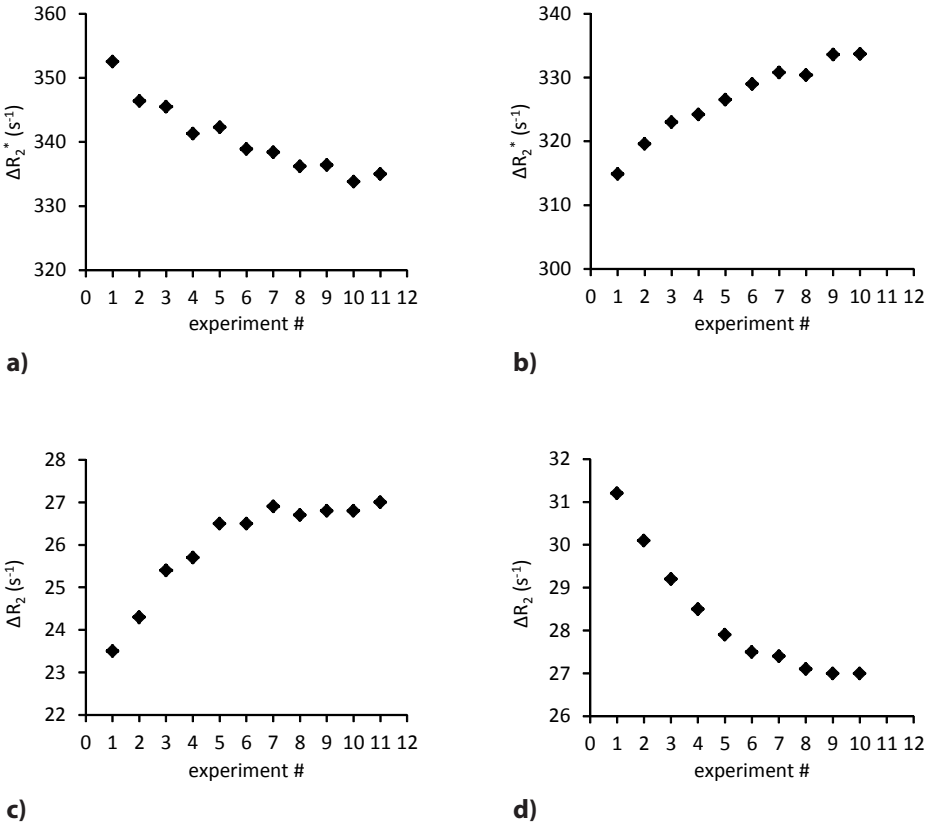

Figure 2 ΔR_2^* (a, b) and ΔR_2 (c, d) values of the 3 mg/ml sample during heating up from ~0°C to room temperature (a, c) and during cooling down from ~50°C to room temperature (b, d).

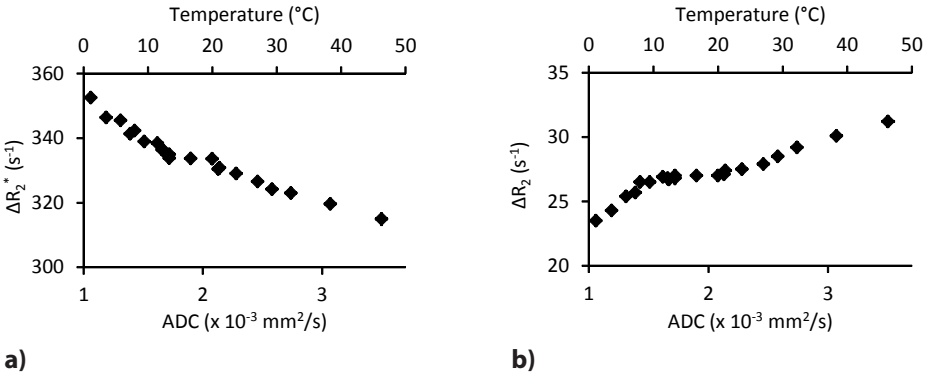

Figure 3 ΔR_2^* (a) and ΔR_2 values (b) for a Ho-MS concentration of 3 mg/ml as a function of ADC and corresponding temperature. ΔR_2^* decreased for increasing temperature and ADC whereas ΔR_2 increased for increasing temperature and ADC.

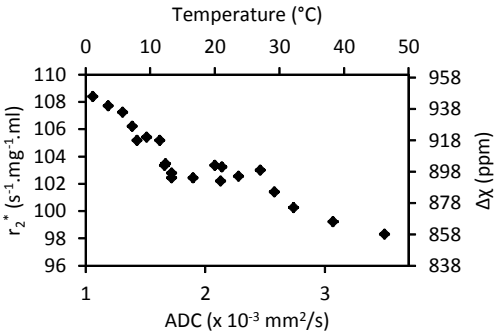

Figure 4 Relaxivity r_2^* of Ho-MS at 1.5T obtained from a linear fit of measured ΔR_2^* values with their corresponding volume susceptibility, assuming static dephasing. The relaxivity and susceptibility values are plotted as a function of corresponding ADC value for comparison with r_2 values and as a function of the corresponding estimated temperatures on which they actually depend.

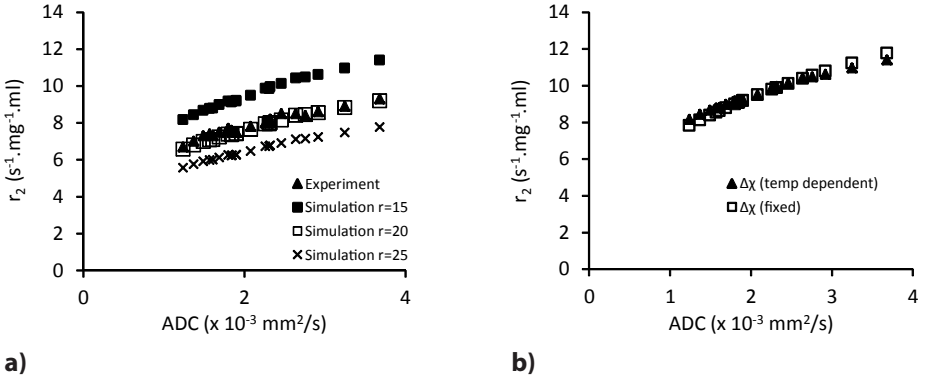

Figure 5 a) Experimental and numerical r_2 relaxivity values for Ho-MS at 1.5T as a function of ADC. Simulation values are shown for microsphere radii of 15, 20 and 25 µm. b) Numerical r_2 values for a microsphere radius of 15 µm with the susceptibility Δχ dependent on temperature as determined from r_2^* and with the susceptibility Δχ having a fixed value of 894 ppm (value at room temperature).

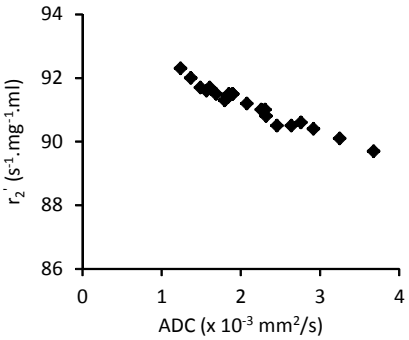

Figure 6 $r'_{2\ SOFIDSE}$ as obtained from a subtraction of r_2^* and r_2 where for r_2^* a value of 99 $s^{-1}.mg^{-1}.ml$ was used (~r_2^* value at body temperature).

DISCUSSION

The results of the relaxation measurements described in this chapter clearly showed that the degree of diffusion in the tissue in which Ho-MS reside influences the relaxivity r_2 of the microspheres. r_2 values that were measured from a phantom setup of which the diffusion coefficient was varied by changing the temperature, increased from 6.7 $s^{-1}.mg^{-1}.ml$ to 9.3 $s^{-1}.mg^{-1}.ml$ over an apparent diffusion coefficient range of 1.24 x 10^{-3} mm^2/s to 3.86 x 10^{-3} mm^2/s. Numerical results, based on the strong field behavior model of Jensen and Chandra (92), showed a similar increase. As a consequence, the $r'_{2\ SOFIDSE}$ relaxivity that is used for quantification of Ho-MS when utilizing the SOFIDSE method will depend on the diffusion coefficient since $r'_{2\ SOFIDSE}$ is defined as: $r'_{2\ SOFIDSE} = r_2^* - r_2$. However, the possible error introduced by using a fixed value instead of a diffusion dependent r_2 value is small. The total change in r_2 was measured to be 2.6 $s^{-1}.mg^{-1}.ml$ (6.7 – 9.3 $s^{-1}.mg^{-1}.ml$) for a total ADC variation of 2.62 x 10^{-3} mm^2/s (1.24 - 3.86 x 10^{-3} mm^2/s). Taking body temperature (~37°C) as a reference, this was found to result in a total variation of only 2.8% for r_2' over the entire ADC range.

The changes in r_2^* that were found were completely attributed to the temperature dependency of the holmium volume susceptibility, since it was assumed that the FID of Ho-MS containing systems is not influenced by diffusion because it complies with the criteria of static dephasing (53, 85, 92). The resulting decrease in $\Delta\chi$ that was found for increasing temperature is in line with results reported in literature on the temperature dependency of the holmium susceptibility (99), although a slightly stronger dependency would have been expected from this report. This dissimilarity is presumably a result of differences in chemical composition since in the mentioned report the susceptibility of pure holmium

was measured whereas in this work holmium was embedded in poly(L-lactic acid) microspheres. Interestingly, the temperature dependency of r_2^* has so far never been taken into account for quantification of the microsphere biodistribution in previous work (4, 37, 38, 53, 96). In vivo quantification after radioembolization (96), for a body temperature of ~37°C, was performed using a relaxivity r_2^* that was determined from a calibration phantom setup at room temperature. This might have been one of the reasons for the underestimation that was found on average for the total amount of microspheres in the liver, since using a too high relaxivity leads to lower microsphere concentrations.

The comparison with numerical simulations showed that experimental values agreed well with existing theory. Although using a microsphere radius of 15µm for the simulations, which was the mean radius of the used microspheres, showed higher r_2 values than the experiments, the ADC dependency was very similar. Using a 20 µm radius for the microspheres for the simulations led to r_2 values that were similar to experimental values. This radius discrepancy may be a result of the way the microsphere volume was defined in Equation [13]. Defining the mean volume by the mean radius is only valid in case all the microspheres have the same radius. However, the diameter of the microspheres that were used for the experiments ranged between 20 and 50 µm. Therefore, the mean volume actually may have been higher than was determined from the mean diameter. The size distribution of the particles was neither taken into account in defining the parameter k_3 where V_n/V_0 was assumed to be 1.

In conclusion, it was shown that the Ho-MS r_2 relaxivity, as measured by the SOFIDSE method, does depend on the local tissue diffusion coefficient. As a consequence the r_2' parameter that is used to relate the measured signal decay to the local microsphere concentration is dependent on the local diffusion coefficient. By neglecting this dependency, quantification errors can arise but will be limited.

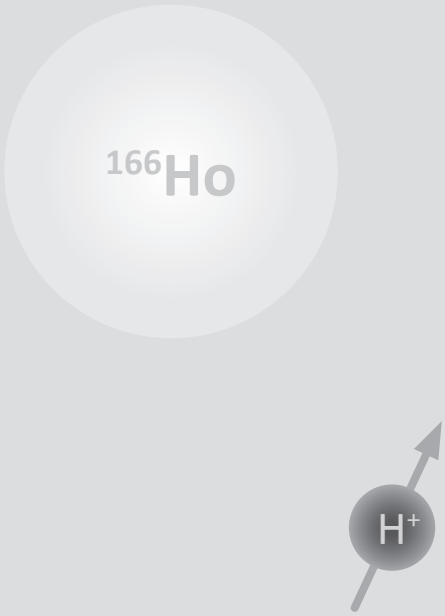
166Ho
H+

Chapter 7

Diffusion weighted imaging after radioembolization

"The purpose of this study was to investigate whether there is an influence of the presence of Ho-MS on diffusion weighted imaging and hence on ADC measurements after radioembolization."

INTRODUCTION

Intra-arterial radioembolization (RE), in which radioactive labeled microspheres are used to selectively irradiate tumors, is an emerging technique for the treatment of unresectable primary or metastatic liver cancer (1, 3, 32, 33). One type of microspheres that has been developed for RE therapy and recently been investigated in a phase I clinical trial (10) is composed of holmium-165 embedded in poly(L-lactic acid) microspheres (Ho-MS) which are neutron activated to holmium-166 MS. Because of the highly paramagnetic nature of holmium, these microspheres are expected to be an ideal device for MRI-guided therapy (31, 37, 38, 96) including MRI-based treatment follow-up for tumor response assessment.

MRI-based response assessment after RE is currently primarily based on conventional anatomical (contrast enhanced) T_1-weighted imaging to measure changes in tumor size according to Response Evaluation Criteria in Solid Tumours v.1.1 (RECIST) (100). This approach however carries an important drawback since early response detection is problematic because anatomical changes may not be seen until three months after therapy (101), and short-term therapy-induced edema surrounding the tumor may be misinterpreted as tumor growth (49). An alternative and promising MRI-based approach to assess tumor response is diffusion weighted imaging (DWI) (97) where the degree of water mobility is characterized by means of the apparent diffusion coefficient (ADC). Several studies, investigating the feasibility of assessing tumor response after ^{90}Y microsphere RE using DWI, showed increasing tumor ADC values shortly after treatment, while no significant changes in tumor size were observed (102–104).

Although this demonstrates the potential of DWI for early tumor response measurements after ^{90}Y RE, it is questioning whether DWI will be able to offer an accurate tumor response measure after ^{166}Ho RE since the paramagnetic nature of Ho-MS may lead to changes in MR signal behavior. The induced susceptibility variations will cause field variations leading to non-linear local gradients that add to the linear diffusion gradients that are applied in DWI (105). Spins will diffuse in both the applied and microsphere induced gradients where the strength of the first will depend on used b-value and the strength of the second will depend on the particle characteristics. Since ADC measurements are based on the application of several b-values, and the ratio between applied and particle induced gradients will differ per b-value, the DW signal behavior may no longer be described by the monoexponential function $S = S_0 \cdot \exp(-b \cdot ADC)$ (106–108).

The purpose of this study was to investigate whether there is an influence of the presence of Ho-MS on DWI and hence on ADC measurements after radioembolization.

MATERIALS AND METHODS

To systematically explore the influence of Ho-MS under ideal laboratory conditions, experiments were conducted in vitro on a phantom setup containing different amounts of Ho-MS. In addition, in vivo measurements were carried out on a patient who was treated with Ho-MS radioembolization for hepatic metastases to investigate the effects in a more realistic scenario.

Phantom preparation

An agarose gel series was prepared in 25 ml plastic tubes (length 65 mm, inner diameter 22 mm). The agarose gel consisted of 2% agarose (weight percentage of agarose per unit distilled water) doped with $MnCl_2.4H_2O$ (30 mg per liter distilled water) in order to shorten the tissue T_1 and thus reduce saturation effects in short-TR sequences. During preparation of the agar gel, non-radioactive Ho-MS (27) were added in concentrations of 0.96, 2.24, 3.03, 4.16 and 4.99 mg/ml. One sample was left blank (0mg/ml). The holmium content of the microspheres was 18.7% by weight and the mean diameter was 30 µm (range 20 – 50 µm). During imaging the samples were placed with their long axes parallel to the main magnetic field.

Patient treatment

A 64-year-old male patient with unresectable, chemorefractory liver metastases originating from colorectal carcinoma was treated with Ho-MS radioembolization within the framework of a phase II efficacy study. The patient signed informed consent and ethical approval for this study was obtained from the institutional review board. The study was performed in accordance with the Declaration of Helsinki and registered with Clinicaltrials.gov, number NCT01612325. The total amount of Ho-MS intended to be delivered to the liver (600mg), plus an extra 10% margin (total amount 660 mg) to correct for loss of microspheres during quality control and administration, was weighed, packed in polyethylene vials (Posthumus Plastics, Beverwijk, the Netherlands) and neutron activated in a nuclear reactor (Delft University of Technology, Delft, the Netherlands). The amount of activity needed for treatment was calculated based on liver weight and an aimed whole-liver absorbed dose of 60 Gy using the medical internal radiation dosimetry (MIRD) method as described for Ho-MS previously (10). The radioembolization procedure was performed according to standard recommendations for ^{90}Y radioembolization (18, 109). The total amount of administered Ho-MS was 610 mg with a total activity of 5548 MBq, as determined by subtraction of measured activity in the microsphere containing vial prior to treatment and measured activity in the administration system after treatment. These

activity measurements were performed using a dose calibrator (VDC-404, Veenstra Instrumenten B.V., Joure, the Netherlands).

MRI acquisition

MR imaging was performed on a 1.5T clinical system (Achieva, Philips Healthcare, Best, the Netherlands), using an 8-channel head receive coil for the phantom experiment and a 16-channel torso receive coil for the patient.

Phantom

For the phantom, a 2D diffusion weighted spin echo sequence was used with b-values of 0, 100, 200, 300 and 400 s/mm^2 and an effective echo time of 48.2 ms. Further scan parameters included: repetition time = 2 s, slice thickness = 15 mm, field of view = 128 x 128 mm^2, matrix = 64^2 and readout bandwidth = 2050 Hz/pixel.

Patient

Diffusion weighted images of the patient were acquired one day prior to and one day after the radioembolization procedure using a DWI protocol that is currently clinically used at the UMC Utrecht for liver imaging. This protocol features a multi slice, respiratory triggered EPI spin echo sequence with b-values of 10, 150 and 1000 s/mm^2 and an effective spin echo time of 70 ms. Other parameters included: repetition time = 1569 ms, slice thickness = 5 mm, field of view = 360 x 293 mm^2, acquisition matrix = 128 x 103, reconstruction matrix = 256^2 and readout bandwidth = 903 Hz/pixel.
To quantify the local concentration of Ho-MS in the liver after radioembolization by means of the microsphere induced T_2^* signal decay, multi-echo gradient echo images were acquired prior to and after treatment. 11 gradient echoes were acquired during breath hold with TE_1 = 2.33 ms and ΔTE = 0.82 ms. Scan parameters included: TR = 360ms, slice thickness = 6 mm, FOV = 384 x 344 mm^2, acquisition matrix = 192 x 151, reconstruction matrix = 192^2, flip angle = 90° and readout bandwidth = 1783 Hz/pixel. Sensitivity encoding (SENSE) with a factor of 2.7 was used for acceleration.

Data processing

All data was processed using home-built software code written in MATLAB (MathWorks, Natick, Massachusetts, USA).

Phantom

Signal intensities were measured from the DW images of the phantom setup for each concentration Ho-MS and b-value utilizing regions of interest (ROI). ADC values were determined by a monoexponential fit ($S(b) = S(0) \cdot \exp[-b \cdot ADC]$) using a least squares fitting

algorithm. A signal to noise (SNR) threshold was used, excluding signal intensities with $S<3\sigma$ to minimize the influence of noise. Here, σ refers to the standard deviation of the signal measured in the blank sample (0 mg/ml Ho-MS). Subsequently, the ADC values as a function of concentration Ho-MS were linearly fitted.

Patient

ADC maps were constructed by a monoexponential fit to the voxel signal intensities of the DW images using a least squares fitting algorithm which weighted all values equally. Here also an SNR threshold of $S<3\sigma$ was used, with σ the standard deviation of the signal measured in a region with homogeneous signal intensity and free from Ho-MS. For each voxel the number of b-values for which the SNR exceeded the threshold and that were used for the ADC fitting procedure was stored. After fitting, the liver was manually segmented using the image contrast of the b = 10 s/mm^2 image.

To quantify the concentration of Ho-MS after radioembolization, multi gradient echo data was processed using the method described in (9). In short, R_2^* maps were constructed from the multi gradient echo dataset by monoexponentially fitting the function $S(TE) = S(0) \cdot \exp[-R_2^* \cdot TE]$ to the intensities of the subsequent gradient echoes using a least squares fitting algorithm. Also for this fitting procedure an SNR threshold of $S<3\sigma$ was used. A baseline R_2^* value was subtracted from the posttherapy R_2^* maps to yield the change in R_2^* (ΔR_2^*) due to the microspheres. This baseline value was determined by the mean R_2^* of the entire liver prior to administration. Subsequently, the concentration Ho-MS was determined from the ΔR_2^* values using the relaxivity r_2^* of the microspheres (103 $s^{-1}.mg^{-1}.ml$ at 1.5 Tesla).

The liver volume was determined by counting the voxels included in the ADC liver segmentation. In addition volumes were determined separately for the cases in which ADC values were determined by three b-values, two b-values or not determined (number of b-values < 2). Mean ADC values in the entire liver were calculated for both the pre- and post-radioembolization situation. Mean ADC values were calculated for two cases: 1) only taking into account values that were determined with three b-values and 2) by also including values that were determined with two b-values.

RESULTS

Phantom setup

Diffusion weighted images of the phantom setup showed increasing signal loss for increasing Ho-MS concentrations even if no diffusion gradient was applied (b = 0) (Figure 1). Signal intensities measured by mean ROI values showed monoexponentially decaying signal as a function of b-value for all samples (Figure 2a) but the decay rate depended on the microsphere concentration. For all b-values, decreased signal intensities were observed for increased concentrations of Ho-MS and a monoexponential relation between signal intensity and concentration Ho-MS was observed for distinct b-values (Figure 2b). ADC values that were determined by a monoexponential fit to the diffusion weighted signal intensities from Figure 2a, displayed a decrease in ADC values for increasing concentrations of Ho-MS (Figure 3). From a linear fit to these values an ADC dependency of $-0.16 \pm 0.02 \times 10^{-3}$ mm^2/s per mg/ml Ho-MS was found for a baseline ADC of 2.09×10^{-3} mm^2/s (blank sample).

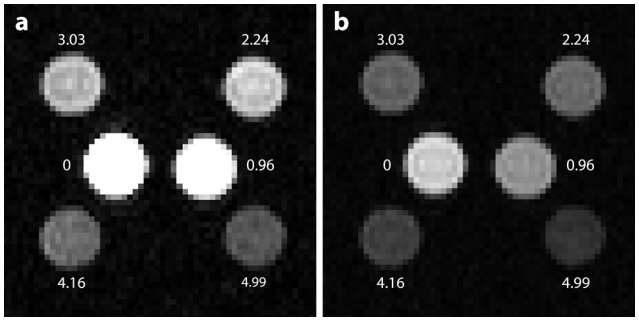

Figure 1 Diffusion weighted images (TE = 48 ms) of the phantom containing a range of Ho-MS concentrations (0, 0.96, 2.24, 3.03, 4.16 and 4.99 mg/ml) for b = 0 s/mm^2 (a) and b = 400 s/mm^2 (b). Signal intensity decreases for increasing microsphere concentrations even if no diffusion sensitizing gradients are applied (b = 0).

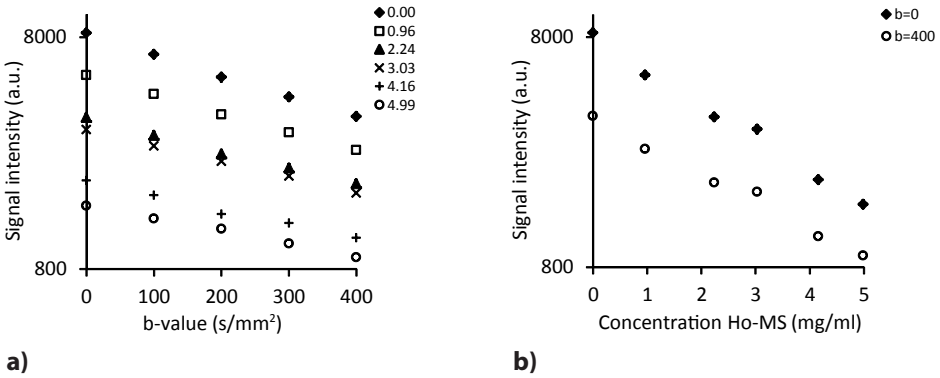

Figure 2 a) Signal intensities measured by regions of interest from the diffusion weighted images of the phantom for various concentrations of Ho-MS plotted on a logarithmic scale. Mono-exponentially decaying signal intensities are observed for increasing b-value. In b) the measured signal intensities are plotted as a function of concentration Ho-MS for distinct b-values on a logarithmic scale. Signal intensities decrease for increasing concentrations of Ho-MS and here also an exponential relation is observed.

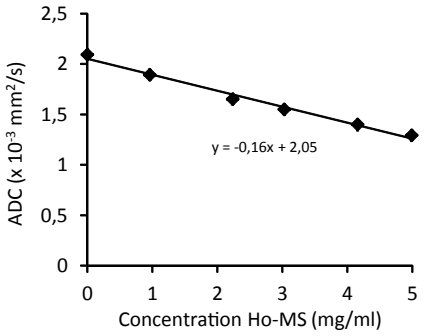

Figure 3 a) ADC values measured for a range of Ho-MS concentrations. Decreasing ADC values are observed for increasing concentrations Ho-MS. A linear fit to these values provided an ADC dependency of -0.16 x 10^{-3} mm^2/s per mg/ml for a baseline ADC of 2.09 x 10^{-3} mm^2/s.

Patient

After Ho-MS radioembolization, diffusion weighted images showed signal loss for all b-values especially in a particular region of the liver (Figure 4) that was identified as tumorous tissue prior to therapy. The same region showed signal loss on T_2^*-weighted gradient echo images especially for later echo times. ADC maps constructed from the DW images showed that in this region ADC values could not be determined at several locations (Figure 5b, black areas) because the number of b-values available for fitting was too low (Figure 5b, bottom row) due to low SNR. Concentration maps, constructed from the multi-echo gradient echo data set showed high concentrations of Ho-MS in these areas. Furthermore it was observed that locations where the ADC could be determined but where only two b-values were available for fitting, displayed increased ADC values.

These locations were primarily found in regions with high microsphere concentrations. Volume measurements of used b-values in the entire liver showed an overall decrease of b-values available for fitting (Table 1). Before RE, the ADC could be characterized in almost the entire liver volume utilizing either 3 b-values (97.2%) or 2 b-values (2.5%). After radioembolization only in 84.5% of the liver volume the ADC was determined by 3 b-values, in 12.9% of the volume by 2 b-values and the ADC could not be characterized in 2.6% of the liver volume. The mean ADC, measured over the entire liver but only including ADC values that were determined by all three b-values, decreased from 0.98 ± 0.37 x 10^{-3} mm^2/s before radioembolization to 0.92 ± 0.41 x 10^{-3} mm^2/s after radioembolization. Including also values that were determined by two b-values showed a minor increase of ADC after RE. The mean Ho-MS concentration in the liver after RE was calculated to be 0.20 ± 0.37 mg/ml based on the quantitative R_2^* data.

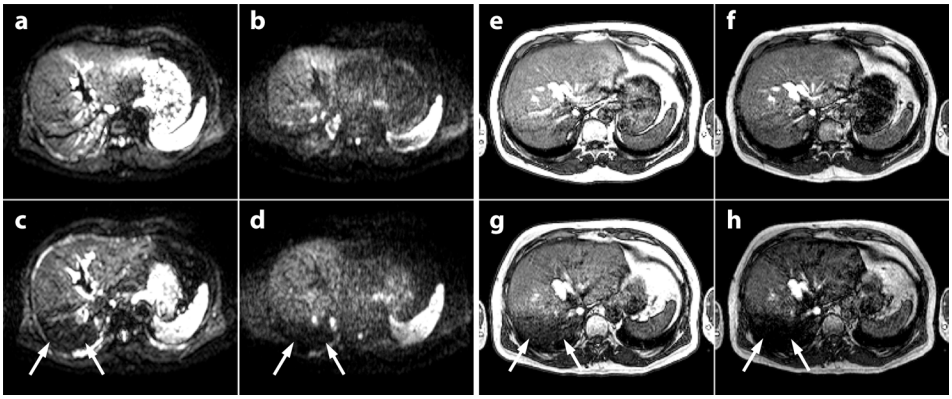

Figure 4 64-year-old man with liver metastases originating from colorectal carcinoma treated with Ho-MS radioembolization. Diffusion weighted images for a b-value of 10 s/mm^2 (a, c) and 1000 s/mm^2 (b, d) and gradient echo images for TE = 2.3 ms (e, g) and 10.5 ms (f, h) prior to (top row) and after (bottom row) Ho-MS radioembolization. Signal reduction was observed for both b-values after RE in regions where gradient echo images also showed large signal loss (white arrows).

Table 1 Measured volumes of available b-values and ADC measurements on a whole liver base before and after RE.

	Before RE	After RE
3 b-values	97.2% LV	84.5% LV
2 b-values	2.5% LV	12.9% LV
< 2 b-values	0.3% LV	2.6 % LV
Mean ADC ± SD (3 b-values)	0.98 ± 0.37	0.92 ± 0.41
Mean ADC ± SD (2 or 3 b-values)	1.02 ± 0.65	1.06 ± 1.03

% LV = % of liver volume
ADC values with their SD given in x 10^{-3} mm^2/sec

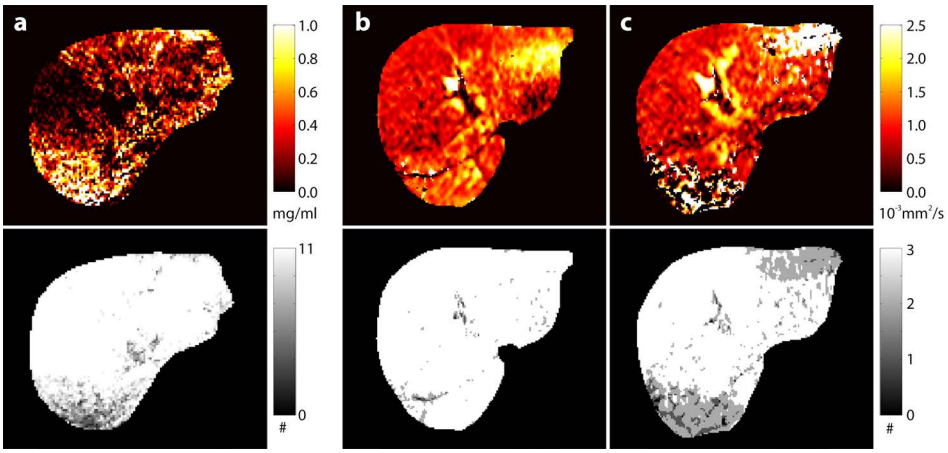

Figure 5 Top row: a) MRI-based Ho-MS concentration map of the liver, b) ADC map of the liver before RE and c) after RE. Bottom row: maps indicating the number of used gradient echoes images for concentration quantification (a) and the number of available b-values for determining ADC values (b, c). Prior to treatment, ADC values could be determined in the entire liver whereas after treatment, calculating ADC values failed in regions where high concentrations of Ho-MS were measured. In addition, in regions where only 2 b-values were available for the fitting procedure, increased ADC values were observed, compared to other regions in the liver and compared to pretreatment values.

DISCUSSION

Although DWI has potential for early tumor response assessment after radioembolization, the results obtained in this work show that tissue ADC characterization after Ho-MS radioembolization is complicated by the paramagnetic nature of the microspheres that are used. Due to the local field gradients that are induced by the microspheres, two problems arise: 1) The presence of microspheres results in reduced spin echo signal for all b-values that are used, including the b (0) image, as was shown for both phantom and in vivo measurements and 2) ADC values decrease as a function of increasing concentrations Ho-MS as was clearly demonstrated by the phantom experiments.

The signal reduction on DW images is a consequence of incomplete signal rephasing at the spin echo time as a result of spins diffusing in the field gradients induced by the microspheres (96). As a result, the SNR may become too low to accurately characterize ADC values as was observed from the in vivo data. Especially in regions that contained high concentrations Ho-MS, according to quantitative R_2^* based data, ADC values could not be determined, or ADC values were only determined by two b-values. Those areas in which only two b-values were available showed increased ADC values which was probably

caused by the influence of perfusion. Whereas high b-value images are assumed to be purely diffusion weighted, low b-value images are partly perfusion weighted (110). Perfusion weighted signal decays faster as a function of b-value than purely diffusion weighted signal, leading to increased ADC values when leaving out the higher b-images which have low SNR.

The ADC dependency on Ho-MS concentration is a consequence of the Ho-MS induced signal reduction that is not equal for each b-value due to the fact that a non-linear gradient distribution induced by the microspheres adds up with the linear diffusion sensitizing gradients (106–108). The total signal loss at the spin echo time therefore depends on the ratio between applied and microspheres induced gradients where the applied gradients become relatively more dominant for higher b-values. As a result, the signal loss due to the presence of microspheres becomes relatively lower for increasing b-values (Figure 2) resulting in decreasing ADC values for increasing concentrations Ho-MS. The relation between ADC and concentration microspheres was found to be approximately linear for the concentration range that was included in the experiments (0 – 5 mg/ml). Such a relation is in line with results that have previously been reported for iron particles (106) and intravascular contrast agent (107). Also for the in vivo case, despite the inability to accurately characterize the ADC in regions with high Ho-MS concentrations, a decrease of ADC was measured in the liver after RE (0.98 prior to versus 0.92 after RE).

To improve ADC characterization after ^{166}Ho RE, first of all the low SNR issue has to be solved. The MR signal level can be easily increased by using more signal averages however at the cost of increasing acquisition time which is not attractive from a clinical point of view. A better solution is to reduce the effective spin echo time but to accomplish this, diffusion gradient duration or spacing should be shortened. However, since b-values are a function of gradient strength, duration and timing only, and the gradient strength is limited by the MRI hardware, this means that the maximum applicable b-value decreases. This may lead to increased perfusion influence on determined ADC values, which has to be taken into account.

Minimizing or correcting for the ADC changes the Ho-MS induce may be more complex. Several attempts have been made to develop a model that accurately describes the influence of protons diffusing in gradients induced by magnetic particles, in order to derive the dependency of the MR signal decay on the properties of the particles (111, 112). Also approaches have been proposed to reduce the influence of the particle induced gradients (113, 114). Whether the proposed models are correct or not (115) it is doubtful that they provide a proper solution to address the problem in the in vivo situation. Since the microspheres are injected in the arterial system of the liver and will lodge in the micro-vasculature and not enter the extra-vascular space, the biodistribution is expected to be rather inhomogeneous. A better strategy may include a correction based on known

local microsphere concentrations and their corresponding ADC reduction as measured from a calibration phantom. The effectiveness and robustness of such a strategy has to be explored in future studies.

In conclusion, it was demonstrated that the presence of Ho-MS causes signal reduction on diffusion weighted images, complicating ADC characterization and leading to decreased ADC values. This has to be taken into account when DW-MRI is used in clinical practice for response prediction in patients who underwent ^{166}Ho-radioembolization.

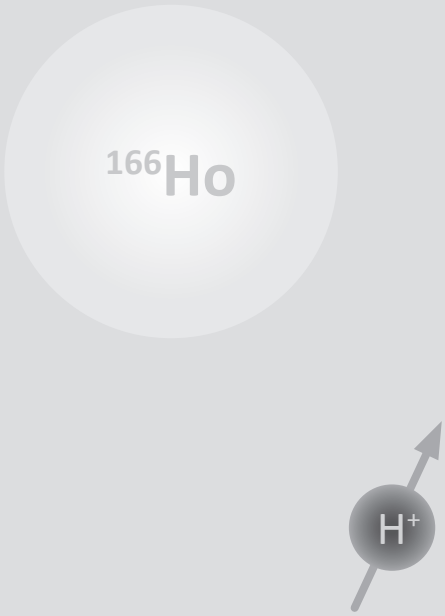
166Ho
H+

Chapter 8

Summary and future perspectives

"The ability of MRI to assess the in vivo microsphere distribution and thus the associated radiation dose distribution was shown, methods to improve MRI-based biodistribution assessment were demonstrated, and the influence of the presence of microspheres on diffusion weighted MR imaging for tumor response assessment was investigated."

To assure safety and to increase efficacy of intra-arterial radioembolization for treatment of liver tumors, imaging is essential. This is not only true for diagnostic purposes to assess tumor involvement and response but also to evaluate the biodistribution of the radioactive microspheres that are used in radioembolization. In this respect, holmium microspheres as therapeutic particles and MRI as imaging platform form a promising combination. While holmium microspheres possess attractive radioembolization characteristics, MRI is a non-invasive imaging modality that offers soft tissue contrast, provides functional imaging and enables microsphere biodistribution measurements. In this thesis the utility of MRI in holmium radioembolization was explored. The ability of MRI to assess the in vivo microsphere distribution and thus the associated radiation dose distribution was shown, methods to improve MRI-based biodistribution assessment were demonstrated, and the influence of the presence of microspheres on diffusion weighted MR imaging for tumor response assessment was investigated. A summary of this work is given below per chapter.

Chapter 2. The feasibility of MRI-based assessment of the intrahepatic Ho-MS biodistribution after radioembolization was investigated in patients that were included in a phase I clinical trial. Fifteen patients were treated with radioactive Ho-MS according to a dose escalation protocol, delivering 484 mg of microspheres on average (range 408- 593 mg) to the liver with an aimed whole liver dose of 20, 40, 60 or 80 Gy. Multi gradient echo MR images were acquired on a 1.5 T whole body MRI system prior to and after radioembolization. R_2^* maps were constructed from these series of gradient echo images using a mono-exponential fitting algorithm. These R_2^* maps visualized the deposition of Ho-MS with great detail. To quantify the amount of microspheres, the induced change in R_2^* was determined by subtracting the mean R_2^* value of the whole liver pre-treatment from the post-treatment R_2^* maps and divided by the r_2^* relaxivity of Ho-MS as measured from a calibration phantom setup. The total amount that was detected in the liver, 431 mg on average (range 236 – 666 mg), was comparable to the delivered amount (89 ± 19% on average, correlation coefficient $r = 0.7$; $P < 0.01$). The voxelwise amounts were converted into units of activity by multiplication with the specific activity of the microspheres. Single photon emission computed tomography (SPECT) images, acquired for comparison and reconstructed to quantitative Ho-MS activity maps, showed good visual resemblance to the MRI-based activity maps. For both MRI and SPECT, absorbed dose maps were generated by convolution of the activity maps with a ^{166}Ho 3D dose point kernel calculated using Monte Carlo code and mean absorbed radiation doses were calculated. A good correlation was found between the whole liver mean absorbed radiation dose as assessed by MRI and SPECT (correlation coefficient $r = 0.93$; $P < 0.001$).

Chapter 3. The conventional R_2^* fitting method as used in chapter 2 may fail because of fast signal decay due to high local Ho-MS concentrations. Therefore, a post-processing method, S_0-fitting, was developed to successfully estimate R_2^* in that case. S_0-fitting incorporates the estimated initial amplitude of the free induction decay (FID) curve, S_0, of neighboring voxels into the fitting procedure for voxels for which the conventional algorithm failed. The method was applied to a conventional multi gradient echo (MGE) dataset of a phantom setup containing known concentrations of Ho-MS (range 0 – 15 mg/ml) and a dataset of an ex vivo rabbit liver to which Ho-MS were administered. Applying S_0-fitting provided a best estimate for R_2^* up to a value of about 2300 s^{-1} (which corresponds to a Ho-MS concentration of 11.5 mg/ml at 3T) compared with a maximum value of about 1000 s^{-1} (which corresponds to a Ho-MS concentration of 5 mg/ml at 3T) that could be characterized using conventional fitting. The S_0-fitting method was validated by comparing resulting R_2^* values and their corresponding r_2^* relaxivity with results obtained utilizing quantitative ultrashort TE imaging (qUTE), an acquisition method for sampling rapidly decaying signals. S_0-fitting provided a Ho-MS relaxivity of 206 ± 12 $s^{-1}.mg^{-1}.ml$ whereas qUTE data provided a relaxivity of 205 ± 16 $s^{-1}.mg^{-1}.ml$ over the same concentration range. The detected amount of Ho-MS in the ex vivo liver, as derived from the R_2^* measurements was 7.21mg, 8.20mg, and 8.26mg for respectively conventionally fitted MGE data, S_0-fitted MGE data, and qUTE data. This demonstrates that S_0-fitting increases the accuracy of Ho-MS quantification, taking qUTE as the reference standard.

Chapter 4. The potential of MRI for accurate assessment of the three-dimensional ^{166}Ho activity distribution to estimate radiation-absorbed dose distributions in liver radioembolization was investigated. MRI, computed tomography (CT), and SPECT experiments were conducted on an anthropomorphic phantom with tumor-simulating gel samples and on an excised human tumor-bearing liver, both containing known amounts of Ho-MS. Three-dimensional radiation-absorbed dose distributions were estimated by convolving the ^{166}Ho activity distribution, derived from quantitative MRI data, with a ^{166}Ho dose point kernel generated by Monte Carlo N-Particle transport code and from Medical Internal Radiation Dose Pamphlet 17. MRI-based radiation-absorbed dose distributions were qualitatively compared with CT and autoradiography images and quantitatively compared with SPECT-based dose distributions. Both MRI- and SPECT-based activity estimations were validated against dose calibrator measurements. The phantom data showed that MRI enables accurate assessment of local Ho-MS mass and activity distributions, as supported by a linear regression coefficient of 1.05 (R^2 = 0.99), relating local MRI-based mass and activity calculations to reference values obtained with the dose calibrator. Estimated MRI-based radiation-absorbed dose distributions of Ho-MS in the ex vivo human liver visually showed high resemblance with SPECT-based dose distributions. Quantitative analysis revealed that the differences in local and total amounts of Ho-MS estimated by MRI, SPECT,

and the dose calibrator were within 10%. Excellent agreement was observed between MRI- and SPECT-based dose-volume histograms.

Chapter 5. A method was proposed, S_0 estimation of the free induction decay combined with a single spin echo measurement (SOFIDSE), to simultaneously measure R_2^* and R_2 within a short acquisition time. SOFIDSE estimates R_2^* and the signal at time point 0, S_0, from a multi gradient echo readout of the free induction decay and subsequently estimates R_2 utilizing S_0 and a single spin echo readout. By subtraction of R_2^* and R_2, the reversible Ho-MS induced signal decay parameter R_2' is obtained that is independent of the R_2 value of the tissue in which the microspheres reside. In this respect SOFIDSE provides a quantification strategy that is insensitive to changes in tissue R_2 that may occur following therapy and basically eliminates the need for pretreatment image acquisition. The method was evaluated by comparing SOFIDSE R_2 values with values obtained from shifted spin echo (SSE) measurements, both on a phantom setup containing known amounts of holmium microspheres and in vivo on a healthy volunteer. SOFIDSE R_2 values showed on average a small overestimation (5%), independent of the concentration microspheres, compared with SSE. R_2' values determined by a subtraction of R_2^* and either SOFIDSE R_2 or SSE R_2 showed a high correlation (correlation coefficient $r = 1$; $P = 9 \cdot 10^{-11}$). The holmium microsphere induced reversible R_2' values that were obtained by SOFIDSE were, in contrast to the R_2^* values, not sensitive to the R_2 value of the tissue in which they reside, as was demonstrated on a phantom setup containing a range of baseline R_2 values and a fixed Ho-MS concentration.

Chapter 6. The dependency of the spin echo relaxivity parameter r_2 and hence of the SOFIDSE relaxivity parameter $r_{2\,SOFIDSE}'$ on diffusion were investigated. SOFIDSE experiments were performed on a phantom setup, containing a known Ho-MS concentration range, of which the diffusion coefficient was changed by varying the temperature. Diffusion weighted images were acquired in order to measure the degree of diffusion by means of the apparent diffusion coefficient (ADC). Ho-MS r_2 and r_2^* relaxivity values were determined from a linear fit to the concentration dependent ΔR_2 and ΔR_2^* that were obtained from the SOFIDSE data for the range of measured ADC values. An increase of 6.7 $s^{-1}.mg^{-1}.ml$ to 9.3 $s^{-1}.mg^{-1}.ml$ was found for r_2 over an ADC range of 1.24 x 10^{-3} mm^2/s to 3.86 x 10^{-3} mm^2/s. Changes in r_2^* that were found were attributed to the temperature dependency of the holmium susceptibility and processed as such. Over an estimated temperature range of 1.1°C to 46.3°C, r_2^* was found to decrease from 108.3 $s^{-1}.mg^{-1}.ml$ to 98.3 $s^{-1}.mg^{-1}.ml$. A comparison of the obtained results with numerical simulations, based on an analytical model for NMR signal behavior in heterogeneous systems subjected to diffusion, showed good agreement between experiments and theory. Taking body temperature as a reference, the relaxivity parameter $r_{2\,SOFIDSE}'$ obtained from a subtraction of r_2^* and r_2 showed a variation of only 2.8% over the entire ADC range that was investigated.

Chapter 7. The influence of the presence of Ho-MS on diffusion weighted imaging (DWI) after radioembolization and hence on apparent diffusion coefficient (ADC) characterization was investigated. DWI was performed on a phantom setup containing known concentrations of Ho-MS. Signal intensities measured from the DW images for each concentration and applied b-value showed reduced signal that depended on microsphere concentration and applied b-value. ADC values, obtained from a mono-exponential fit to the DW signal intensities, showed a decrease of -0.16 x 10^{-3} mm^2/s per mg/ml Ho-MS for a baseline ADC of 2.09 x 10^{-3} mm^2/s. DWI was also performed in vivo on a patient who underwent Ho-MS radioembolization for treatment of hepatic metastases. ADC values were determined from DW images that were acquired prior to and after administration of the microspheres. The resulting ADC maps were compared to quantitative R_2^* based Ho-MS biodistribution maps. Signal reduction was observed on post-treatment DW images in regions with high Ho-MS concentrations. The low signal-to-noise ratio in these areas resulted in inaccurate or no ADC characterization since the number of data points available for fitting decreased.

The work presented in this thesis and summarized above demonstrates the significant role MRI can play in ^{166}Ho radioembolization. R_2^* based MRI data provides a quantitative measure of the intrahepatic microsphere biodistribution with great detail, thereby enabling radiation absorbed dose estimation on a tumor level. Utilizing these dose measurements, the safety and efficacy of the radioembolization procedure can be evaluated, since it can be assessed whether or not absorbed radiation doses exceeded tolerance levels for healthy liver tissue and whether tumors received a dose which can be expected to be lethal to tumor tissue. This information can subsequently be used to determine whether treatment targets have been met or secondary treatment will be necessary and secure. A strong feature of MRI-based dose measurement is that the required acquisition time is relatively short, as compared with the alternative SPECT, which gives opportunities for monitoring the microsphere biodistribution during the administration procedure. Whole-liver real-time microsphere tracking during injection may not be realistic yet, considering the MR acquisition times mentioned in this work, however, a scenario in which the total dose to be administered is spread out over several injections, each followed by a biodistribution measurement, is feasible. Based on intermediate measurements, administration can be continued or not, depending on whether safety margins for the healthy liver tissue have been reached or lethal doses on the tumor have been achieved. Instead of a whole liver approach, radioembolization under MRI-guidance will also offer opportunities for selective administration of microspheres to more specific liver areas or tumors, particularly since MRI acquisition times scale with the size of the area to be imaged. Such an approach may be much more safe and effective, especially for patients with a small

number of liver tumors to be treated, since it will lower the overall radiation dose on healthy liver tissue while the tumor-received dose will increase.
With regard to MRI-based therapy response assessment, the use of ^{166}Ho microspheres introduces some challenges. Especially when utilizing diffusion weighted imaging for relating the local apparent diffusion coefficient to tissue characteristics, two problems arise. First, the signal reduction induced by the microspheres, and the associated lower signal-to-noise ratio, on diffusion weighted images hampers the accuracy of ADC characterization. Second, the ADC becomes dependent on the local concentration of microspheres. The latter effect may be accounted for by a correction based on the measured concentration of microspheres and the known relation between concentration and ADC value. Counteracting the SNR reduction will probably be less straightforward since in MRI an increase in SNR is usually paid for by an increase in acquisition time. Using higher main magnetic field strengths, like 3T or 7T instead of 1.5T, will increase the initially available MR signal but will also lead to stronger microsphere-induced dephasing effects. These factors have to be taken into account in finding a proper solution. The reduction in signal intensity should also be taken into account when therapy response evaluation is based on conventional T_1-weighted or T_2-weighted images. Although it may not be expected that tissue structures will appear deformed, the tissue contrast will differ between pre- and posttherapy images when microspheres are present. Radiologists should be aware of this effect to prevent misinterpretation of these images.

In conclusion, in this thesis it is shown that the combination of magnetic resonance imaging and ^{166}Ho radioembolization has the potential to increase safety and efficacy of radioembolization and opens the way to image-guided therapy.

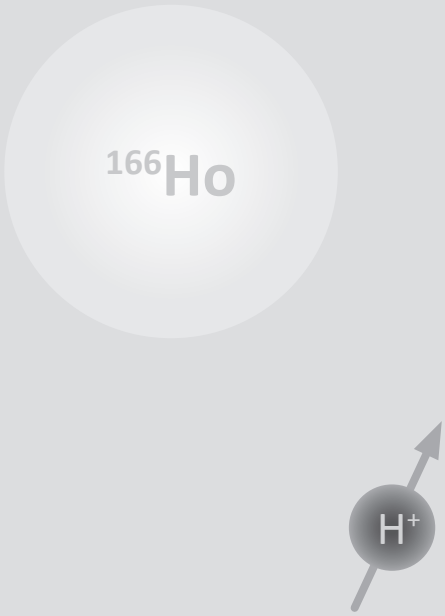
166Ho
H+

Bibliography

"83. Hahn EL. Spin echoes. Phys Rev 1950; 80:580-594

84. Ma J, Wehrli FW. Method for image-based measurement of the reversible and irreversible contribution to the transverse-relaxation rate. J Magn Reson Ser B 1996; 111:61-69"

1. Salem R, Thurston KG. Radioembolization with Yttrium-90 Microspheres: A state-of-the-art brachytherapy treatment for primary and secondary liver malignancies. J Vasc Interv Radiol 2006; 17:1571-1594

2. Kennedy AS, McNeillie P, Dezarn WA, Nutting C, Sangro B, Wertman D, Garafalo M, Liu D, Coldwell D, Savin M, Jakobs T, Rose S, Warner R, Carter D, Sapareto S, Nag S, Gulec S, Calkins A, Gates VL, Salem R. Treatment parameters and outcome in 680 treatments of internal radiation with resin 90Y-microspheres for unresectable hepatic tumors. Int J Radiat Oncol Biol Phys 2009; 74:1494-500

3. Vente MAD, Wondergem M, van der Tweel I, van den Bosch MA, Zonnenberg BA, Lam MG, van het Schip AD, Nijsen JF. Yttrium-90 microsphere radioembolization for the treatment of liver malignancies: a structured meta-analysis. Eur Radiol 2009; 19:951-959

4. Hendlisz A, Van den Eynde M, Peeters M, Maleux G, Lambert B, Vannoote J, De Keukeleire K, Verslype C, Defreyne L, van Cutsem E, Delatte P, Delaunoit T, Personeni N, Paesmans M, van Laethem JL, Flamen P. Phase III trial comparing protracted intravenous fluorouacil infusion alone or with yttrium-90 resin microspheres radioembolization for liver-limited metastatic colorectal cancer refractory to standard chemotherapy. J Clin Oncol 2012; 28:3687-94

5. Bierman HR, Byron RL Jr, Kelley KH, Grady A. Studies on the blood supply of tumors in man. III. Vascular patterns of the liver by hepatic arteriography in vivo. J Natl Cancer Int 1951; 12:107-31

6. Ackerman NB, Lien WM, Kondi ES, Silverman NA. The blood supply of experimental liver metastases. I. The distribution of hepatic artery and portal vein blood to “small” and “large” tumours. Surgery 1969; 66:1076-1072

7. Burton MA. Selective internal radiation therapy: distribution of radiation in the liver. Eur J Cancer Clin Oncol 1989; 25:1486-1491

8. Bult W, Vente MAD, Zonnenberg BA, van het Schip AD, Nijsen JF. Microsphere radioembolization of liver malignancies: current developments. Q J Nucl Med Mol Imaging 2009; 53:325-335

9. Liepe K, Brogsitter C, Leonhard J, Wunderlich G, Hliscs R, Pinkert J, Folprecht G, Kotzerke J. Feasibility of high activity rhenium-188-microsphere in hepatic radioembolization. Jpn J Clin Oncol 2007; 37:942-950

10. Smits ML, Nijsen JF, van den Bosch MA, Lam MG, Vente MA, Mali WP, van het Schip AD, Zonnenberg BA. Holmium-166 radioembolisation: results of a phase 1, dose escalation study in patients with unresectable, chemorefractory liver me-

tastases – the HEPAR trial. Lancet Oncol 2012; 13:1025-1034

11. Murthy R, Numez R, Szklaruk J, Erwin W, Madoff DC, Gupta S, Ahrar K, Wallace MJ, Cohen A, Coldwell DM, Kennedy AS, Hicks ME. Yttrium-90 microsphere therapy for hepatic malignancy: devices, indications, technical considerations, and potential complications. Radiographics 2005; 25:S41-S55

12. Murthy R, Brown DB, Salem R, Meranze SG, Coldwell DM, Krishnan S, Nunez R, Habbu A, Liu D, Ross W, Cohen AM, Censullo M. Gastrointestinal complications associated with hepatic arterial Yttrium-90 microsphere therapy. J Vasc Interv Radiol 2007; 18:533-561

13. Carretero C, Munoz-Navas M, Betes M, Angos R, Subtil JC, Fernandez-Urien I, De la Riva S, Sola J, Bilbao JI, de Luis E, Sangro B. Gastroduodenal injury after radioembolization of hepatic tumors. Am J Gastroenterol 2007; 102:1216-1220

14. Leung TW, Lau WY, Ho SK, Ward SC, Chow JH, Chan MS, Metreweli C, Johnson PJ, Li AK. Radiation pneumonitis after selective internal radiation treatment with intraarterial 90Yttrium-microspheres for inoperable hepatic tumors. Int J Radiat Oncol Biol Phys 1995; 33:919-924

15. Salem R, Parikh P, Atassi B, Lewandowski RJ, Ryu RK, Sato KT, Gates VL, Ibrahim S, Mulcahy MF, Kulik L, Liu DM, Riaz A, Omary RA, Kennedy AS. Incidence of radiation pneumonitis after hepatic intra-arterial radiotherapy with yttrium-90 microspheres assuming uniform lung distribution. Am J Clin Oncol 2008; 31:431-438

16. Lewandowski RJ, Sato KT, Atassi B, Ryu RK, Nemcek AA Jr, Kulik L, Geschwind JF, Murthy R, Rilling W, Liu D, Bester L, Bilbao JI, Kennedy AS, Omary RA, Salem R. Radioembolization with 90Y microspheres: angiographic and technical considerations. Cardiovasc Interv Radiol 2007; 30:571-592

17. Salem R, Thurston KG. Radioembolization with 90yttrium microspheres: a state-of-the-art brachytherapy treatment for primary and secondary liver malignancies. Part 2: special topics. J Vasc Interv Radiol 2006; 17:1425-1439

18. Kennedy A, Nag S, Salem R, Murthy R, McEwan AJ, Nutting C, Benson A 3rd, Espat J, Bilbao JI, Sharma RA, Thomas JP, Coldwell D. Recommendation for radioembolization of hepatic malignancies using yttrium-90 microsphere brachytherapy: a consensus panel report from the radioembolization brachytherapy oncology consortium. Int J Radiat Oncol Biol Phys 2007; 68:13-23

19. Leung WT, Lau WY, Ho SK, Chan M, Leung NW, Lin J, Metreweli C, Johnson PJ, Li AK. Measuring lung shunting in hepatocellular carcinoma with intrahepatic-arte-

rial technetium 99m macroaggregated albumin. J Nucl Med 1994; 35:70-73

20. Fabbri C, Sarti G, Cremonesi M, Ferrari M, Di Dia A, Agostini M, Botta F, Paganelli G. Quantitative analysis of 90Y Bremsstrahlung SPECT-CT images for application to 3D patient-specific dosimetry. Cancer Biother Radiopharm 2009; 24:145-154

21. Minarik D, Sjögreen-Gleisner K, Ljungberg M. Evaluation of quantitative 90Y SPECT based on experimental phantom studies. Phys Med Biol 2008; 53:5689-5703

22. Minarik D, Sjögreen-Gleisner K, Linden O, Wingardh K, Tennvall J, Strand SE, Ljungberg M. 90Y Bremsstrahlung imaging for absorbed-dose assessment in high-dose radioimmunotherapy. J Nucl Med 2010; 51:1974-1978

23. Elschot M, Nijsen JFW, Dam AJ, de Jong HWAM. Quantitative evaluation of scintillation camera imaging characteristics of isotopes used in liver radioembolization. PLoS ONE 2011; 6:e26174

24. Lhommel R, van Elmbt L, Goffette P, van den Eynde M, Jamar F, Pauwels S, Walrand S. Feasibility of 90Y TOF PET-based dosimetry in liver metastasis therapy using SIR-Spheres. Eur J Nucl Med Mol Imaging 2010; 37:1654-1662

25. Gates VL, Esmail AAH, Marshall K, Spies S, Salem R. Internal pair production of 90Y permits hepatic localization of microspheres using routine PET: Proof of concept. J Nucl Med 2011; 52:72-76

26. Mumper RJ, Ryo UY, Jay M. Neutron-activated holmium-166-poly (L-lactic acid) microspheres: a potential agent for the internal radiation therapy of hepatic tuomors. J Nucl Med 1991; 32:2139-2143

27. Nijsen JFW, Zonnenberg BA, Woittiez JRW, Rook DW, Swildens-van Woudenberg IA, van Rijk PP, van het Schip AD. Holmium-166 poly lactic acid microspheres applicable for intra-arterial radionuclide therapy of hepatic malignancies: effects of preperation and neutron activation techniques. Eur J Nucl Med 1999; 26:699-704

28. de Wit TC, Xiao J, Nijsen JFW, van het Schip AD, Staelens SG, van Rijk PP, Beekman FJ. Hybrid scatter correction applied to quantitative holmium-166 SPECT. Phys Med Biol 2006; 51:4773-4787

29. Seevinck PR, Seppenwoolde JH, de Wit TC, Nijsen JF, Beekman FJ, van het Schip AD, Bakker CJ. Factors affecting the sensitivity and detection limits of MRI, CT, and SPECT for multimodal diagnostic and therapeutic agents. Anticancer Agents Med Chem 2007; 7:317-334

30. Bartels LW, Bakker CJG. Endovascular interventional magnetic resonance imaging. Phys Med Biol 2003; 48:R37-R64

31. Seppenwoolde JH, Bartels LW, van der Weide R, Nijsen JF, van het Schip AD, Bakker CJ. Fully MR-guided hepatic artery catheterization for selective drug delivery: a feasibility study in pigs. J Magn Reson Imaging 2006; 23:123-129

32. Kennedy AS, Coldwell D, Nutting C, Murthy R, Wertman DE Jr, Loehr SP, Overton C, Meranze S, Niedzwiecki J, Sailer S. Resin 90Y-microsphere brachytherapy for unresectable colorectal liver metastases: modern USA experience. Int J Radiat Oncol Biol Phys 2006; 65:412–425

33. Vente MAD, Hobbelink MGG, van het Schip AD, Zonnenberg BA, Nijsen JF. Radionuclide liver cancer therapies: from concept to current clinical status. Anticancer Agents Med Chem 2007; 7:441–459

34. Gulec SA, Fong Y. Yttrium 90 microsphere selective internal radiation treatment of hepatic colorectal metastases. Arch Surg 2007; 142:675–682

35. Gupta T, Virmani S, Neidt TM, Szolc-Kowalska B, Sato KT, Ryu RK, Lewandowski RJ, Gates VL, Woloschak GE, Salem R, Omary RA, Larson AC. MR Tracking of iron-labeled glass radioembolization microspheres during transcatheter delivery to Rabbit VX2 liver tumors: feasibility study. Radiol 2008; 249:845–854

36. Nijsen JFW, van Steenbergen MJ, Kooijman H, Talsma H, Kroon-Batenburg LM, van de Weert M, van Rijk PP, de Witte A, van het Schip AD, Hennink WE. Characterization of poly(L-lactic acid) microspheres loaded with holmium acetylacetonate. Biomaterials 2001; 22:3073–3081

37. Nijsen JFW, Seppenwoolde JH, Havenith T, Bos C, Bakker CJ, van het Schip AD. Liver tumors: MR imaging of radioactive holmium microspheres — phantom and rabbit study. Radiol 2004; 231:491–499

38. Seppenwoolde JH, Nijsen JFW, Bartels LW, Zielhuis SW, van het Schip AD, Bakker CJ. Internal radiation therapy of liver tumors: qualitative and quantitative magnetic resonance imaging of the biodistribution of holmium-loaded microspheres in animal models. Magn Reson Med 2005; 53:76–84

39. Vente MAD, Nijsen JFW, de Wit TC, Seppenwoolde JH, Krijger GC, Seevinck PR, Huisman A, Zonnenberg BA, van den Ingh TS, van het Schip AD. Clinical effects of transcatheter hepatic arterial embolization with holmium-166 poly(L-lactic acid) microspheres in healthy pigs. Eur J Nucl Med Mol Imaging 2008; 7:1259–1271

40. Seevinck PR, van de Maat GH, de Wit TC, Vente MA, Nijsen JF, Bakker CJ. Magnet-

ic resonance imaging-based radiation-absorbed dose estimation of 166-Ho microspheres in liver radioembolization. Int J Rad Oncol Biol Phys 2012; 83:e437–e444

41. Vente MA, Nijsen JF, de Roos R, van Steenbergen MJ, Kaaijk CN, Koster-Ammerlaan MJ, de Leege PF, Hennink WE, van het Schip AD, Krijger GC. Neutron activation of holmium poly(L-lactic acid) microspheres for hepatic arterial radio-embolization: a validation study. Biomed Microdevices 2009; 11:763–772

42. Smits ML, Nijsen JF, van den Bosch MA, Lam MG, Vente MA, Huijbregts JE, van het Schip AD, Elschot M, Bult W, de Jong HW, Meulenhoff PC, Zonnenberg BA. Holmium-166 radioembolization for the treatment of patients with liver metastases: design of the phase I HEPAR trial. J Exp Clin Cancer Res 2010; 29:70

43. Coldwell D, Sangro B, Wasan H, Salem R, Kennedy A. General selection criteria of patients for radioembolization of liver tumors: an international working group report. Am J Clin Oncol 2011; 34:337–41

44. Brown MA, Carden JA, Coleman RE, McKenney R Jr, Spicer LD. Magnetic field effects on surgical ligation clips. Magn Reson Imag 1987; 5:443–453

45. Czervionke LF, Daniels DL, Wehrli FW, Mark LP, Hendrix LE, Strandt JA, Williams AL, Haughton VM. Magnetic susceptibility artifacts in gradient-recalled echo MR imaging. Am J Neuroradiol 1988; 9:1149–1155

46. Port JD, Pomper MG. Quantification and minimization of magnetic susceptibility artifacts on GRE images. J Comput Assist Tomogr 2000; 24:958–964

47. Bolch WE, Bouchet LG, Robertson JS, Wessels BW, Siegel JA, Howell RW, Erdi AK, Aydogan B, Costes S, Watson EE, Brill AB, Charkes ND, Fisher DR, Hays MT, Thomas SR. MIRD pamphlet no. 17: the dosimetry of nonuniform activity distributions—radionuclide S values at the voxel level. Medical Internal Radiation Dose Committee. J Nucl Med 1999; 40:11S–36S

48. International Commission on Radiation Units and Measurements. Tissue Substitutes in Radiation Dosimetry and Measurement, 44th edn. Bethesda, MD: 1989

49. Kamel IR, Bluemke DA. Imaging evaluation of hepatocellular carcinoma. J Vasc Interv Radiol 2002; 13:S173–S183

50. Rummeny E, Weissleder R, Stark DD, Saini S, Compton CC, Bennett W, Hahn PF, Wittenberg J, Malt RA, Ferrucci JT. Primary liver tumours: diagnosis by MR imaging. Am J Roentgenol 1989; 152:63–72

51. Vente MA, Zonnenberg BA, Nijsen JF. Microspheres for radioembolization of liver malignancies. Expert Rev Med Devices 2010; 7:581–583

52. Seevinck PR, Bos C, Bakker CJ. Ultrashort T_2^* relaxometry using conventional multiple gradient echo sampling with S0 fitting: validation with quantitative UTE (QUTE) imaging. Proc Intl Soc Mag Reson Med 2008:1419

53. Seevinck PR, Seppenwoolde JH, Zwanenburg JJ, Nijsen JF, Bakker CJ. FID sampling superior to spin-echo sampling for T_2^*-based quantification of holmium-loaded microspheres: theory and experiment. Magn Reson Med 2008; 60:1466–1476

54. van de Maat GH, Elschot M, Seevinck PR, de Leeuw H, de Jong H, Smits M, van den Bosch M, Lam M, Zonnenberg B, van het Schip AD, Nijsen JF, Bakker CJ. Detection and quantification of holmium-166 loaded microspheres in patients with liver metastases: initial experience within the framework of a phase I study. Proc Intl Soc Mag Reson Med 2011:201

55. Ghugre NR, Enriquez CM, Coates TD, Nelson MD Jr, Wood JC. Improved R_2^* measurements in myocardial iron overload. J Magn Reson Imaging 2006; 23:9–16

56. Song R, Song HK. Echo-spacing optimization for the simultaneous measurement of reversible (R_2') and irreversible (R_2) transverse relaxation rates. Magn Reson Imaging 2007; 25:63–68

57. Kuhlpeter R, Dahnke H, Matuszewski L, Persigehl T, von Wallbrunn A, Allkemper T, Heindel WL, Schaeffter T, Bremer C. R_2 and R_2^* mapping for sensing cell-bound superparamagnetic nanoparticles: in vitro and murine in vivo testing. Radiology 2007; 245:449–457

58. Maris TG, Papakonstantinou O, Chatzimanoli V, Papadakis A, Pagonidis K, Papanikolaou N, Karantanas A, Gourtsoyiannis N. Myocardial and liver iron status using a fast T_2^* quantitative MRI (T_2^*qMRI) technique. Magn Reson Med 2007; 57:742–753

59. Robson MD, Gatehouse PD, Bydder M, Bydder GM. Magnetic resonance: an introduction to ultrashort TE (UTE) imaging. J Comput Assist Tomogr 2003; 27:825–846

60. Robson MD, Benjamin M, Gishen P, Bydder GM. Magnetic resonance imaging of the Achilles tendon using ultrashort TE (UTE) pulse sequences. Clin Radiol 2004; 59:727–735

61. Du J, Takahashi AM, Chung CB. Ultrashort TE spectroscopic imaging (UTESI): application to the imaging of short T2 relaxation tissues in the musculoskeletal sys-

tem. J Magn Reson Imaging 2009; 29:412–421

62. Du J, Hamilton G, Takahashi A, Bydder M, Chung CB. Ultrashort echo time spectroscopic imaging (UTESI) of cortical bone. Magn Reson Med 2007; 58:1001–1009

63. Williams A, Qian Y, Bear D, Chu CR. Assessing degeneration of human articular cartilage with ultra-short echo time (UTE) T2* mapping. Osteoarthritis Cartilage 2010; 18:539–546

64. Wolfram Mathworld 2010
http://mathworld.wolfram.com/LeastSquaresFittingExponential.html

65. Henkelman RM. Measurement of signal intensities in the presence of noise in MR images. Med Phys 1985; 12:232–233

66. Gudbjartsson H, Patz S. The Rician distribution of noisy MRI data. Magn Reson Med 1995; 34:910–914

67. Josan S, Pauly JM, Daniel BL, Pauly KB. Double half RF pulses for reduced sensitivity to eddy currents in UTE Imaging. Magn Reson Med 2009; 61:1083–1089

68. Liu W, Dahnke H, Rahmer J, Jordan EK, Frank JA. Ultrashort T_2^* relaxometry for quantification of highly concentrated superparamagnetic iron oxide (SPIO) nanoparticle labeled cells. Magn Reson Med 2009; 61:761–766

69. Salem R, Thurston KG. Radioembolization with yttrium-90 microspheres: a state-of-the-art brachytherapy treatment for primary and secondary liver malignancies: Part 3: comprehensive literature review and future direction. J Vasc Interv Radiol 2006; 17:1571-1593

70. Riaz A, Gates VL, Atassie B, Lewandowski RJ, Mulcahy MF, Ryu RK, Sato KT, Baker T, Kulik L, Gupta R, Abecassis M, Benson AB 3rd, Omary R, Millender L, Kennedy A, Salem R. Radiation segmentectomy: a novel approach to increase safety and efficacy of radioembolization. Int J Radiat Oncol Biol Phys 2011; 79:163-171

71. Kennedy AS, Nutting C, Coldwell D, Gaiser J, Drachenberg C. Pathologic response and microdosimetry of (90)Y microspheres in man: review of four explanted whole livers. Int J Radiat Oncol Biol Phys 2004; 60:1552-1563

72. Ho S, Lau WY, Leung TW, Chan M, Chan KW, Lee WY, Johnson PJ, Li AK. Tumour-to-normal uptake ratio of 90Y microspheres in hepatic cancer assessed with 99Tcm macroaggregated albumin. Br J Radiol 1997; 70:823-828

73. Vente MAD, de Wit TC, van den Bosch MA, Bult W, Seevinck PR, Zonnenberg BA, de Jong HW, Krijger GC, Bakker CJ, van het Schip AD, Nijsen JF. Holmium-166 poly(L-lactic acid) microsphere radioembolisation of the liver: Technical aspects studied in a large animal model. Eur Radiol 2010; 20:862-869

74. Knesaurek K, Machac J, Muzinic M, DaCosta M, Zhang Z, Heiba S. Quantitative comparison of yttrium-90 (90Y)-microspheres and technetium-99m (99mTc)-macroaggregated albumin SPECT images for planning 90Y therapy of liver cancer. Technol Cancer Res Treat 2010; 9:253-262

75. Nijsen F, Rook D, Brandt C, Meijer R, Dullens H, Zonnenberg B, de Klerk J, van Rijk P, Hennink W, van het Schip F. Targeting of liver tumour in rats by selective delivery of holmium-166 loaded microspheres: A biodistribution study. Eur J Nucl Med 2001; 28:743-749

76. Kos S, Huegli R, Hofmann E, Quick HH, Kuehl H, Aker S, Kaiser GM, Borm PJ, Jacob AL, Bilecen D. Feasibility of real-time magnetic resonance-guided angioplasty and stenting of renal arteries in vitro and in swine, using a new polyetheretherketone-based magnetic resonance-compatible guidewire. Invest Radiol 2009; 44:234-241

77. Bulte JWM, Duncan ID, Frank JA. In vivo magnetic resonance tracking of magnetically labeled cells after transplantation. J Cereb Blood Flow Met 2002; 22:899-907

78. Carr HY, Purcell EM. Effects of diffusion on free precession in nuclear magnetic resonance experiments. Phys Rev 1954; 94:630-638

79. Meiboom S, Gill D. Modified spin-echo method for measuring nuclear relaxation times. Rev Sci Instr 1958; 29:688-691

80. Rozenman Y, Zou X, Kantor HL. Signal loss induced by superparamagnetic iron oxide particle in NMR spin-echo images: The role of diffusion. Magn Reson Med 1990;14:31-39

81. Bulte JWM, Miller GF, Vymazal J, Brooks RA, Frank JA. Hepatic hemosiderosis in non-human primates: Quantification of liver iron using different field strengths. Magn Reson Med 1997; 37:530-536

82. van de Maat GH, Seevinck PR, Vincken KL, de Leeuw H, Bakker CJ. Multi-echo spin-echo (MESE) signal behavior of paramagnetic Holmium-166 loaded microspheres for radiotherapy: experiment and simulation. Proc Intl Soc Mag Reson Med 2009:4468

83. Hahn EL. Spin echoes. Phys Rev 1950; 80:580-594

84. Ma J, Wehrli FW. Method for image-based measurement of the reversible and irreversible contribution to the transverse-relaxation rate. J Magn Reson Ser B 1996; 111:61-69

85. Yablonskiy DA, Haacke EM. An MRI method for measuring T2 in the presence of static and RF magnetic field inhomogeneities. Magn Reson Med 1997; 37:872-876

86. Haacke EM, Brown RW, Thompson MR, Venkatesan R (1999) Magnetic resonance imaging: Physical principles and sequence design. John Wiley & Sons, Inc. New York

87. Yablonski DA, Haacke EM. Theory of NMR signal behavior in magnetically inhomogeneous tissues: the static dephasing regime. Magn Reson Med 1994; 32:749-763

88. Gillis P, Koenig SH. Transverse relaxation of solvent protons induced by magnetized spheres: application to ferritin, erythrocytes, and magnetite. Magn Reson Med 1987; 5:323-345

89. Boxerman JL, Hamberg LM, Rosen BR, Weisskoff RM. MR contrast due to intravascular magnetic susceptibility perturbations. Magn Reson Med 1995; 34:555-566

90. Kiselev VG, Posse S. Analytical theory of susceptibility induced NRM signal dephasing in a cerebrovascular network. Phys Rev Lett 1998; 81:5696-5699

91. Kiselev VG, Posse S. Analytical model of susceptibility-induced MR signal dephasing: effect of diffusion in a microvascular network. Magn Reson Med 1999; 41:499-509

92. Jensen JH, Chandra R. Strong field behavior of the NMR signal from magnetically heterogeneous tissues. Magn Reson Med 2000; 43:226-236

93. Jensen JH, Chandra R. NMR relaxation in tissues with weak magnetic inhomogeneities. Magn Reson Med 2000; 44:144-156

94. Remmele S, Ring J, Sénégas J, Heindel W, Mesters RM, Bremer C, Persigehl T. Concurrent MR blood volume and vessel size estimation in tumors by robust and simultaneous ΔR2 and ΔR2* quantification. Magn Reson Med 2011; 66:144-153

95. de Leeuw H, Bakker CJG. Correction of gradient echo images for first and second

order macroscopic signal dephasing using phase derivative mapping. Neuroimage 2012; 60:818-829

96. van de Maat GH, Seevinck PR, Elschot M, Smits ML, de Leeuw H, van het Schip AD, Vente MA, Zonnenberg BA, de Jongh HW, Lam MG, Viergever MA, van den Bosch MA, Nijsen JF, Bakker CJ. MRI-based biodistribution assessment of holmium-166 ploy(L-lactic acid) microspheres after radioembolisation. Eur radiol 2013;23:827-835

97. Taouli B, Koh DM. Diffusion-weighted MR imaging of the liver. Radiol 2010; 254:47-66

98. Sack I, Gedat E, Bernarding J, Buntkowsky G, Braun J. Magnetic resonance elastography and diffusion-weighted imaging of the sol/gel phase transition in agarose. J Magn Reson 2004; 166:252-261

99. Rhodes BL, Legvold S, Spedding FH. Magnetic properties of holmium and thulium metals. Phys Rev 1958; 109:1547-1550

100. Eisenhauer EA, Therasse P, Bogaerts J, Schwartz LH, Sargent D, Ford R, Dancey J, Arbuck S, Gwyther S, Mooney M, Rubinstein L, Shankar L, Dodd L, Kaplan R, Lacombe D, Verweij J. New response evaluation criteria in solid tumours: revised RECIST guideline (version 1.1). Eur J Cancer 2009; 45:228–247

101. Salem R, Lewandowski RJ, Atassi B, Gordon SC, Gates VL, Barakat O, Sergie Z, Wong CY, Thurston KG. Treatment of unresectable hepatocellular carcinoma with use of 90Y microspheres (TheraSphere): safety, tumor response, and survival. J Vasc Interv Radiol 2005; 16:1627–1639

102. Deng J, Miller FH, Rhee TK, Sato KT, Mulcahy MF, Kulik LM, Salem R, Omary RA, Larson AC. Diffusion-weighted MR Imaging for determination of hepatocellular carcinanoma response to Yttrium-90 radioembolization. J Vasc Interv Radiol 2006; 17:1195–1200

103. Kamel IR, Reyes DK, Liapi E, Bluemke DA, Geschwind JFH. Functional MR imaging assessment of tumor response after 90Y microsphere treatment in patients with unresectable hepatocellular carcinoma. J Vasc Interv Radiol 2007; 18:49–56

104. Rhee TK, Naik NK, Deng J, Atassi B, Mulcahy MF, Kulik LM, Ryu Rk, Miller FH, Larson AC, Salem R, Omary RA. Tumor response after yttrium-90 radioembolization for hepatocellular carcinoma: comparison of diffusion-weighted functional MR imaging with anatomic MR imaging. J Vasc Interv Radiol 2008; 19:1180–1186

105. Stejskal EO, Tanner JE. Spin diffusion measurements: spin echoes in the presence

of a time-dependent field gradient. J Chem Phys 1965; 42:288–292

106. Zhong J, Kennan RP, Gore JC. Effects of susceptibility variations on NMR measurements of diffusion. J Magn Reson 1991; 95:267–280

107. Does MD, Zhong J, Gore JC. In vivo measurement of ADC change due to intravascular susceptibility variation. Magn Reson Med 1999; 41:236–240

108. Kennan RP, Zhong J,Gore JC. Effects of magnetic susceptibility variations on the apparent diffusion measured by NMR. In: LeBihan D, Rosen B. MR imaging of perfusion and diffusion. New York: Raven Press, 1995:110-121

109. Coldwell D, Sangro B, Wasan H, Salem R, Kennedy A. General selection criteria of patients for radioembolization of liver tumors: an international working group report. Am J Clin Oncol 2011; 34:337–341

110. Le Bihan D, Breton E, Lallemand D, Aubin ML, Vignaud J, Laval-Jeantet M. Separation of diffusion and perfusion in intravoxel incoherent motion MR imaging. Radiol 1988; 18:497–505

111. Majumdar S, Gore JC. Studies of diffusion in random fields produced by variations in susceptibility. J Magn Reson 1988; 78:41–55

112. Hardy PA, Henkelman RM. Transverse relaxation rate enhancement caused by particulates. Magn Reson Imaging 1989; 7:265–275

113. Karlicek RF, Lowe IJ. A modified pulsed gradient technique for measuring diffusion in the presence of large background gradients. J Magn Reson 1980; 37:75–91

114. Cotts RM, Hoch MJR, Sun T, Markert JT. Pulsed field gradient stimulated echo methods for improved NMR diffusion measurements in heterogeneous systems. J Magn Reson 1989; 83:252–266

115. Hardy PA, Henkelman RM. On the transverse relaxation rate enhancement induced by diffusion of spins through inhomogeneous fields. Magn Reson Med 1991; 17:348–356

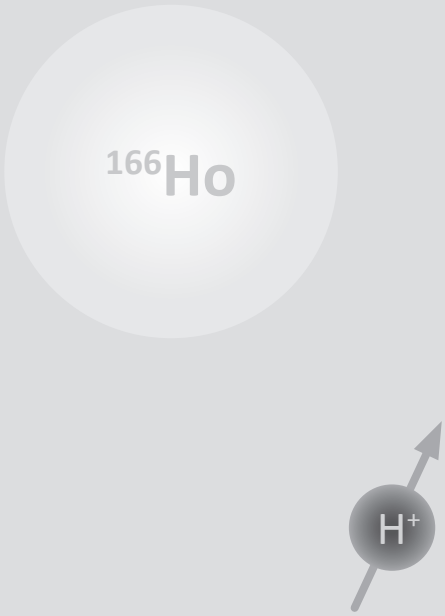
166Ho
H+

Samenvatting

"Er werd aangetoond dat met gebruik van MRI de *in vivo* verdeling van de microsferen en dus de verdeling van de stralingsdosis in kaart kan worden gebracht. Voorts werden nieuwe methoden gepresenteerd voor het verbeteren van deze biodistributiemetingen en werd de invloed van de aanwezigheid van de microsferen op diffusie-gewogen MRI, een MRI techniek voor de beoordeling van tumor respons, onderzocht."

Intra-arteriële radioembolisatie is een minimaal-invasieve therapie voor de behandeling van primaire levertumoren of levermetastasen, die kan worden toegepast als chirurgische resectie van de betreffende tumoren niet mogelijk is. Bij radioembolisatie worden microscopisch kleine, radioactieve bolletjes, zogenaamde microsferen, toegediend aan de lever via een katheter die is gepositioneerd in de leverslagader. De microsferen worden vervolgens meegevoerd met de bloedstroom en lopen uiteindelijk vast in het vaatbed van de lever. Doordat tumoren over het algemeen hun bloedtoevoer vooral aan de leverslagader onttrekken, terwijl gezond leverweefsel vooral wordt gevoed vanuit de poortader, is de verwachting dat de meeste microsferen zullen vastlopen in en rond de tumoren, met als gevolg dat vooral tumorweefsel wordt bestraald en gezond leverweefsel wordt gespaard. Deze biodistributie is in grote mate bepalend voor de effectiviteit en veiligheid van radioembolisatie. Daarom is het van essentieel belang om na toediening te kunnen meten waar de microsferen zijn terechtgekomen en hun stralingsdosis hebben afgegeven. Voor de microsferen die thans in de kliniek worden gebruikt, namelijk microsferen beladen met yttrium-90 (^{90}Y), is het meten van deze biodistributie echter een groot probleem. Alhoewel door middel van *single photon emission computed tomography* (SPECT), gebruikmakend van de vrijkomende *brehmsstrahlung*, en door middel van *positron emission tomography* (PET), een globale indruk verkregen kan worden van de verdeling van de microsferen in de lever, zijn de gevoeligheid en het oplossend vermogen van deze twee afbeeldingstechnieken niet voldoende om te bepalen wat de exacte stralingsdosis op de tumoren is geweest. Met name vanwege dit gebrek aan de mogelijkheid van biodistributiemetingen, is binnen het Universitair Medisch Centrum Utrecht in de afgelopen jaren een nieuw type microsfeer ontwikkeld: met holmium-166 beladen poly (L-lactic acid) microsferen, verder afgekort als Ho-MS. Dit type microsfeer heeft als grote voordeel dat het eigenschappen bezit die het mogelijk maken om met verscheidene medische beeldvormde technieken de verdeling van de microsferen in de lever in kaart te brengen. Ho-MS zenden namelijk gedurende het radioactieve verval, naast β-deeltjes benodigd voor de radiotherapie, ook γ-fotonen uit welke gebruikt kunnen worden om kwantitatieve SPECT-beelden te maken met een hogere resolutie dan mogelijk is met *brehmsstrahlung* SPECT. Daarnaast zijn Ho-MS sterk paramagnetisch en bieden daardoor de mogelijkheid voor detectie gebruikmakend van *magnetic resonance imaging* (MRI). Aangezien MRI een niet-invasieve beeldvormende techniek is, die veel mogelijkheden biedt wat betreft het weergeven van anatomische structuren en op het gebied van functie-onderzoek van lichaamsorganen, vormen Ho-MS als therapeutisch deeltje en MRI als afbeeldingsmodaliteit een interessante combinatie. In dit proefschrift werd het gebruik van MRI rondom holmium-radioembolisatie onderzocht. Er werd aangetoond dat met gebruik van MRI de *in vivo* verdeling van de microsferen en dus de verdeling van de stralingsdosis in kaart kan worden gebracht. Voorts werden nieuwe methoden gepresenteerd voor het verbe-

teren van deze biodistributiemetingen en werd de invloed van de aanwezigheid van de microsferen op diffusie-gewogen MRI, een MRI techniek voor de beoordeling van tumorrespons, onderzocht. Een samenvatting van dit werk is hieronder gegeven per hoofdstuk.

Hoofdstuk 2. De eerste resultaten werden beschreven van Ho-MS biodistributiemetingen in patiënten. Vijftien patiënten werden behandeld met radioactieve Ho-MS in het kader van een fase I klinische studie. De patiënten waren verdeeld in vier cohorten. Voor elk cohort werd de totale hoeveelheid toegediende microsferen gelijk gehouden (gemiddeld 484 mg), maar liep de beoogde gemiddelde dosis op de lever op van 20 Gy naar 80 Gy in stappen van 20 Gy. MRI scans werden gemaakt voor en na radioembolisatie op een 1.5T MRI-systeem. In de toegepaste scantechniek werd de *free induction decay* door middel van gradiëntecho's bemonsterd, waaruit de relaxatiesnelheid R_2^* kon worden bepaald. Een parametrisch R_2^* beeld voor de hele lever werd verkregen door voor elk beeldelement de waargenomen curve te fitten aan een mono-exponentieel model. Op deze beelden was goed zichtbaar waar de Ho-MS terecht waren gekomen. Om de lokale hoeveelheid microsferen te kwantificeren werd de door de Ho-MS geïnduceerde verandering in R_2^* berekend. Dit werd gedaan door van elke individuele R_2^* waarde na de behandeling de gemiddelde R_2^* waarde van de hele lever zoals gemeten voor de behandeling af te trekken. Om per volume-element de hoeveelheid microsferen te bepalen, werd gebruik gemaakt van de r_2^* relaxiviteit van Ho-MS (relaxatiesnelheid per eenheid van concentratie) zoals tevoren bepaald aan de hand van een kalibratiefantoom. De totale hoeveelheid die werd gemeten in de lever, gemiddeld 431 mg (spreiding 236 – 666 mg), was vergelijkbaar met de daadwerkelijk toegediende hoeveelheid (89 ± 19 % gemiddeld, correlatiecoëfficiënt $r = 0.7$; $P < 0.01$). De hoeveelheden per volume-element werden vervolgens omgerekend naar eenheden van activiteit door een vermenigvuldiging met de specifieke activiteit van de microsferen. De resultaten van MRI werden vergeleken met SPECT. Kwantitatieve Ho-MS activiteitsbeelden zoals gereconstrueerd uit SPECT opnamen, vertoonden een goede visuele overeenkomst met de op MRI gebaseerde activiteitsbeelden. Voor zowel MRI als SPECT werd de geabsorbeerde dosis berekend door middel van een convolutie van de activiteitsbeelden met een ^{166}Ho 3D *dose-point-kernel*, berekend met gebruikmaking van Monte Carlo code. Aan de hand van deze dosisberekeningen werd de gemiddelde geabsorbeerde dosis op de hele lever bepaald. Een goede correlatie werd gevonden tussen de gemiddelde leverdosis bepaald met MRI en SPECT (correlatiecoëfficiënt $r = 0.93$; $P < 0.001$).

Hoofdstuk 3. De conventionele R_2^* kwantificatiemethode, zoals gebruikt in hoofdstuk 2, kan falen wanneer het MRI signaal te snel vervalt als gevolg van een hoge lokale concentratie Ho-MS. Daarom werd er een *post-processing* methode, S_0-fitten, ontwikkeld om in

die gevallen toch de lokale R_2^* waarde te schatten. S_0-fitten maakt gebruik van de geschatte beginamplitude van de *free induction decay* (FID), S_0, van naburige voxels waarvoor wel voldoende signaal aanwezig was om R_2^* te bepalen. De gemiddelde S_0-waarde van deze naburige voxels wordt gebruikt als S_0-waarde voor het voxel waarin R_2^* niet bepaald kon worden. Door middel van dit extra gegenereerde meetpunt wordt vervolgens alsnog een R_2^* waarde bepaald. De methode werd toegepast op een conventionele multigradient-echo (MGE) dataset van een buisjesfantoom met bekende concentraties Ho-MS (variërend van 0 – 15 mg/ml) en op een dataset van een *ex vivo* konijnenlever waaraan Ho-MS waren toegediend. Door het toepassen van S_0-fitten konden R_2^* waardes tot een maximum van 2300 s^{-1} worden bepaald, wat overeenkomt met een maximum Ho-MS-concentratie van 11.5 mg/ml op een magnetische veldsterkte van 3T. Dit in vergelijking met een maximumwaarde van 1000 s^{-1} (overeenkomend met een Ho-MS concentratie van 5 mg/ml op 3T) die kon worden bepaald door middel van de conventionele kwantificatiemethode. De S_0-fitten methode werd gevalideerd door resulterende R_2^* waardes en bijbehorende r_2^* relaxiviteitwaardes te vergelijken met waardes die werden bepaald door gebruik te maken van *quantitative ultrashort TE imaging* (qUTE), een speciale MRI methode voor het bemonsteren van snel vervallende signalen. Met gebruikmaking van S_0-fitten, toegepast op de conventionele MGE dataset, werd een Ho-MS relaxiviteit gevonden van 206 ± 12 $s^{-1}.mg^{-1}.ml$, terwijl met de qUTE methode een relaxiviteit van 205 ± 16 $s^{-1}.mg^{-1}.ml$ werd gevonden. Metingen aan de *ex vivo* konijnenlever, waarin de totale hoeveelheid Ho-MS werd berekend aan de hand van R_2^*-metingen, leverden voor respectievelijk de conventionele methode, de S_0-fitten methode en de qUTE methode hoeveelheden op van 7.21 mg, 8.20 mg en 8.26 mg. Dit laat zien dat S_0-fitten de accuraatheid verhoogt van de Ho-MS-kwantificatie in het geval van hoge lokale concentraties microsferen, ervan uitgaande dat qUTE als de gouden standaard mag worden beschouwd.

Hoofdstuk 4. Onderzocht werd of door middel van MRI accurate driedimensionale ^{166}Ho activiteitsdistributie-metingen kunnen worden gedaan, om aan de hand daarvan de geabsorbeerde stralingsdosis te kunnen bepalen in de lever na radioembolisatie. Voor dit doeleinde werden MRI, *computed tomography* (CT) en SPECT experimenten uitgevoerd op een fantoom met tumor-simulerende stukjes gel waarin zich radioactieve Ho-MS bevonden, en op een *ex vivo* humane lever met tumoren waaraan radioactieve Ho-MS waren toegediend. Driedimensionale stralingsdosisverdelingen werden bepaald door convolutie van de ^{166}Ho activiteitsdistributie, bepaald aan de hand van MRI beelden, met een ^{166}Ho *dose-point-kernel*. Deze kernel was gegenereerd met *Monte Carlo N-Particle transport code*, gebruikmakend van standaarden gedefinieerd in *Medical Internal Radiation Dose Pamphlet 17*. Op MRI gebaseerde stralingsdosisverdelingen werden kwalitatief vergeleken met CT en autoradiografie en kwantitatief vergeleken met op SPECT gebaseerde dosisverdelingen. Zowel de op MRI als op SPECT gebaseerde metingen werden gevalideerd

aan de hand van metingen met een dosiscalibrator. De goede lineaire relatie die werd gevonden tussen MRI-waardes en dosiscalibrator-waardes zoals gemeten voor het fantoom (richtingscoëfficiënt 1.05; R^2 = 0.99), liet zien dat door middel van MRI de lokale activiteit accuraat kan worden bepaald. De op MRI gebaseerde stralingsdosisverdelingen in de *ex vivo* humane lever vertoonden grote visuele overeenkomst met op SPECT gebaseerde verdelingen. Een kwantitatieve vergelijking tussen MRI, SPECT en dosiscalibrator metingen liet zien dat zowel lokaal als voor de hele lever de afwijkingen in hoeveelheid niet groter waren dan 10%. Een zeer goede overeenkomst werd tevens gevonden tussen op MRI en SPECT gebaseerde dosis-volume-histogrammen.

Hoofdstuk 5. Een nieuwe methode werd geïntroduceerd, *S_0 estimation of the free induction decay combined with a single spin echo measurement* (SOFIDSE), waarmee simultaan R_2^* en R_2 gemeten kunnen worden in een korte scantijd. SOFIDSE bepaalt R_2^* en de signaalamplitude op tijdstip 0, S_0, aan de hand van een multi-gradientecho (MGE) bemonstering van de *free induction decay*, waarna vervolgens R_2 wordt bepaald door middel van S_0 en een enkele spin-echometing. Door de aldus bepaalde R_2 waarde af te trekken van de R_2^* waarde, wordt de parameter R_2' berekend. Deze R_2' waarde is een directe maat voor het door de Ho-MS geïnduceerde signaalverlies, en is niet meer afhankelijk van de R_2 waarde van het leverweefsel waarin de microsferen zich bevinden. Door deze onafhankelijkheid van R_2 is SOFIDSE niet gevoelig voor veranderingen in de R_2 van weefsels zoals die kunnen optreden als gevolg van de therapie. Daarmee neemt SOFIDSE in principe de noodzaak weg om ook voor aanvang van de therapie een MRI scan te maken. De methode SOFIDSE werd gevalideerd door R_2 waardes bepaald met SOFIDSE te vergelijken met waardes die waren bepaald met gebruikmaking van een zogenaamde *shifted spin echo* (SSE) techniek. Deze validatie werd gedaan aan de hand van metingen aan een buisjesfantoom met bekende hoeveelheden Ho-MS en middels metingen in een gezonde vrijwilliger. Gemiddeld genomen gaf SOFIDSE een overschatting van R_2 (5%) vergeleken met SSE, welke overschatting niet afhankelijk bleek van de concentratie Ho-MS. R_2' waardes die werden bepaald door het verschil tussen R_2^* en respectievelijk SOFIDSE R_2 en SSE R_2, lieten een goede correlatie zien (correlatiecoëfficiënt r = 1, $P = 9 \cdot 10^{-11}$). Voorts werd aangetoond dat de door de holmiummicrosferen geïnduceerde R_2' waardes, in tegenstelling tot de bepaalde R_2^* waardes, niet gevoelig zijn voor de R_2 waarde van het medium waarin ze zich bevinden. Dit werd gedaan met behulp van buisjes met een variatie aan R_2 waardes en een gelijke concentratie Ho-MS.

Hoofdstuk 6. De diffusieafhankelijkheid van de spin-echo relaxiviteitsparameter r_2, en daarmee van de SOFIDSE relaxiviteitsparameter $r'_{2\,SOFIDSE}$ zoals die geïntroduceerd werd in hoofdstuk 5, werd onderzocht. SOFIDSE experimenten werden uitgevoerd op een buisjesfantoom met een reeks bekende Ho-MS concentraties waarvan de diffusiecoëfficiënt werd gevarieerd door de temperatuur te veranderen. Daarnaast werden diffusie-gewo-

gen MRI beelden (DWI) gemaakt om de mate van diffusie te meten aan de hand van de zogenaamde *apparent diffusion coefficient* (ADC). Ho-MS r_2 en r_2^* relaxiviteitswaardes werden berekend via een lineaire fit aan ΔR_2 en ΔR_2^* als functie van de concentratie, zoals gemeten met SOFIDSE voor het hele bereik van gemeten ADC waardes. Een verhoging van 6.7 $s^{-1}.mg^{-1}.ml$ naar 9.3 $s^{-1}.mg^{-1}.ml$ werd gevonden voor r_2 voor een ADC bereik van 1.24 x 10^{-3} mm^2/s tot 3.86 x 10^{-3} mm^2/s. Veranderingen in r_2^* die werden gevonden werden toegeschreven aan de temperatuurafhankelijkheid van de susceptibiliteit van holmium en werden als zodanig meegenomen in de berekeningen. Voor een geschat temperatuurbereik van 1.1°C tot 46.3°C werd gevonden dat r_2^* afnam van 108.3 $s^{-1}.mg^{-1}.ml$ naar 98.3 $s^{-1}.mg^{-1}.ml$. Een vergelijking van deze gevonden waardes met die van numerieke simulaties, gebaseerd op een analytisch model voor NMR signaalgedrag in heterogene systemen onderhevig aan diffusie, liet een goede overeenkomst zien tussen experiment en theorie. Met de lichaamstemperatuur als referentie, werd gevonden dat de afwijking van de relaxiviteitsparameter $r'_{2\ SOFIDSE}$, berekend door middel van substractie van r_2^* en r_2, niet groter was dan 2.8% over het gehele bereik van onderzochte ADC waardes.

Hoofdstuk 7. De invloed van de aanwezigheid van Ho-MS op diffusie-gewogen MRI (DWI), en daarmee op de bepaling van de apparent diffusion coefficient (ADC) na radioembolisatie, werd onderzocht. DWI werd uitgevoerd op een fantoom met buisjes met daarin bekende concentraties Ho-MS. Signaalintensiteitsmetingen op de DWI beelden ,voor elke concentratie Ho-MS en elke toegepaste b-waarde, lieten een signaalreductie zien die afhankelijk was van zowel de concentratie microsferen als de b-waarde. ADC-waardes, bepaald door middel van een mono-exponentiële fit aan de DWI signaalintensiteiten, lieten een afname zien van -0.16 x 10^{-3} mm^2/s per mg/ml Ho-MS voor een basis ADC waarde van 2.09 x 10^{-3} mm^2/s. Diffusie-gewogen beelden werden ook gemaakt van een patiënt die holmium radioembolisatie had ondergaan voor de behandeling van levermetastasen. ADC waardes werden berekend aan de hand van DWI beelden die waren gemaakt zowel voor als na toediening van de microsferen. De resulterende ADC beelden werden vergeleken met kwantitatieve, op R_2^* gebaseerde biodistributie-metingen. Signaalafname werd geobserveerd op posttherapie DWI beelden in leverregio's met hoge concentraties Ho-MS. De lage signaal-ruis-verhouding in deze regio's resulteerde in een niet-accurate ADC bepaling of maakte de bepaling onmogelijk door een te gering aantal bruikbare meetpunten.

Het werk beschreven in dit proefschrift en hierboven samengevat laat duidelijk de belangrijke rol zien die MRI kan spelen rondom ^{166}Ho radioembolisatie. Op R_2^* gebaseerde MRI levert een kwantitatieve, gedetailleerde afbeelding op van de verdeling van de toegediende microsferen in de lever, waardoor op tumorniveau de geabsorbeerde stralingsdosis bepaald kan worden. Met gebruikmaking van deze dosismetingen kan zowel

de veiligheid als de effectiviteit van de radioembolisatieprocedure geëvalueerd worden, omdat beoordeeld kan worden of het stralingstolerantieniveau voor gezond leverweefsel niet is overschreden, en of tumoren een dosis hebben ontvangen die naar verwachting afdoende is voor behandeling van tumorweefsel. Deze informatie kan vervolgens worden gebruikt om te bepalen of de behandelingsdoeleinden zijn bereikt of dat een vervolgbehandeling noodzakelijk is en als veilig mag worden beschouwd. Een sterke eigenschap van op MRI gebaseerde dosismetingen is dat de scantijden relatief kort zijn, vergeleken met het alternatief SPECT, wat mogelijkheden geeft om de microsfeerdistributie te monitoren tijdens de toedieningsprocedure. Het *realtime* monitoren van de microsferen in de gehele lever gedurende injectie mag dan momenteel nog niet realistisch zijn, gezien de benodigde scantijden genoemd in dit proefschrift, een scenario waarin de totale toe te dienen dosis wordt opgedeeld in kleinere injecties, met na elke deeltoediening een biodistributiemeting, ligt wel binnen handbereik. Aan de hand van deze tussentijdse metingen kan dan beoordeeld worden of de toediening kan worden voortgezet, afhankelijk van of de veiligheidsmarges zijn bereikt en of tumoren adequaat behandeld zijn. In plaats van de volledige lever te behandelen, biedt het gebruik van MRI tijdens de toedieningsprocedure ook mogelijkheden voor het selectief toedienen van de microsferen aan meer afgebakende delen van de lever of individuele tumoren, omdat voor MRI de benodigde scantijd schaalt met de grootte van het af te beelden gebied. Een dergelijke selectieve benadering zou mogelijk veel veiliger en effectiever kunnen zijn, vooral voor patiënten met een beperkt aantal te behandelen tumoren, omdat gezond leverweefsel in mindere mate een stralingsdosis ontvangt terwijl de dosis op de tumor mogelijk juist vergroot wordt.
Op het gebied van MRI-gebaseerde tumorresponsmetingen introduceert het gebruik van ^{166}Ho microsferen enkele uitdagingen. Vooral bij het gebruik van diffusie-gewogen MRI, voor het bepalen van de aan weefseleigenschappen gerelateerde *apparent diffusion coefficient*, doen zich twee problemen voor. Ten eerste wordt het karakteriseren van de lokale ADC bemoeilijkt doordat de aanwezigheid van microsferen zorgt voor signaalvermindering op diffusie-gewogen beelden en een daarmee samenhangende lagere signaal-ruis-verhouding. Ten tweede wordt de ADC afhankelijk van de lokale concentratie holmiummicrosferen. Voor dit laatste effect kan wellicht gecorrigeerd worden op basis van biodistributiemetingen en de bekende relatie tussen concentratie microsferen en ADC. Het tenietdoen van de door holmium veroorzaakte signaalvermindering zal echter waarschijnlijk minder gemakkelijk zijn, omdat voor MRI over het algemeen geldt dat een verhoging van de signaal-ruisverhouding gepaard gaat met een langere scanduur. Gebruikmaken van hogere magnetische veldsterktes zoals 3T of 7T, zal wel de aanvankelijk beschikbare signaalsterkte vergroten maar het gebruik van deze hogere veldsterktes zal ook leiden tot sterker signaalverval als gevolg van de microsferen. Deze factoren zullen moeten worden meegenomen in de zoektocht naar een goede oplossing. Met de

door Ho-MS veroorzaakte signaalvermindering moet ook rekening gehouden worden als de therapierespons wordt beoordeeld aan de hand van conventionele T_1 of T_2-gewogen beelden. Alhoewel het niet de verwachting is dat anatomische structuren vervormd zullen worden weergegeven, zal wel het contrast tussen weefselstructuren verschillend zijn voor beelden die zijn gemaakt voor toediening en na toediening van de microsferen. Radiologen moeten daarom bedacht zijn op dergelijke effecten om foutieve interpretatie van de beelden te voorkomen.

Concluderend kunnen we stellen dat de combinatie van magnetische resonantie beeldvorming en ^{166}Ho radioembolisatie duidelijk potentie heeft om de veiligheid en effectiviteit van radioembolisatie te vergroten en dat deze combinatie de weg opent naar beeldgeleide therapie.

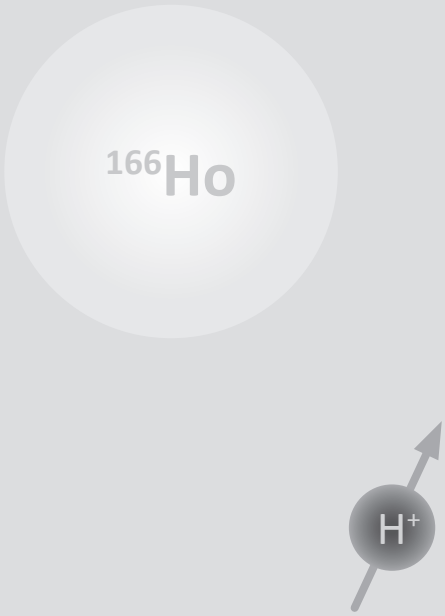
166Ho
H+

Dankwoord

“Een ieder die op welke manier dan ook een steentje heeft bijgedragen kan zich verzekerd zijn van mijn dank daarvoor”

Ook al staat er maar één naam op de voorkant van dit proefschrift, het werk dat erin beschreven staat had niet uitgevoerd kunnen worden zonder hulp van anderen. Eerst en bovenal niet zonder de hulp van God, die ik dank voor de talenten die Hij mij gegeven heeft om dit onderzoek uit te kunnen voeren. Daarnaast niet zonder de hulp van alle mensen die bij dit onderzoek betrokken zijn geweest, zij het direct of zijdelings. En nu kan ik hier een bijna oneindige lijst van namen van mensen die ik wil bedanken neer gaan zetten, maar het gevaar bestaat dat ik dan iemand vergeet of tekort doe. Een ieder die op welke manier dan ook een steentje heeft bijgedragen kan zich verzekerd zijn van mijn dank daarvoor. Enkele personen wil ik echter bij naam noemen:

Chris Bakker, mijn begeleider en co-promotor. Beste Chris, hierbij een kort woord van dank in plaats van een lofrede ook al zou dat op zijn plaats zijn. Dank voor al de tijd die je in me hebt geïnvesteerd voor onder meer het wegwijs maken binnen het wereldje dat wetenschap heet, het zoeken naar 'de waarheid' op gebied van MRI en diffusie, en het plaatsen van kanttekeningen bij door mij geschreven proza (lees: artikelen). Je nuchtere kijk op onderzoek doen, heeft me de moed gegeven om uiteindelijk toch ook maar een boekje te gaan schrijven.

Mijn promotoren, Max Viergever en Maurice van den Bosch. Beste Max, bedankt dat ik een aantal van mijn levensjaren heb mogen doorbrengen bij het Image Sciences Institute om daar dit onderzoek uit te voeren. Ik heb er al die tijd met plezier mogen werken. Ook dank voor het grondige commentaar op dit proefschrift. Beste Maurice, je interesse vanuit de radiologie voor het holmiumonderzoek heeft er mede voor gezorgd dat in dit proefschrift MRI-beelden staan van de eerste patiënten behandeld met holmium radioembolisatie. Bedankt dat ik nog een tijdje mocht blijven om de nog lopende zaken af te kunnen ronden.

Mijn mede "holmium-MRI-plaatjesmakers" en tevens paranimfen, Peter Seevinck en Hendrik de Leeuw. Peter, bedankt voor je hulp bij het bedwingen van de scanner, de vele, soms heftige, maar meestal verhelderende discussies over relaxometrie en diffusie, en de prettige samenwerking voor een groot deel van de hoofdstukken van dit proefschrift. Hendrik, bedankt dat je al die jaren je kamer met me wilde delen, zowel in het UMC als in verre oorden, dat ik je mocht vervelen met de meest onbenullige vragen, al dan niet op het gebied van MRI, en de telefoon voor je mocht aannemen. De verse koffie die 's ochtends vaak klaar stond, alhoewel je zelf geen druppel dronk, heb ik erg kunnen waarderen. Ook Jan-Henry Seppenwoolde wil ik hier nog noemen. Beste Jan-Henry, ook al was onze samenwerking erg kort, omdat je al snel nadat ik met mijn onderzoek bij het ISI begon naar het zendingsveld werd geroepen, bedankt voor de allereerste MRI-kennis die je me hebt bijgebracht.

De onderzoekers betrokken bij het holmiumproject, ieder vanuit zijn of haar eigen expertise. Frank Nijsen, in mijn beleving staat het woord holmium zo ongeveer op jouw voorhoofd geschreven. De gedrevenheid waarmee je holmiumtherapie vanuit het laboratorium naar de kliniek probeert te krijgen heeft er mede voor gezorgd dat mijn enthousiasme voor het afbeelden van de bolletjes met behulp van MRI alleen maar is gegroeid. Bernard Zonnenberg, zonder patiënten geen behandeling. Ondanks dat een eerste klinische studie voor een nieuwe therapie op sommige momenten haast een onneembare horde lijkt, staan in dit proefschrift toch resultaten vermeld van alle patienten behandeld in het kader van de fase I studie. Bedankt dat ik er bij mocht zijn om de eerste holmiumverdelingen in patienten te meten met behulp van MRI. Fred van het Schip, bedankt voor alle hulp rondom zaken als radioactiviteit en dosisbepaling. Maarten Vente, voor dierenexperimenten kon ik altijd bij jou terecht. Dank voor alle hulp bij het prepareren van levers en andere zaken waar bloed bij kwam kijken. Remmert de Roos, een fysicus los laten lopen in een radionuclidenlab is een niet te onderschatten risicofactor. Bedankt voor alle hulp bij het bereiden van fantomen, ex-vivo materialen en alle andere zaken die nodig waren om mijn MRI experimenten (goed) te laten verlopen. Wouter Bult, ons uitstapje naar fluor imaging heeft dan misschien geen baanbrekende resultaten opgeleverd, ik heb er in elk geval weer wat bijgeleerd op het gebied van moleculaire bindingen. Dank daar voor. Mattijs Elschot, ook al lijkt het dat ik in dit proefschrift SPECT wegzet als een inferieure afbeeldingstechniek, het feit dat, in zowel hoofdstuk 2 als 4, SPECT als referentiestandaard wordt gebruikt zegt denk ik al genoeg. Bedankt voor alle hulp rondom SPECT, dosekernels en dosisverdelingen. En natuurlijk bedankt voor de data t.b.v. het plotje. Maarten Smits, bedankt voor alle hulp rondom patiëntendata gerelateerde zaken. Marnix Lam, bedankt voor de prettige samenwerking vooral ook met betrekking tot hoofdstuk 2 van dit schrijven. Tjitske Bosma, bedankt voor het steeds tijdig melden dat ik de scanner maar weer eens moest aanzwengelen omdat er weer een patiënt onderweg was, en alle andere zaken die daar mee te maken hadden.
MRI-laboranten, zonder jullie geen MRI-beelden van patiënten. Dank voor jullie inzet om zo mooi mogelijke “foto’s” te maken en dat ik op de meest ongelukkige momenten binnen mocht vallen om “nog wat data te rec-parren”. Niels Blanken, dank voor alle hulp bij het implementeren van de benodigde scanprotocollen en alle andere zaken die nodig waren om de holmiumstudie succesvol te laten verlopen.
Chris Oerlemans, bollenmaker. Wat we in elk geval samen hebben geleerd is dat magnetische roerstaafjes het terugvinden van alginaatbollen op MRI-beelden bemoeilijkt. Bedankt voor die ervaring en het veelvuldig gezelschap houden in het lab.
Koen Vinken, ook al staat een experimenteel natuurkundige soms wat wantrouwig tegenover simulaties, je software heeft me verschillende keren weer teruggebracht op het rechte pad wanneer mijn experimenten vreemde afwijkingen vertoonden. Dank daarvoor.

Alle overige collega's bij het ISI en de divisie Beeld wil ik bedanken voor het delen van kennis en inzichten, jullie advies en hulp bij allerlei (rand)zaken en voor de gezelligheid tijdens etentjes, conferenties en andere sociale aangelegenheden. Mensen van de OIO-steeg, bedankt voor alle zinnige en minder zinnige gesprekken tijdens de koffiepauze, lunchpauze of om andere redenen gerechtvaardigde werkonderbrekingen. Ook al was het alsof ik wat langer bleef hangen omdat ik mijn werk nog niet af had, eigenlijk kon ik jullie natuurlijk gewoon nog niet missen.

Het laatste stukje van dit dankwoord is gereserveerd voor degenen die me het meest dierbaar zijn. Lieve Berdien, bedankt voor het fijne thuisfront dat je me geeft en voor het vertrouwen dat het heus nog wel eens goed zou komen met dit boekje. Lieve Noah, mocht je later dit boekje nog eens lezen, zie het dan maar als een verhaal dat gaat over de tijd waarin jij papa 's ochtends uitzwaaide als hij met de bus naar het ziekenhuis ging. Lieve Zara, jij maakt alleen nog maar het allerlaatste gedeelte mee van de periode die dit boekje afsluit maar een mooiere afsluiting kan ik me eigenlijk niet indenken.

Gerrit

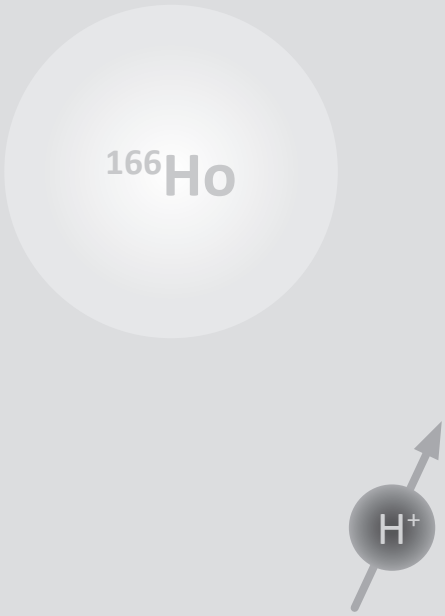
166Ho
H+

List of publications

Curriculum vitae

"In hetzelfde jaar startte hij een promotieonderzoek bij het Image Sciences Institute van het Universitair Medisch Centrum Utrecht, met als onderwerp "MRI-geleide inwendige radiotherapie van levertumoren met holmium-geladen microsferen."

Publications

International journals:

- van de Maat GH, Seevinck PR, Elschot M, et al. MRI-based biodistribution assessment of Holmium-166 poly(L-lactic acid) microspheres after radioembolisation. Eur Radiol 2013;23:827-835

- van de Maat GH, Seevinck PR, Bos C, et al. Quantification of holmium-166 loaded microspheres: estimating high local concentrations using a conventional multiple gradient echo sequence with S0-fitting. J Magn Res Imag 2012;35:1453-1461

- Bakker CJ, de Leeuw H, van de Maat GH, et al. On the utility of spectroscopic imaging as a tool for generating geometrically accurate MR images and parameter maps in the presence of field inhomogeneities and chemical shift effects. Magn Reson Imaging 2013; 31:86-95

- Oerlemans C, Seevinck PR, van de Maat GH, et al. Alginate-lanthanide microspheres for MRI-guided embolotherapy. Acta Biomater 2013;9:4681-4687

- Seevinck PR, van de Maat GH, de Wit TC, et al. Magnetic resonance imaging-based radiation-absorbed dose estimation of (166)ho microspheres in liver radioembolization. Int J Radiat Oncol Biol Phys 2012;83:e437-444

Conference proceedings (first author only):

- GH van de Maat, MAD Vente, JFW Nijsen, et al. The influence of holmium-166 loaded microspheres on diffusion weighted imaging: an ex-vivo study. Proc Intl Soc Mag Reson Med 2012:1851

- GH van de Maat, UA Blume, CJ den Harder, et al. Macroscopic meets microscopic: the use of Multi acquisition variable resonance image combination (MAVRIC) for detection of microscopic objects by means of off-resonance excitation. Proc Intl Soc Mag Reson Med 2011:4522

- GH van de Maat, M Elschot, PR Seevinck, et al. Detection and quantification of Holmium-166 loaded microspheres in patients with liver metastases: initial experience within the framework of a phase I study. Proc Intl Soc Mag Reson Med 2011:201

- GH van de Maat, PR Seevinck, CJ Bakker. The influence of Holmium-166 loaded microspheres on ADC measurements using DWI. Proc Intl Soc Mag Reson Med 2010

- GH van de Maat, H de Leeuw, PR Seevinck, et al. Selective positive contrast of subvoxel field-disturbers using off-resonance excitation. Proc Intl Soc Mag Reson Med 2010

- GH van de Maat, PR Seevinck, KL Vincken, et al. Multi-echo Spin-echo (MESE) signal behavior of paramagnetic Holmium-166 loaded microspheres for radiotherapy: experiment and simulation. Proc Intl Soc Mag Reson Med 2009:4468

- GH van de Maat, A van der Toorn, BA Zonnenberg, et al. Single-point 19F imaging of fluorinated drugs injected into the eye for the treatment of macular degeneration. Proc Intl Soc Mag Reson Med 2009:4357

Curriculum vitae

Gerrit van de Maat was born on April 16th 1982 in Almelo, the Netherlands. In 2000 he graduated from secondary school (VWO, Jacobus Fruytier scholengemeenschap, Apeldoorn) and started studying applied physics at the University of Twente. During his study he went to Heidelberg, Germany, for an internship at the European Molecular and Biology Laboratory (EMBL). After a research project at the biophysical engineering group of the University of Twente, he obtained his Masters' degree in 2007. In the same year he started as a PhD student at the Image Sciences Institute, University Medical Center, Utrecht, on the subject "Magnetic resonance imaging-guided internal radiation therapy of liver tumors with holmium-loaded microspheres." The results of this research project are described in this thesis.

Gerrit van de Maat werd geboren op 16 april 1982 te Almelo, Nederland. In 2000 behaalde hij het VWO diploma (Jacobus Fruytier Scholengemeenschap, Apeldoorn) en begon de studie Technische Natuurkunde aan de Universiteit Twente. Tijdens deze studie ging hij naar Heidelberg, Duitsland, voor een stage bij het European Molecular and Biology Laboratory (EMBL). Na zijn afstudeerproject bij de leerstoel biofysische technieken van de Universiteit Twente ontving hij in 2007 zijn doctoraaldiploma. In hetzelfde jaar startte hij een promotieonderzoek bij het Image Sciences Institute van het Universitair Medisch Centrum Utrecht, met als onderwerp "MRI-geleide inwendige radiotherapie van levertumoren met holmium-geladen microsferen." De resultaten van dit onderzoek zijn beschreven in dit proefschrift.